Investigating the Position-Sensitive Capabilities of Segmented Germanium Detectors using Gamma Imager

A thesis submitted in partial fulfillment of the requirements for

the degree of

DOCTOR OF PHILOSOPHY

by

ARZOO SHARMA

(2017PHZ0005)

DEPARTMENT OF PHYSICS

INDIAN INSTITUTE OF TECHNOLOGY ROPAR

June 2023

.... to my family and friends

Declaration of Originality

I, hereby, declare that the work being presented in the thesis entitled **"Investigating the Position-Sensitive Capabilities of Segmented Germanium Detectors using Gamma Imager"** has been solely authored by me. It presents the result of my independent investigation/research conducted during the period from **August 2017** to **June 2023** under the supervision of **Dr. Pushpendra P. Singh**. To the best of my knowledge, it is an original work, both in terms of research content and narrative, and has not been submitted or accepted elsewhere, in part or in full, for the award of any degree, diploma, fellowship, associateship, or similar title of any university or institution. Further, due credit has been attributed to the relevant state-of-the-art collaborations (if any) with appropriate citations and acknowledgements in line with established ethical norms and practices. I also declare that any idea/data/fact/source stated in my thesis has not been fabricated/ falsified/ misrepresented. All the principles of academic honesty and integrity have been followed. I fully understand that if the thesis is found to be unoriginal, fabricated, or plagiarized, the Institute reserves the right to withdraw the thesis from its archive and revoke the associated Degree conferred. The Institute also reserves the right to appraise all concerned sections of society of the matter for their information and necessary action (if any). If accepted, I hereby consent for my thesis to be available online in the Institute's Open Access repository, inter-library loan, and the title & abstract to be made available to outside organizations.

Arzoo Sharma
2017PHZ0005 / Ph.D.
Department of Physics
Indian Institute of Technology Ropar
Rupnagar, Punjab - 140 001, India

Date: June 19, 2023

Acknowledgement

With the grace of God, I am finally submitting my Ph.D. thesis. The journey has been like a wave, and God has always been kind for providing me the strength to continue putting in effort without stopping, *Jai Shree Ram*.

The most profound gratitude goes to Dr. Pushpendra P. Singh, my Ph.D. advisor, for investing in me and encouraging me throughout the journey. I distinctly recall the day he instilled faith in me despite my qualms about taking on such a challenging project. Sir, I appreciate the support you provided during this project. I would like to acknowledge Prof. R. Palit (TIFR, Mumbai) and Prof. J. Gerl (GSI, Germany) for their constant discussions on different experiments and analyses of the work and for allowing me to work with them. Your guidance, perseverance, and support made it possible to get through tough yet interesting situations. Special thanks to Prof. H.J. Wollersheim for constant feedback on the topic and help whenever needed and for acquainting me to the world of nuclear detectors and instrumentation during my early Ph.D. days. Recalling the day I arrived in Germany, an entirely new place, new people, new language, but seeing you at the airport was a relief.

I sincerely thank Dr. M. Gorska-Ott and Dr. H.M. Albers for allowing me to work with the DESPEC/HISPEC group at GSI. I would also like to thank the lab mentors, Dr. I. Kojouharov, Dr. P. Herrmann, and Dr. H. Schaffner, for their continuous help during the testing of the detectors and experiment. I acknowledge Dr. T. Habermann for all the assistance and discussions on critical analysis. Special thanks to Dr. A. Banerjee for helping and motivating me and the special khichdi. Your support is like a pillar. I also thank all the DESPEC group members, especially Dr. Biswarup Das, Biswajit Das, G. Aggez, S. Alhomaidhi, M. Mikolajczuk, R. Donthi, Dr. J. Vesic, Dr. E. Sahin, Dr. M. Polettini, Dr. N. Hubbard, Dr. A. Mistry, B. Bles, J. Bardak, A. Yaneva, M. Armstrong, Dr. Z. Chen, Dr. T. Arici, G. Kosir. I still miss my UNO team; playing with you has been a stress reliever. Preparing apple pie with Michal has been a show-stopper for me.

The Ministry of Education (MoE), Government of India, and the National Mission on Interdisciplinary Cyber-Physical Systems (NM - ICPS), Department of Science & Technology (DST), Government of India, through the Technology Innovation Hub - AWaDH at the Indian Institute of Technology Ropar, are gratefully acknowledged for the Ph. D. fellowship. I also acknowledge the support from the Department of Atomic Energy, Government of India, under project No. 12P-R&D-TFR-5.02-0400 and the Helmholtz International Center for FAIR/GET_INvolved in Germany. Further, I acknowledge Pascal Quirin, Michael Ginsz, and their complete team at MIRION Technologies for the comprehensive discussion and cooperation for the work.

I thank my Doctoral Committee members, Dr. Shubhrangshu Dasgupta (Chairperson), Prof. P. K. Raina, Dr. Asoka Biswas, and Prof. Manoranjan Mishra, for regularly monitoring the progress of my work and providing invaluable suggestions towards the improvement of the thesis. I thank the staff at the Department of Physics for their support, Mr. Sahil Kapoor, Mr. Satish, and

Ms. Athira for assisting me in utilizing all the facilities available in the department, and special thanks to Mr. Anshu Vaid for all the help and motivation during this journey.

I acknowledge my friends Dr. Kanika and Shaifali. On my first day at GSI, I suddenly met Kanika outside an office, a complete coincidence but an amazing one. I am thankful to God that I could meet both of you. You have helped me in all the situations in Germany and to adjust to an entirely different and new environment. The place would not have been the same without you. I also extend my gratitude to the Mohite family. Thank you for all the helpful future discussions and the food. I further acknowledge Dr. R.S. Siddhu for being so kind and helpful during my starting journey at GSI. I would like to thank one of my new friends, Danny, for being lovely and a good host during my visit to Heidelberg. I also acknowledge my new Steinhaus friends Jewel, Dr. Om, Dr. Rinku, Dr. Vishnu, Dr. Deepak, Divyang, and Suraj for making me feel at home and cooking special lunch and dinner. I thank the whole GSI staff for all the assistance during the stay.

I would like to acknowledge my NuStAR seniors Pawan bhaiya, Arshiya di, and Rudra bhaiya (pursuing promising postdocs abroad) for all the valuable suggestions and feedback during the course of this journey. I further acknowledge my new NuStAR team members for maintaining a friendly and healthy environment in the group. You guys are very enthusiastic, and I hope you stay the same throughout your Ph.D. journey and get a good degree. I thank my friend Riya for being an asset in my life. You have helped a lot in every situation. The day we met, my first day in the classroom, I never thought of becoming such good friends. Special thanks to Dr. Piyush for helping me whenever needed and for our after-dinner discussions on Science/Engineering/stocks/politics/fashion. I acknowledge Swati for essential Ph.D. discussions and short trips to Ropar town. I will never forget our first dahi kabab together. Special thanks to Sonam, who is also an inspiration to me. You have been a strong, kind, and accommodating person. I am happy to have you as my roommate. I also acknowledge my friends Amrit, Gonika, and Anisha for their support and motivation.

I acknowledge my PG lab members Paramjeet, Dr. Malika, Katyayni, and Rajat for keeping the small lab alive. The short discussions during the tea breaks have been fascinating. I wish you all a beautiful journey ahead! Special thanks to Katyayni and Paramjeet for caring about me related to all matters. I acknowledge everyone who played an essential role in keeping this journey going. The mess and canteen workers for serving delicious food on demand.

I especially thank my parents and little brother for staying calm and believing in me during this challenging and long journey. I am really thankful for letting me do what I always wanted. I also thank my chaiji, naani, chachi, chachu, Abhinav, and Siddharth for all your support and care. I can proudly say that my family is my backbone.

Further, special thanks to another important person, who came as a friend but stayed and is now my husband. Thanks a lot, Dr. Murli K. Manglam. Your support and presence have helped me a lot.

Thanks to the almighty God!

Certificate

This is to certify that the thesis entitled **"Investigating the Position-Sensitive Capabilities of Segmented Germanium Detectors using Gamma Imager"**, submitted by **Arzoo Sharma (2017PHZ0005)** for the award of the degree of **Doctor of Philosophy** of Indian Institute of Technology Ropar, is a record of bonafide research work carried out under my guidance and supervision. To the best of my knowledge and belief, the work presented in this thesis is original and has not been submitted, either in part or full, for the award of any other degree, diploma, fellowship, associateship, or similar title of any university or institution.

In my opinion, the thesis has reached the standard of fulfilling the requirements of the regulations relating to the Degree.

Dr. Pushpendra P. Singh
Department of Physics
Indian Institute of Technology Ropar
Rupnagar, Punjab - 140001, India

Date: June 19, 2023

Lay Summary

In recent years, gamma-spectroscopy has advanced with the development of highly segmented germanium detectors and high-end pulse processing electronics. The segmented germanium detectors, popularly known as tracking detectors, are capable of gamma-ray tracking based on pulse shape analysis. Due to the complexity of signals/pulses in such segmented detectors, obtaining their full 3-dimensional characterization/scan is necessary to achieve at each gamma interaction point inside the detector. The primary aim of this thesis is to develop a one-shot scanning system, a gamma imager, for interdisciplinary applications. In order to characterize a planar segmented germanium detector, the detector has been scanned employing GSI Scanner at the GSI Helmholtzzentrum für Schwerionenforschung, Darmstadt, Germany. The planar detector will be used as an active stopper in upcoming DEcay SPECtroscopy (DESPEC) experiments. The gamma imaging analysis has been performed using pulse shape analysis by looking at pulses for all interactions on an event-by-event basis to determine the gamma-ray interaction coordinates. Further, efforts have been made to develop a new gamma-imager to be deployed in India at IIT Ropar in collaboration with GSI - Germany. The aim is to develop a fast and improved gamma imager and employ this for scanning tracking detectors to understand their electric field distribution, gamma interaction locations, defects, etc. The work is an R&D for future scanning device development with simple configuration and advanced readout electronics. The characterization of the new gamma imager has been performed, and the results show a position resolution of the order of ≈ 1 mm. It may be pointed out that the gamma-scanning system/imager has applications in medical imaging, quantum sensing, homeland security, the oil and natural gas industry, and deep sea exploration, to name a few.

Abstract

In recent years, many efforts have been devoted towards the development of advanced gamma-spectroscopy detectors and sophisticated pulse-processing electronics. A crucial breakthrough in the domain of gamma-spectroscopy has been achieved after the development of highly segmented germanium detectors. Detector segmentation is essential in determining gamma-ray interaction location using Pulse Shape Analysis (PSA). The experimental dataset of traces obtained using various standard gamma sources provided a more realistic tracking algorithm to determine energy and 3-D point of interaction for each event. The PSA technique has been used to achieve energy and 3-D point of gamma interaction depending upon the amplitude of the pulse and its shape at each electrode. The prime feature of locating a point of interaction is that the moving charge induces a charge on the electrode, and based on the properties of electrical segmentation, an image charge is produced on the neighboring/adjacent segment. Due to the complexity of signals/pulses in the segmented detectors, obtaining their full 3-Dimensional (3-D) characterization is necessary.

Therefore, dedicated gamma scanning systems/imagers have been developed employing various novel approaches for gamma-ray interaction location determination. The primary aim of this thesis has been to develop a one-shot scanning system based on a collimation-free scanning technique. The thesis comprises two sets of investigations and developments:

1. In the first set of investigations, the performance test of a planar segmented germanium detector has been performed at GSI Germany. The primary motivation of this work is to prepare the detector deployed as an implantation detector in future DEcay SPECtroscopy (DESPEC) experiments to be performed at the Facility for Antiproton and Ion Research (FAIR) in Germany. The detector under study is a double-sided orthogonal strip detector comprised of ten strips per two opposite sides in horizontal and vertical directions. For its scanning, an existing GSI scanner facility has been used. The GSI scanner consists of a position-sensitive scintillator detector, *i.e.*, LYSO scintillator coupled with a photomultiplier tube with a mesh of 16 X and 16 Y anodes, and a ^{22}Na standard gamma source. The principle of scanning is positron annihilation correlation and the analysis of pulse shape comparison scan. Further, ^{241}Am source scanning has been performed at steps of 1 mm using a lead (Pb) collimator having a hole of diameter 1 mm. The data analysis has been carried out to determine the performance of the planar germanium detector towards the incoming gamma-rays. The gamma interaction depth has been studied by calculating the rise-time of traces stored for each gamma interaction point inside the detector volume, providing $\approx$ 1 mm resolution along the depth. The position resolution of the detector in lateral directions, determined using the amplitude difference of the transient charges, has also been found to be $\approx$ 1 mm.

2. Considering the ongoing efforts of the Indian gamma-spectroscopy commu-

nity to get an AGATA-like array in India, we initiated the development of a gamma imager at IIT Ropar in collaboration with GSI, Germany. The aim of the ongoing R&D is to develop a one-shot scanning technique and employ the device for scanning highly segmented germanium detectors to achieve the gamma interaction locations, electric field distribution, and defects. The prime aim is to develop a gamma imager with simple yet high-end electronics, higher gain, and compact hardware inclusion as an advancement over the existing gamma scanning/imager systems. In this thesis, a position-sensitive detector, i.e., LYSO monolithic scintillator crystal of diameter 7 cm and thickness 3 mm coupled with the matrix of 96 silicon photomultipliers of 3 mm x 3 mm dimensions, has been developed. The testing/characterization of the detector has been performed at GSI, Germany, to understand detector properties and determine its position resolution. In the first step, the test was performed with 24 detector channels employing a ^{22}Na standard gamma source. However, the second test was performed using a coincidence setup between the existing GSI scanner and the new imager. The preliminary test results have been analyzed and discussed for detector position resolution, using differences in amplitudes at the neighboring segments.

Keywords: Position-sensitive detector, Double-sided strip detector, Planar segmented detector, Pulse shape analysis, Gamma imager/scanner, LYSO(Ce) scintillator, Silicon photomultiplier.

List of Publications

International Journals

1. **Arzoo Sharma**, R. Palit, T. Habermann, J. Gerl, I. Kojouharov, H. Schaffner, P. Herrmann, H.J. Wollersheim, S. Saha, Biswajit Das, P. Dey, R. Donthi, B.S. Naidu, S. Mandal, Pushpendra P. Singh, *Performance test of a position sensitive planar germanium detector for phase-III DESPEC experiments*
   Nucl. Instrum. Methods A, 1051 (2023) 168233.

2. **Arzoo Sharma**, R. Palit, I. Kojouharov, J. Gerl, M. Górska, H. Schaffner, T. Habermann, S. Saha, Biswajit Das, P. Dey, R. Donthi, B.S. Naidu, S. Mandal, Pushpendra P. Singh, *Scanning of a Double-Sided Germanium Strip Detector*
   Euro. Phys. Journal, WoC 253 (2021) 11009.

3. Arshiya Sood, G. R. Umapathy, **A. Sharma**, S. R. Abhilash, S. Ojha, D. Kabiraj, A. Banerjee, Pushpendra P. Singh, *Self-supporting thin Tin targets fabricated by ultra-high vacuum evaporation for heavy-ion reactions*
   Vacuum 172 (2020) 109107.

4. Rudra N. Sahoo, Malika Kaushik, Arshiya Sood, Pawan Kumar, **Arzoo Sharma**, Swati Thakur, Pushpendra P. Singh, P. K. Raina, Md. M. Shaikh, R. Biswas, A. Yadav, J. Gehlot, S. Nath, N. Madhavan, V. Srivastava, M. K. Sharma, B. P. Singh, R. Prasad, A. Rani, A. Banerjee, U. Gupta, N. K. Deb, and B. J. Roy, *Sub-barrier fusion in the 37Cl+130Te system*
   Physical Review C 99 (2019), 024607.

5. Arshiya Sood, Swati Thakur, **Arzoo Sharma**, Vijay R. Sharma, Abhishek Yadav, Manoj K. Sharma, B.P. Singh, R. Kumar, R.K. Bhowmik and Pushpendra P. Singh, *Disentangling complete and incomplete fusion events in 12C + 169Tm reaction by spin-distribution measurements*
   J. Phys. G: Nucl. Part. Phys. 48 (2020), 025105.

6. Rudra N. Sahoo, Malika Kaushik, Arshiya Sood, **Arzoo Sharma**, Swati Thakur, Pawan Kumar, Md. M. Shaikh, R. Biswas, Abhishek Yadav, Manoj K. Sharma, J. Gehlot, S. Nath, N. Madhavan, R. G. Pillay, E. M. Kozulin, G. N. Knyazheva, K. V. Novikov, and Pushpendra P. Singh, *Role of neutron transfer in sub-barrier fusion*
   Physical Review C 102 (2020), 024615.

National / International Conference Proceedings

1. **Arzoo Sharma**, R. Palit, I. Kojouharov, J. Gerl, M. Górska, H. Schaffner, T. Habermann, S. Saha, Biswajit Das, P. Dey, R. Donthi, B.S. Naidu, S. Mandal, Pushpendra P. Singh, *Position Sensitivity Study of Double Sided Germanium Strip detector Using Coincidence Method*
   Proceedings of the DAE Symp. on Nucl. Phys. 65 (2021).

2. Rudra N. Sahoo, Malika Kaushik, Arshiya Sood, Pawan Kumar, **Arzoo Sharma**, Swati Thakur, Pushpendra P. Singh, P. K. Raina, Rohan Biswas, Abhishek Yadav, J. Gehlot, S. Nath, N. Madhavan, Md. Moin Shaikh, Manoj K. Sharma, B. J. Roy, Anjali Rani, A. Banerjee, Unnati Gupta, Nabendu K. Deb, B. P. Singh, R. Prasad, *Effect of coupling on sub-barrier fusion: The case of 37 Cl + 130 Te Systems*
Proceedings of the DAE Symp. on Nucl. Phys. 63 (2018), 492.

Abbreviations and Notations

The list of notations and abbreviations used in this thesis are summarised here.

Abbreviations

RIBs	Radioactive Ion Beams
GSI	Gesellschaft für Schwerionenforschung
GANIL	Grand Accélérateur National d'Ions Lourds
TIFR	Tata Institute of Fundamental Research
GRETINA	Gamma-Ray Energy Tracking In-beam Nuclear Array
AGATA	Advanced GAmma Tracking Array
HPGe	High Purity Germanium
PSA	Pulse Shape Analysis
NSCL	National Superconducting Cyclotron Laboratory
DESPEC	DEcay SPECtroscopy
FAIR	Facility for Antiproton and Ion Research
IIT	Indian Institute of Technology
CS	Compton Scattering
PP	Pair Production
NIST	National Institute of Standards and Technology
PMT	PhotoMultiplier Tube
SiPM	Silicon Photomultiplier
SPADs	Single PhotoAvalanche Diodes
FET	Field Effect Transistor
FWHM	Full Width at Half Maximum
SIGMA	Segmented Inverted coaxial GerMAnium
CT	Computed Tomography
MRI	Magnetic Resonance Imaging
SPECT	Single Photon Emission Computed Tomography
PET	Positron Emission Tomography
DCR	Dark Count Rate
PSCS	Pulse Shape Comparison Scan
PAC	Positron Annihilation Correlation
SALSA	SALamanca Scanning Array
PSPGe	Position-Sensitive Planar Germanium
GO4	GSI Object Oriented On-line Off-line
PSD	Position-Sensitive Detector
LYSO(Ce)	Cerium-doped Lutetium Yttrium Orthosilicate
SiPM	Silicon PhotoMultiplier
TOT	Time Over Threshold
V	Volts
QDC	Charge-to-Digital Convertor
PSD	Position Sensitive Detector

Symbol	
ϵ	Dielectric constant of the medium
ϕ	potential
v_d	drift velocity of the particle
e^-	Electron
e^+	Positron
γ	Gamma
χ^2	Chi-square

Contents

List of Figures

List of Tables

Chapter 1

Interactions of Gamma-rays with Matter and their Detection

The interaction of gamma-rays with matter is often described primarily by three distinct processes, i.e., photoelectric effect, Compton scattering, and pair production, in which gamma-rays lose their identity, and there is a redistribution of energy into a different phenomenon. Generally, in Photoelectric Effect (Photoelectric effect), the incident photon falling onto an atom is completely absorbed by it, followed by the emission of an electron. The kinetic energy of the electron depends upon the incident photon energy and the work function or the binding energy of the electron in that shell. The process of Photoelectric effect takes place from the most tightly bound shell of the atom, i.e., k shell, which has a maximum probability to emit photo-electrons as it is closest to the nucleus. However, Compton Scattering (CS), the most dominant interaction process in terms of the probability in a wide energy range, 150 keV to 8 MeV, in which the incoming gamma-rays are elastically scattered (the total energy is conserved) from a free electron in one of the atomic shells and gets deflected at a certain angle. The energy of the incident photon is re-distributed into the kinetic energy of the electron and the energy of the scattered photon. Pair Production (PP) is the phenomenon in which the energy of gamma-rays is transformed into matter through the production of an electron and a positron. The phenomenon is pronounced at higher gamma-ray energies, exceeding twice the rest mass energy of an electron. The photon interacting inside the detector disappears, producing electron-positron pair. To conserve energy and momentum, the process of PP takes place in the vicinity of the nucleus. Schematic representation of the interaction of gamma-rays with a Silicon atom leading to (a) Photoelectric Effect (Photoelectric), (b) Pair Production (PP), and (c) Compton Scattering (CS) is shown in 1.1. The energies of the incident and the scattered photon are denoted by E_0 and E, respectively.

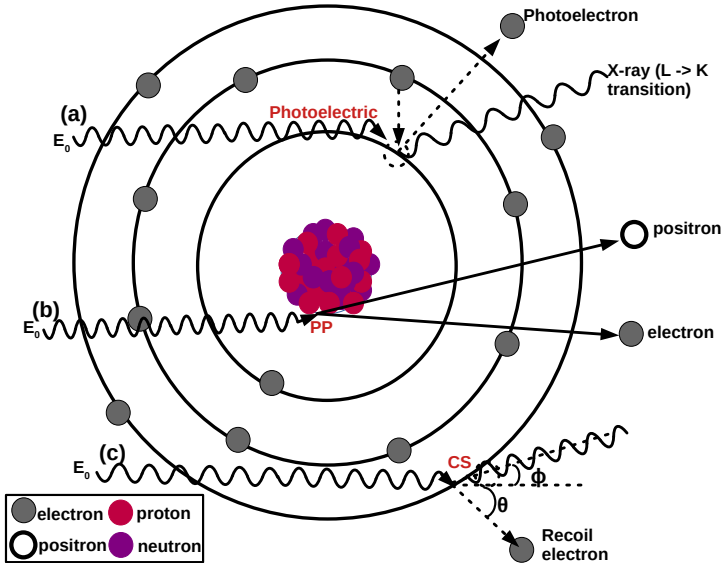

Fig. 1.1. Schematic representation of gamma interactions with Silicon atom leading to (a) Photoelectric Effect (Photoelectric), (b) Pair Production (PP), and (c) Compton Scattering (CS). The incident photon energy is denoted by E_0 and scattered photon energy as E.

Further, in order to display how different gamma-rays interaction processes compete with each other at different energies, the probability of gamma-ray interaction processes has been simulated as a function of incident photon energy in germanium matter, shown in Fig. 1.2(a), using the standard formulation given in ref.[1]. As can be seen from this figure, the weights of different processes depend upon the gamma-rays interaction probability. The figure shows the onset and dominance of different processes with varying incident energies. As can be seen from this figure, the probability of different processes, i.e., Photoelectric, CS, and PP, are denoted by red, blue, and black curves, respectively. The Rayleigh Scattering has also been shown in the figure, represented by a green curve, which is pronounced at low energies and for heavy atoms. The comparison of attenuation coefficients for each of the interaction processes, as well as total attenuation as a function of the increasing incident gamma-ray energy, has been represented in Fig. 1.2(b). It shows the contribution of various interaction processes on an absolute scale.

From the figure Fig. 1.2(a), it can be inferred that the Photoelectric effect process is pronounced at lower energies (below 100 keV) as the photoelectric cross-section decreases rapidly with increasing energy. It happens due to reduced time of interaction with the innermost shells of the atom, the underlying feature for the process to take place. Further, the CS process is dominant at the intermediate energies between 100 keV to a few tens of MeV because of the

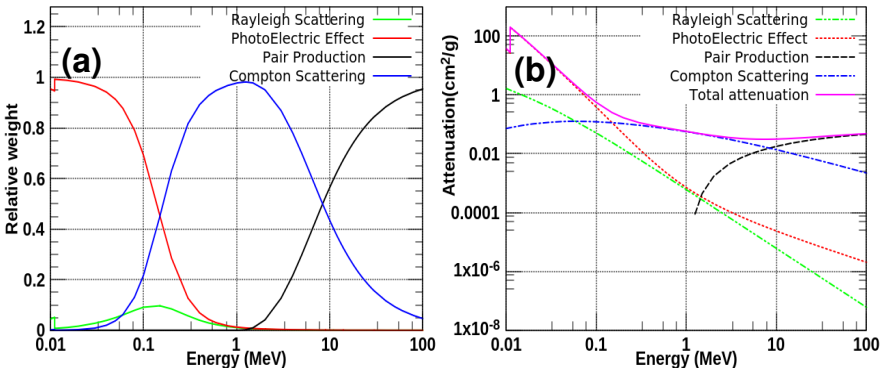

Fig. 1.2. (a) Probability of gamma-ray interaction process as a function of incident photon energy in germanium matter using standard formulation [1]. The Rayleigh Scattering has also been shown in the figure, represented by a green curve, which is pronounced at low energies and for heavy atoms. (b) Comparison of attenuation coefficients for each of the interaction processes, as well as total attenuation (represented by solid line), as a function of the increasing incident gamma-ray energy in germanium.

increased probability of interaction with outer valence electrons. However, at sufficiently high energies, above 1 MeV, the probability of gamma-ray energy converting to mass increases, i.e., through the process of electron-positron pair production, and follows the famous Einstein's mass-energy equivalence equation.

1.1 Gamma-ray Detectors

Gamma-ray detectors are employed to measure radiations emitted from nucleonic excitations. The detector produces an electrical signal, further processed by the accompanied readout electronics, used to measure photon energy and intensity. The energy obtained is characteristic of a specific nucleus, and its intensity describes the source activity. Based on the interaction processes of gamma-rays, different detectors are employed, of which a brief overview of a few detection systems is given in the following sections.

1.1.1 Scintillator Detectors

This detector consists of a scintillator crystal coupled to a photodiode or Photo-Multiplier Tube (PMT). The crystal material exhibits luminance when the ionizing radiation falls on the crystal as the atoms/molecules get excited, emitting light during de-excitation. This light is further absorbed by the photodetector producing electrons via the Photoelectric effect. The phenomenon of light emitted from the scintillator crystal may be classified into two groups depending on

the emission time. If the light emitted after de-excitation occurs within $\approx 10^{-8}$ s, the process is termed fluorescence. Sometimes, the de-excitation gets delayed if it occurs from one of the meta-stable states; depending on the wavelength of a photon being emitted, it is referred to as phosphorescence. The typical combination of a scintillator crystal and a PMT is given in Fig. 1.3.

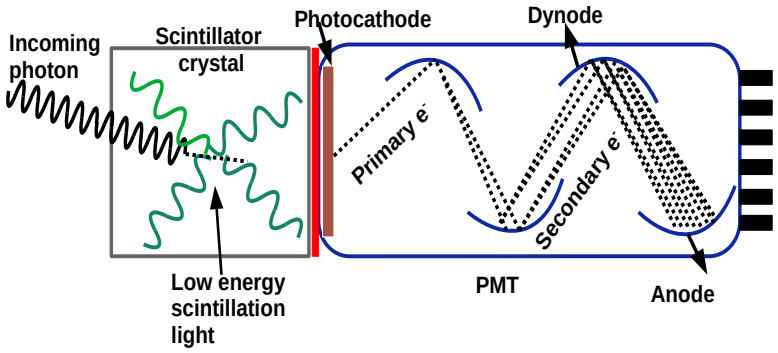

Fig. 1.3. Typical representation of a scintillator detector in which a Scintillator crystal is shown coupled with a photo-multiplier tube (PMT).

As shown in this, the light produced in the scintillator falls on the photo-cathode producing the primary photo-electron, which is guided towards a series of multiple dynode stages through an applied electric field producing secondary electrons. Typically, the electron multiplication is of the order of $\approx 10^7$-10^{10}. The charge signal is then collected at the final anode, processed, and analyzed with the corresponding electronics. The selection of a scintillator is dependent on the following properties:

i High efficiency for light conversion

ii Dense material to stop the incoming gamma-rays for higher photoelectric cross-section as compared to CS.

iii The scintillation light produced is proportional to the number of photons detected, i.e., linear response.

iv Sufficient light collection depends upon whether the material is transparent to its own emission wavelength.

v Shorter decay time implies faster response time to reduce dead time and better time resolution.

vi For efficient light transmission from crystal to PMT, the refractive index of two media shall be approximately similar.

The photodetection efficiency, also termed quantum efficiency, is defined as the number of photo-electrons produced from the incident photons. However, there are events in which de-excitation is not accompanied by the emission of light and is degraded to heat. Such events correspond to the process of quenching. Therefore, during the fabrication of these detectors, optical coupling between the scintillator and PMT requires no impurities or air bubbles trapped in between them. Other than emission through fluorescence or phosphorescence, there is a component added to the scintillator called a wave shifter. It allows the emission of scintillation light at a longer wavelength, mostly in the UV-Visible region, which is useful for good spectral matching between the scintillator and PMT. The scintillators are broadly classified as inorganic and organic scintillators.

i Inorganic scintillators are alkali halides with small impurities acting as activators grown at high temperatures. The emission of light during de-excitation depends upon the electronic band structure. The large band gap between the valence and conduction band leads to mostly the process of quenching. In order to maximize quantum efficiency, the activator creates special sites, and the de-excitation occurs from the activator state to the ground state. The de-excitation is accompanied by the emission of light in the visible region. Some of the widely used scintillators are NaI (Tl) for gamma–ray, CsI (Tl) for protons/alpha, and ZnS (Ag) for α- particle or heavy ion detection.

ii Organic scintillators are compounds of hydrocarbons made of benzene rings. The oscillations occur from the molecular nature of these compounds that creates π-e^{-} structure [18]. The emission of light is through the process of fluorescence (prompt) or phosphorescence (delayed). They have a very fast decay time of the order of a few ns. The wavelength shifter added in a small amount helps to emit light of longer wavelength. Anthracene has the highest quantum efficiency, therefore, better resolution, and stilbene is sensitive to the pulse shape discrimination between electron, proton, or alpha particle radiation.

1.1.2 Semiconductor Detectors

Due to the low radiation energy required to produce electrical signals in semiconductor detectors ≈ 1 eV, the semiconductor detectors outperform the scintillator detectors in which energy required for signal formation is of the order of ≈ 100 eV. The semiconductor detectors offer excellent energy resolution because of increased charge carriers produced, implying lesser statistical fluctuations. The semiconductor detectors are cooled down to the liquid nitrogen temperatures (LN_2), i.e., 77 K, to avoid thermal excitations. Further, the semiconductor materials can be doped with impurities to increase the charge carriers. The dopant impurity substitutes one of the semiconductor atoms in the lattice, adding one extra electron or hole in the material. These extra charge carriers are arranged

at the level within the band gap. Depending upon the type of impurities, tri or pentavalent, the semiconductor is termed p-type or n-type, respectively. When there is a thermal contact between p-type and n-type semiconductors, charge carriers diffuse from one side to another, i.e., electrons move from n-type towards the junction, and holes move from p-type towards the junction. The presence of the charges at the junction creates an electric field. At the junction, the diffusion creates a region with no mobile carriers (devoid of space charge) called the depletion region and is represented in Fig. 1.4 (a). Due to the electric field created in the depletion region, only a few electrons from the n-side can go toward the p-side. A potential barrier is created for the majority carriers; e.g., the potential barrier for Si and Ge is 0.7 eV and 0.3 eV, respectively. Due to the electric field generated, the flow of minority charge carriers, under the influence of the field, will be cancelled by the flow of majority charge carriers. When the external field is applied in the opposite direction of the internal field, the resistance to charge carrier flow is reduced, and the junction is called to be in the forward biasing stage. It has been depicted by $\Delta E - eV$ in the band representation for the p-n junction formed in Fig. 1.4(a). In this figure, E_F denotes the fermi energy, and ΔE represents the energy difference between the conduction bands at the p and n-sides after the formation of the junction, while eV denotes the energy gained after the external field is applied.

The width of the depletion region is dependent upon the concentration of doping impurity and is given by,

$$d = \sqrt{\frac{2\epsilon V_0}{e}\frac{N_A + N_D}{N_A N_D}}, \tag{1.1}$$

where, ϵ= Dielectric constant of the medium, e=electronic charge, V_0= Internal / built-in potential, N_A= No. of Acceptor atoms, N_D= No. of Donor atoms. Depending on the size of the semiconductor detector and the concentration of the dopant, the bias voltage may vary from 500-4000 V. If the doping on the n-side is very high as compared to the p-side, i.e., $N_D \gg N_A$, the space charge region extends further to the p-side and vice-versa. Therefore, the more general form of the equation (1.1) may be written as $d = \sqrt{\frac{2\epsilon V}{eN}}$ [18], for an applied voltage V, and dopant concentration N.

As can be seen in Fig. 1.4(a), the width of the depletion region changes with a change in the external electric field applied, i.e., it reduces with forward biasing. The circuit with a p-n junction is called a diode. When the detector is reverse-biased, the holes move towards the negative potential and electrons toward the positive potential, leaving fewer charge carriers on the two sides. As a result, the width of the depletion region increases further. The application of increased depletion width is that the detector can then be used for radiation study as the charge carrier produced in the depletion region will entirely be due to radiation falling on the detector. It may be pointed out that the width of the depletion region gets enhanced in reverse biasing due to a change in the effective electric field in the depletion region, as shown in Fig. 1.4(b). The same has been depicted by $\Delta E + eV$ in the band representation for the p-n junction formed in

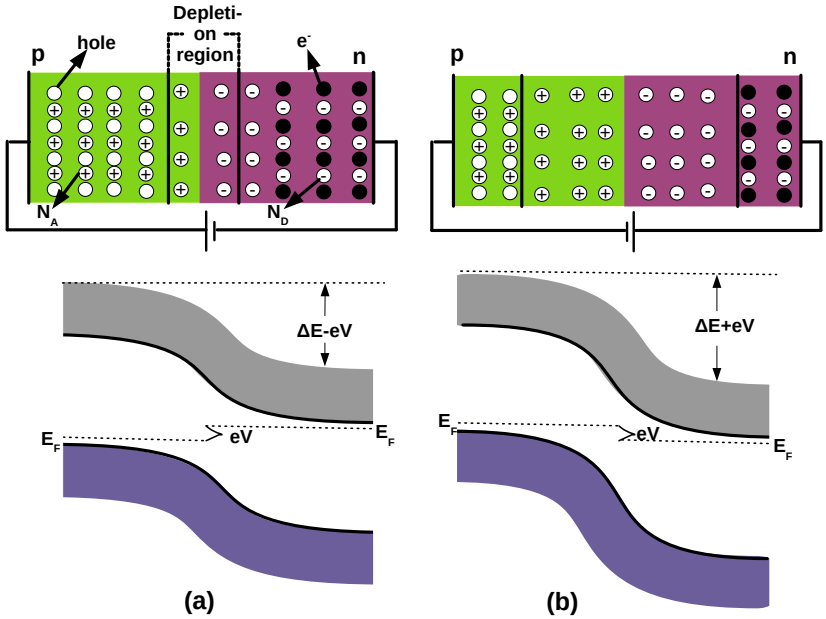

Fig. 1.4. Change of depletion region as a function of bias in a p-n junction diode (a) forward, and (b) reverse bias. The corresponding change in bandgaps is represented below through blue and grey curves.

Fig. 1.4(b). The flow of current in the reverse bias is called reverse saturation current (I_s). It is of the order of nA in silicon devices. It is temperature dependent. I_s increases with an increase in temperature due to minority charge carriers. For Si, for 1 °C rise in temperature, the value of I_s increases by 7%. It is called reverse saturation current because, in reverse biasing, the current does not increase much with an increase in reverse bias. However, there is a voltage at which a lot of minority charge carriers are produced at the depletion region, and the current increases rapidly. This region is called the breakdown region, and the effect is known as the avalanche effect.

1.1.3 High Purity Germanium (HPGe) Detectors

The Si and Ge semiconductor detectors with low band gap energy are broadly used for radiation detection. However, for deeply penetrating radiations, the depletion depth beyond 2-3 mm is difficult to achieve. Therefore, based on the equation $d \propto \sqrt{\frac{1}{N}}$, the decrease in the concentration of impurities (N) leads to the increase in depletion width (d). This leads to the development of High Purity Ge (HPGe) detectors with a reduction in impurity $\approx 10^{8-10}$ atoms/cc (difficult to achieve in the case of Si) using zone refining technique, balancing impurities by adding dopant of an opposite type leading to the production of

either n or p-type HPGe. The HPGe detectors have been produced in different shapes/sizes for different applications; for example, different shapes of planar and coaxial Ge detectors are shown in Fig.1.5 [18]. For completeness, the signal formation in the semiconductor detectors is discussed in Appendix -A of this thesis.

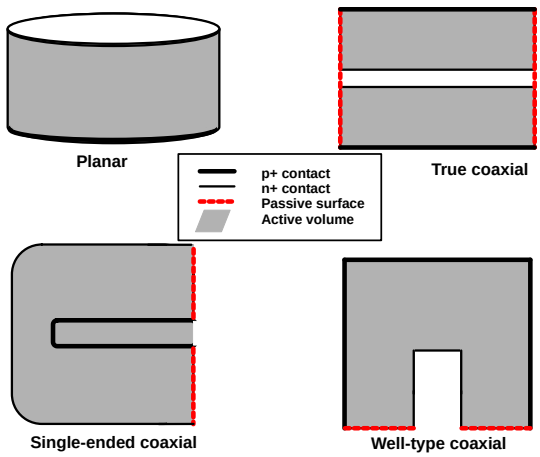

Fig. 1.5. Pictorial representation of different planar and coaxial configurations of HPGe crystals. The n+ and p+ contacts, passive surface, and active volume are self-explanatory in the images.

i In planar configuration, the two electrical contacts (n+ and p+) are made at the opposite flat surface of the disk. The two contacts can be prepared by ion implantation of either donor or acceptor atom on two sides. This technique has an advantage as the contact layer can be made thin, having an advantage for detecting low-energy radiation and X-rays. Most n-type contacts are made using lithium (Li) ion diffusion because of the difficulty in the implantation process and producing a thicker dead layer. In a p-type semiconductor, reverse biasing implies positive voltage on the n+ side w.r.t. p+ side or negative voltage on the p+ side w.r.t. n+ side. At full bias, the detector is fully depleted. The extension of the depletion region would start from the n+ to p+ contact.

ii The width of the depletion region in the planar is limited to 1-2 cm. Therefore, cylindrical or coaxial detectors have been developed to get more width of the depletion region (sensitive to high energy gamma-ray detection). In this geometry, one contact is the outer surface, while the second contact is made by removing the core and making contact at the inner surface. In this configuration, electric field lines are created radially, which helps to achieve a much larger depletion thickness. The core is true coaxial if it extends along the full crystal length. For the more active regions, the

core is extended along one flat end of the crystal; it is called a closed-end coaxial detector.

1.1.4 Silicon Photomultipliers

The Silicon PhotoMultiplier (SiPM) is a matrix of many Single PhotoAvalanche Diodes (SPADs) with a quenching resistor on the Si substrate that works in Geiger mode with a high gain. The SPAD/microcell size may vary from 15-70 μm [24], covering substrate area of $\approx$ 1x1 mm^2/3x3 mm^2. They have added advantage over other p-n junction diodes, i.e., acting as binary photon counters. The intensity of photons impinging the detector can be determined from several pixels firing. Because of small size, high packing density (cell density achieved is $\approx 10^2$-10^3 per mm^2 based upon microcell size), and fast recovery time ($\approx$100 ns), the multiple hit in a single microcell gets reduced appreciably. The accelerated charge carriers produce further secondary charge pairs when the electric field across the detector is more than 10^6 V/cm. Therefore, one photon triggers self occurring ionization cascade. At sufficiently high bias, Si breaks down, producing a high gain signal. Further, a quenching resistor is used to stop the cascade and limit the current drawn by the diode during a breakdown. Hence, it protects the diode to recover for the next signal. The recovery time of SiPM, also denoted by the decay time of a pulse, is given by:

$$\tau_{RC} = C_D(R + Q + R_S N), \tag{1.2}$$

where, C_D = Microcell effective capacitance, R_Q = Quench resistance, N = Number of microcells, R_S = Series resistance. The total charge produced is given as,

$$Q = nGe \tag{1.3}$$

n = Number of fired microcells, G = Gain of the SiPM, e = Electronic charge. The extensive studies show that the gain of SiPM depends upon the overvoltage, a total charge created by the incoming photons, and capacitance, given as,

$$G = \frac{C\delta V}{e}, \tag{1.4}$$

where, δV = V_{bias} - V_B. Important to note that SiPMs are biased to voltages usually greater than 10-25% of breakdown voltage. The number of photons detected is proportional to the number of microcells firing. It is determined by photon detection efficiency (η_{PDE}),

$$\eta_{PDE} = (1 - p_R)Fp_{QE}p_{av}, \tag{1.5}$$

where, p_R = probability of photon reflection at the Si surface. It depends upon the wavelength of the photon.
F = Fill factor used to determine SiPM geometrical area sensitive to light.
p_{QE} = Quantum efficiency. It is the probability that electron-hole pairs will be generated from the photon interaction. p_{av} = It is Geiger efficiency, i.e.,

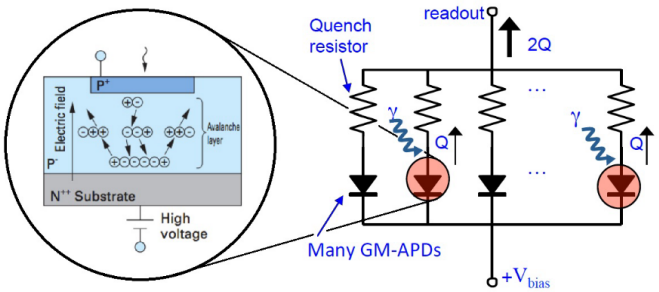

Fig. 1.6. Schematic representation of SiPM working and matrix of SPAD's [2] [3].

the probability avalanche will be generated from primary charge carriers produced in the SiPM. It depends upon wavelength, V_{bias}, and temperature. The energy/wavelength of incoming gamma-ray defines the average absorption thickness in the substrate. It is also said that every 8°C rise in temperature changes SiPM gain by two [25]. It is important to maintain Dark Count Rate (DCR). The pictorial representation of SiPM and its working is shown in Fig. 1.6.

The SiPMs have the advantage of being affordable, easy to transport, and have radiation-hard properties as compared to conventional p-n junction diodes. There can be different SiPM biasing configurations for reverse biasing conditions depending upon whether the output is taken from the p-side (Anode) (implying negative biasing) or n-side (Cathode) (implying positive biasing). The different biasing configurations for cathode/anode readout are shown in Fig. 1.7 (a)-(b).

1.2 This Thesis

The primary objectives of this thesis have been to test the position-sensitive capabilities of a planar germanium detector and to develop a one-shot scanning system/gamma imager based on a collimation-free scanning technique. This thesis comprises two instrumentation projects:

i **Performance test of a position-sensitive planar germanium detector for phase-III DESPEC experiments**: In the first set of investigations, a planar segmented HPGe detector has been characterized to study its charge transport properties using an existing scanner setup at GSI Germany. The aim of this performance test is to prepare the detector for phase-III DEcay SPECtroscopy (DESPEC) experiments at the Facility for Antiproton and Ion Research (FAIR), Germany, as an active implanter. An extensive analysis of the measurements is presented in Chapter 3 of this thesis.

ii **IIT Ropar gamma imager**: In the second phase of this thesis, efforts

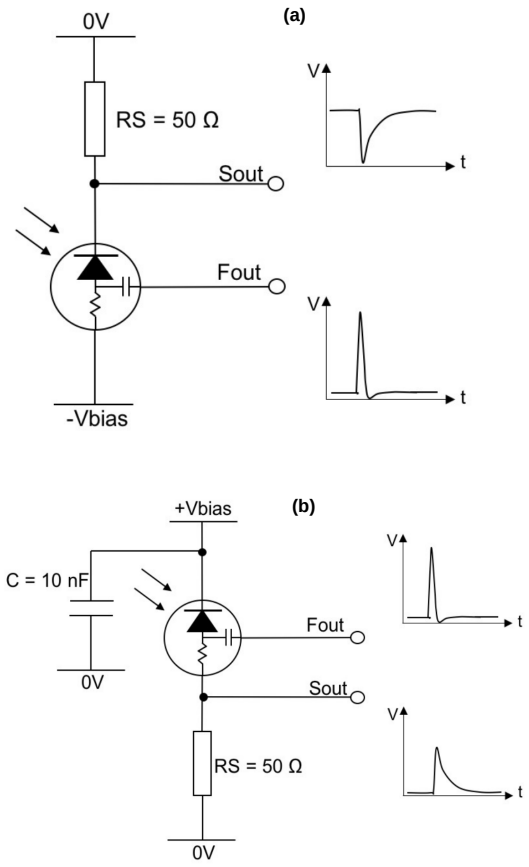

Fig. 1.7. Different bias configurations and corresponding signal outputs for (a) negative and (b) positive biasing detectors. Standard output is represented by Sout, and fast output is Fout. The corresponding pulses have also been shown sideways. RS represents the series resistor.[4]

have been made to develop a new gamma imaging device for IIT Ropar in collaboration with GSI. This R&D has been taken up to complement the efforts being made to set up an AGATA-like array in India. The motivation is to employ the scanning device for tracking detectors with more versatility, advanced readout electronics, and faster scanning time. As an outcome of this work, a one-shot scanning system/gamma imager based on a collimation-free scanning technique has been developed and tested. The primary detector testing and detailed analysis are discussed in Chapter 4 of this thesis.

Chapter 2

Gamma Imaging Devices in Literature

Gamma-spectroscopy offers greater insights into the complex nuclear structure and helps to investigate different astrophysical processes in the universe, such as neutron and proton capture processes, by artificially producing Radioactive Ion Beams (RIBs) in advanced research facilities at GSI (Germany), RIKEN (Japan), GANIL (France) to name a few. The specific nucleus of interest is investigated through gamma-ray detection using a combination/array of many various detectors. The characteristic gamma-rays are analyzed to know properties, like spin, isospin, angular momentum, etc, of a hot rotating nucleus. An advancement in the field of gamma-spectroscopy has been attained after the development of the state-of-the-art segmented germanium detectors, which have been employed in Gamma-Ray Energy Tracking In-beam Nuclear Array (GRETINA) [26] and Advanced GAmma Tracking Array (AGATA) [27], to study exotic nuclei far from the line of stability. Fig. 2.1 displays representative images of (a) AGATA and (b) GRETINA. Both the arrays have 4π solid angle coverage and use High Purity Germanium (HPGe) detectors in which each crystal is segmented into 36 segments along horizontal and vertical directions and also segmented electronically for the purpose of readout. These detectors are based on gamma-ray tracking (for position determination of interaction) and Pulse Shape Analysis (PSA). The main objective of these segmented detectors is to obtain increased efficiency with high solid angle coverage, along with Doppler shift correction leading to better energy resolution, which is caused due to high-velocity RIBs (v$\approx$0.9c).

Owing to the complexity of signals/pulses in these segmented detectors, it is necessary to obtain their full 3-Dimensional (3-D) characterization to store traces (signal/pulse obtained after an interaction) at each interaction location using various standard gamma-ray sources like ^{60}Co, ^{137}Cs, ^{22}Na, ^{57}Co, ^{241}Am, ^{152}Eu, etc. The database of traces is obtained in order to compare the obtained set of traces with an unknown gamma-ray interaction. The uniqueness of the

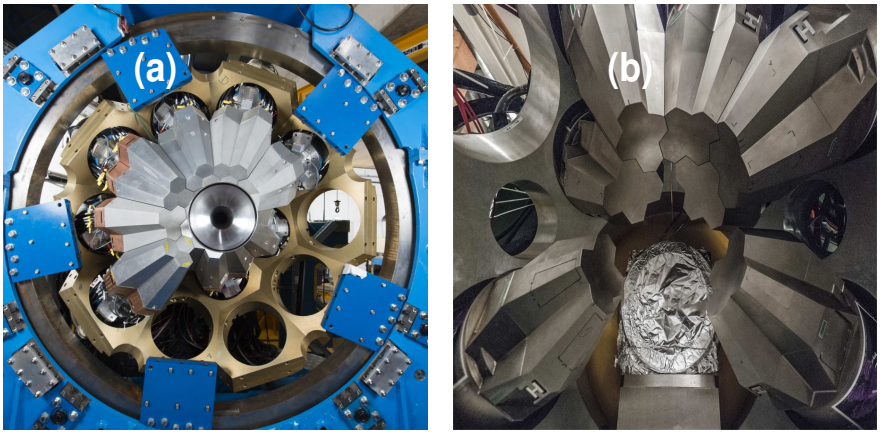

Fig. 2.1. Pictires of (a) AGATA (Advanced GAmma Tracking Array) with 32 HPGe crystals as assembled at GANIL (Grand Accélérateur National d'Ions Lourds), France in September 2016 [5], (b) GRETINA (Gamma-Ray Energy Tracking In-beam Nuclear Array) at NSCL (National Superconducting Cyclotron Laboratory), USA [6].

gamma-ray tracking arrays is to study rare reaction channels obtained with less cross-section in experiments with RIB intensities useful for probing nuclear structure, astrophysics, and fundamental interaction, along with aiding medical imaging [28].

The experimentally obtained dataset of traces using various gamma-ray sources is used to obtain a more realistic tracking algorithm to determine the energy and 3-D point of interaction for each event. This is studied using the PSA technique that depends upon the amplitude of the pulse and its shape at each electrode, i.e., dependent upon the charge induced. The energy deposited by the induced charge is studied using Schokley-Ramo theorem [29]. The moving charge induces a charge on the electrode and based on the properties of electrical segmentation, there is an image charge produced on the neighboring/adjacent segment. This principle is a key feature of locating the point of interaction in such segmented detectors. The results of the grid search algorithm for pulse shape simulation at one of the interaction point in a ring of the AGATA detector are represented in Fig. 2.2. The figure depicts the comparison of the experimental and simulated pulse shapes represented by black and red color, respectively [7]. The overlap between the two sets of pulses indicates the accuracy of the simulated pulse shapes. Along with the simulations, the pulse shapes are stored for various interaction locations via detector scanning, i.e., with real experimental conditions. The characterization of such detectors is necessary to record the signals corresponding to each gamma interaction point inside the detector volume and to find its position resolution [30, 31].

In order to obtain a database of traces in these complex geometry detec-

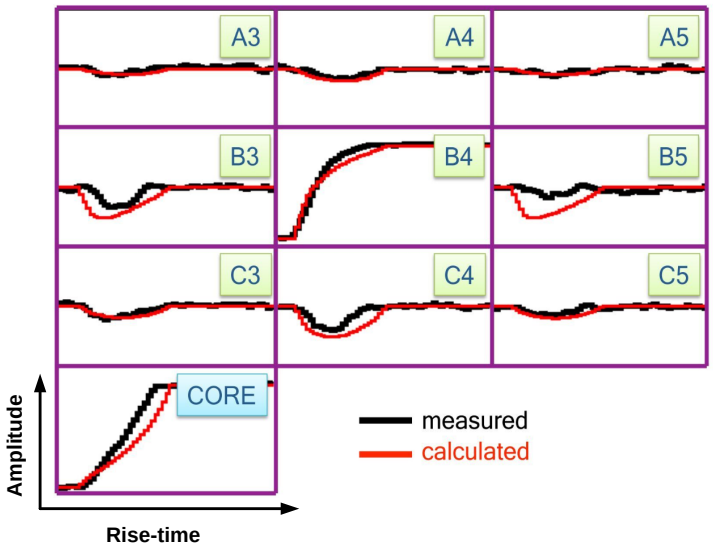

Fig. 2.2. Comparison of the experimental pulse shapes (black) with the simulated pulses (red) obtained using a grid search algorithm for interaction in one of the AGATA segmented rings [7]. The scales along X and Y are linear and rise-time has arbitrary units.

tors, dedicated scanning tables have been developed employing various novel approaches for interaction location determination. The PSA method, based on the charge collection properties of the electrodes, was used to achieve gamma interaction point and position resolution [32, 33]. The pulse formation in a radiation detector has been explained in appendix A. Crespi et al. worked on the algorithm for the identification of interaction location in a segmented detector [32]. The algorithm was based on different slopes produced for different charge carrier motions in the detector, which could generate a number of interactions with a good sensitivity, i.e., 65-95% for 600 keV gamma-ray interaction. Liddick et al. developed a PSA algorithm for a Silicon detector by identifying pile-up pulses from the sequential alpha decay of ^{109}Xe and ^{105}Te isotopes by utilizing the rise-time difference between the two alpha decays [34]. Extensive simulations have been performed to study the performance of a 25-fold segmented HPGe detector [35]. In addition to the PSA performance test, the efficiency and the peak-to-total ratio of the segmented HPGe detector were studied in this work. A Segmented Inverted coaxial GerMAnium (SIGMA) detector has been developed with better energy and position resolution [36]. SIGMA is an electrically segmented HPGe detector with point contact and electrode segmentation technology. For this detector, the grid search algorithm has been employed to find position resolution by considering a simulated pulse for a single interaction point with a random noise added to the pulse. The SIGMA detector has achieved a

position resolution of 0.41 mm for 150 keV gamma energy.

In addition to the availability of highly segmented HPGe detectors, the domain of gamma [37] and beta [38] spectroscopy has been significantly advanced with the R&D of planar segmented HPGe detectors. Following the developments, Khaplanov et al. [37] studied the effect of granularity on the position resolution of a planar HPGe detector. In this study, two different detector geometries, i.e., (a) pixelated detector with 16 pixels on one side and (b) double-sided strip detector with eight strips in the orthogonal directions at opposite faces, were used to determine the gamma interaction point. The PSA analysis showed the benefit of using an orthogonal double-sided strip detector over the pixelated detector. It has been reported in ref. [37] that the higher granularity of the detector is an asset to achieve better position resolution. Further, in a beta-decay spectroscopy experiment [38], a performance test of a planar orthogonal double-sided strip HPGe detector was carried out, in which a 16-fold electrically segmented detector was used as an implantation detector for radioactive isotopes. Rintoul et al.[39] studied the charge collection property of planar double-sided strip detectors through the collimated ^{241}Am source surface scan and ^{137}Cs source side scan and obtained good energy and position resolution using the PSA technique. In ref. [40], the position sensitivity of the segmented planar-type Ge detector was studied using the PSA technique by reconstructing the pulse shape for various interaction locations based on the different properties of electrons and holes traversing the germanium detector. Lee et al. have studied the reconstruction of pulse shapes of a planar p-type detector using Green's function based on induced charge effect [41].

2.1 Gamma Imagers for Interdisciplinary Applications

The gamma imaging techniques are beneficial for various fields such as disease diagnosis, cancer therapy, homeland security, food security, complex tracking array detector scanning, etc. Different imaging techniques are provided in Table 2.1 along with the application domain. MRI is preferred for scanning soft tissues/ligament/brain, CT is preferred for bones and blood vessel imaging, while radioactive SPECT and PET are used for cancer/heart/brain imaging. For some of the applications, it is advised to use more than one technique for better reliability. For example, the diagnosis of the brain using PET/SPECT, in which both techniques are employed. In both cases, one requires to administer the radiotracer that decays via the emission of gamma-rays (single low-energy photon detection in SPECT, and coincident 511 keV photon detection in PET). PET, being expensive as compared to SPECT, provides better spatial resolution [42] or may outstand SPECT in some cases. Herholz et al. studied the comparison and/or correspondence between PET and SPECT scans in an Alzheimer's patient [8]. The results showed more robustness of the PET for qualitative abnormality distinction, as shown in Fig. 2.3. In this image, the red arrows show

that the frontal brain impairment is better depicted with a PET scan. A similar study has been performed by Messa et al. achieving better resolution with PET for Alzheimer's patients by comparing with the healthy person [43].

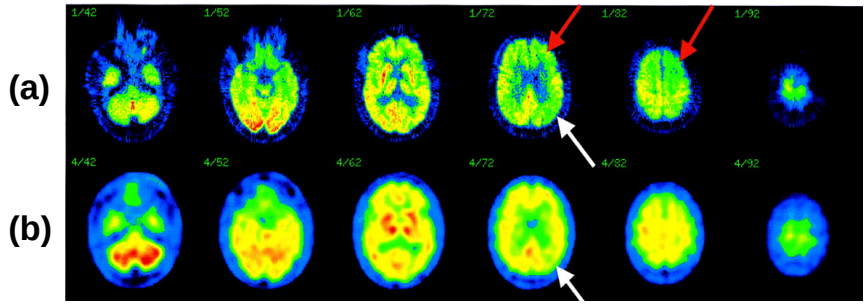

Fig. 2.3. (a) PET (b) SPECT scan of an Alzheimer's disease patient. The red arrow depicts impaired frontal uptake for PET that is not visible in SPECT [8].

Amongst various scanning techniques, PET imaging outstands for sensitivity in picomolecular range [51]. The present thesis also revolves around the discussion of the positron annihilation principle, and it has been discussed in detail in the scope of the present work. Tomography is the term used in the medical field to describe scanning by dividing the area into sections. PET scanning is based on the principle of detection of 511 keV gamma-rays annihilating from a positron source via electromagnetic interaction, i.e.,

$$e^- + e^+ - > \gamma + \gamma \tag{2.1}$$

The 511 keV gamma-rays are detected using an array of detectors used to stop them completely. In the case of PET imaging of a certain organ, a radiotracer (e.g., F-18 fluorodeoxyglucose) is injected inside the patient, which accumulates in the tissue and helps in disease diagnosis. It may have varied doses, however, keeping it as low as possible.

For efficient stopping of 511 keV gamma-rays inside the detector material, a lot of R&D has been undertaken and still continued. The relatively dense and cost-effective detectors used for these applications are the scintillator detectors. The selection of the scintillator is based on its properties (a) to efficiently convert gamma-ray to light, (b) full stopping, (c) fast time response, and (d) good light transmission from crystal to the coupled PMT. The comparison of various scintillator properties for 511 keV gamma-ray detection has been discussed in table 2.2. The attenuation coefficient has been calculated using ref. [1] and considering nominal doping of 0.5 %. The mass attenuation coefficients for all gamma-ray interaction processes are taken from ref. [1]. In the table 2.2, the total attenuation including coherent scattering, i.e., Rayleigh scattering, has been

Table 2.1: Table showing different types of medical imaging techniques [19], [20].

Imaging technique	Source	Working Mechanism	Probe	Spatial Resolution (Reference)	Ionizing Radiation Effect	Measurement Time
X-ray CT (Computed Tomography)	X-ray	Detection of x-rays attenuated from the body part to be scanned	High Z material (Iodine/Barium/sulphate)	0.5 mm ([44])	Yes	$\approx$ 1 s
MRI (Magnetic Resonance Imaging)	radio wave	MR scanner measures signal produced by rotating the magnetic field to excite spin/Nuclear magnetic resonance	Paramagnetic (Gd3++), superparamagnetic (Fe_3O_4)	0.5 mm ([45])	No	1 s - 1 h
Ultrasonography	high-frequency sound wave	Transducer detects waves reflected after echo from tissues, and signature from different tissues will be different	Skin	0.5 mm ([46])	No	15 - 45 min
Thermography	Infrared radiation	Measurement of the surface temperature of the skin and able to detect temperature change of the order of 0.05°C	Skin	<0.1 mm ([47])	No	at least 1 h
SPECT (Single Photon Emission Computed Tomography)	γ-ray	Single photon detection using collimator in front of the detector and rotating system by 360°to obtain full image	Tc^{99m}, In^{111}, I^{131}	6 mm ([48])	Yes	1 min
PET (Positron Emission Tomography)	γ-ray	Ring of detectors set up in coincidence to detect annihilating photon at 180°and determine its position	^{18}F, ^{13}N, ^{64}Cu	0.5 mm (using ^{18}F) ([49],[50])	Yes	1 min

Table 2.2: Table showing comparison between various scintillators based upon their properties [21] [22] [23].

Scintillator (Activator)	**Density (g/cm^3)**	**Light Yield/keV**	**Wavelength (nm)**	**Decay time (ns)**	**Attenuation Coefficient for 511 keV (cm^{-1})**	**Refractive Index**	**Ref.**
NaI (Tl)	3.7	55	410	230	0.35	1.85	[52]
CsI (Tl)	4.51	54	550	1000	0.43	2.0	[53]
CsI	4.51	2	315	16	0.43	2.0	[53]
CsI (Na)	4.51	41	550	900	0.43	1.80	[53]
BGO (Ce) ($Bi_4Ge_3O_{12}$:Ce)	7.13	9	480	300	0.96	2.15	[54]
$LaBr_3$ (Ce)	5.06	63	380	16	0.45	1.9	[55]
$LaBr_3$ (Ce+Sr)	5.01	73	385	25	0.44	2.0	[55]
$CeBr_3$	5.1	60	380	19	0.46	2.09	[56]
CeF_3	6.16	4.4	300 (Fast) 340 (Slow)	300 (Fast) 30 (Slow)	0.60	1.62 (Slow)	[57]

Scintillator (Activator)	**Density (g/cm^3)**	**Light Yield/keV**	**Wavelength (nm)**	**Decay time (ns)**	**Attenuation Coefficient for 511 keV (cm^{-1})**	**Refractive Index**	**Ref.**
CaF_2 (Eu)	3.18	30	435	950	0.27	1.47	[58]
BaF_2	4.88	1.9 (Fast) 10 (Slow)	200 (Fast) 310 (Slow)	0.6	0.46	1.54 (Fast) 1.50 (Slow)	[59]
$LaCl_3$	3.86	49	350	28	0.36	1.9	[60]
SrI_2 (Eu)	4.55	115	435	1200	0.42	2.05	[61]
ZnS (Ag)	4.09	50	450	110	0.35	2.36	[62]
$CdWO_4$	7.9	12-15	475	14000	0.88	1	[63]
PWO	8.28	-	430, 520	6,30	1.03	2.16	[64]
GSO (Ce) (Gd_2SiO_5:Ce)	6.7	8-10	430	30-60	0.70	1.85	[65]
LSO (Ce) (Lu_2SiO_5:Ce)	7.4	30	420	40	0.87	1.81	[66]

Scintillator (Activator)	**Density (g/cm^3)**	**Light Yield/keV**	**Wavelength (nm)**	**Decay time (ns)**	**Attenuation Coefficient for 511 keV (cm^{-1})**	**Refractive Index**	**Ref.**
LYSO (Ce) ($Lu_{1.8}Y_{0.2}SiO_5$:Ce)	7.1	33	420	36	0.82	1.82	[67]
YSO (Ce) (Y_2SiO_5:Ce)	4.5	10	420	50-70	0.39	1.8	[68]
CLYC (Ce) (Cs_2LiYCl_6:Ce)	3.31	20	370	1.5E4	0.30	1.81	[69]
LuAG (Ce) ($Lu_3Al_5O_{12}$:Ce)	6.73	25	535	70	0.75	1.84	[70]
LuAG (Pr) ($Lu_3Al_5O_{12}$:Pr)	6.73	22	310	20	0.75	2.03	[71]
YAP (Ce)	5.37	25	370	28	0.46	1.95	[72]
YAG (Ce) ($Y_3Al_5O_{12}$:Ce)	4.55	35	550	70	0.34	1.82	[73]
GaGG (Ce) ($Gd_3Al_2Ga_3O_{12}$:Ce)	6.63	50	520	90	0.65	1.87	[74]

calculated. Although the relative cross-section for coherent scattering is very less pronounced above 100 keV, however, for the sake of completion, it has been considered in the calculations. Based on extensive research, it has been found that among various scintillators, the LYSO(Ce) (Cerium-doped Lutetium Yttrium Orthosilicate) scintillator has high stopping power, fast timing along with impressive light yield. Therefore, in the present work, LYSO(Ce) scintillator has been studied.

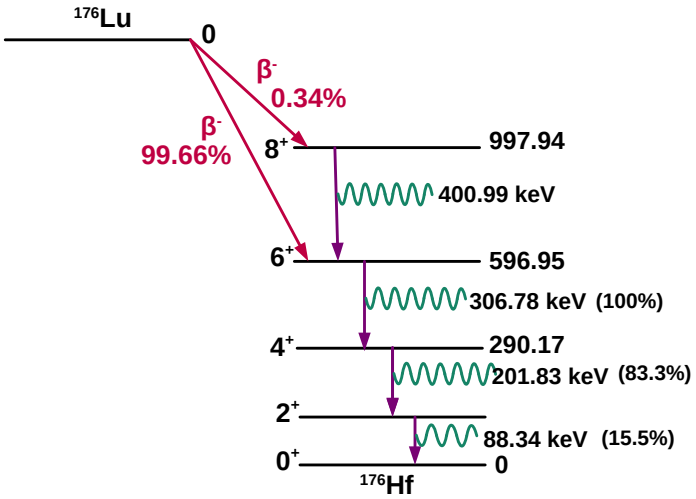

Fig. 2.4. Decay level scheme of ^{176}Lu [9].

The Cerium-doped Lutetium scintillator crystals are widely used for various applications like high energy physics, PET imaging, etc. LYSO(Ce) has 87% of the light yield relative to the NaI(Tl) detector. It contains ^{176}Lu which is radioactive in nature. The decay level scheme of ^{176}Lu is shown in Fig. 2.4, i.e., the excited state to ground state is accompanied via emission of the gamma-ray cascade with energies 88, 202, 307 keV. The absorption efficiency of 3 mm thick LYSO(Ce) crystal at 500 keV is of the order of 25%. The absorption efficiency spectrum as a function of energy for LYSO(Ce) with different thicknesses is represented in Fig. 2.5. The LYSO(Ce) coupled to an Avalanche Photo Diode provides an energy resolution of $\approx$ 17% and quantum efficiency $\approx$ 75% [77]. Further, the crystal is coupled to electronics for efficient light conversion to the electrical signal. There are different types of electronics (coupled to a scintillator) developed over the many years as mentioned in table 2.5. From table 2.5, it is observed that the LYSO coupled to SiPM has a better response in terms of resolution, along with easy-to-handle, simple electronics, and mechanical stability.

In the present work, the LYSO scintillator coupled to 96 SiPM readout has

Table 2.5: Table depicting the difference between the behavior of different readout electronics for a scintillator.

	PIN/Photodiode	**APD**	**PMT**	**SiPM**
Working Principle	electron-hole pair production in depletion region generating photo-current in the presence of applied reverse bias.	It is a photodiode operating under high reverse bias voltage, i.e., breakdown voltage.	Consists of Photo-cathode (convert voltage to photocurrent) and electron multiplication circuit	Works with the same principle as APD as it is an array/matrix of SPADs.
Multiplication Factor	1	10^2	10^6	10^6
Temperature Sensitivity/DCR	Low/	High/	Low/	Low/
Mechanical strength	High	Medium	Low	High
Size	Compact	Compact	Bulky	Compact
Spectral Range (nm)	190-2600	320-1000	300-650	320-900
Bias Voltage (V)	≈5	≈20-150	>1000	≈30
Magnetic sensitivity	No	No	Yes	No
noise	Low	Medium	Low	High
Quantum efficiency with LYSO for emission wavelength	59% [75]	75% [75]	25-40% [75]	43% [76] (for S30)
Time Resolution with LYSO (ps)	slow	764 [77]	≈200 [78]	7 [79]
Energy Resolution with LYSO at 511 keV	worst (not used in medical) (application due to lack) (of internal gain)	17% [77]	11% [78]	9% [80]

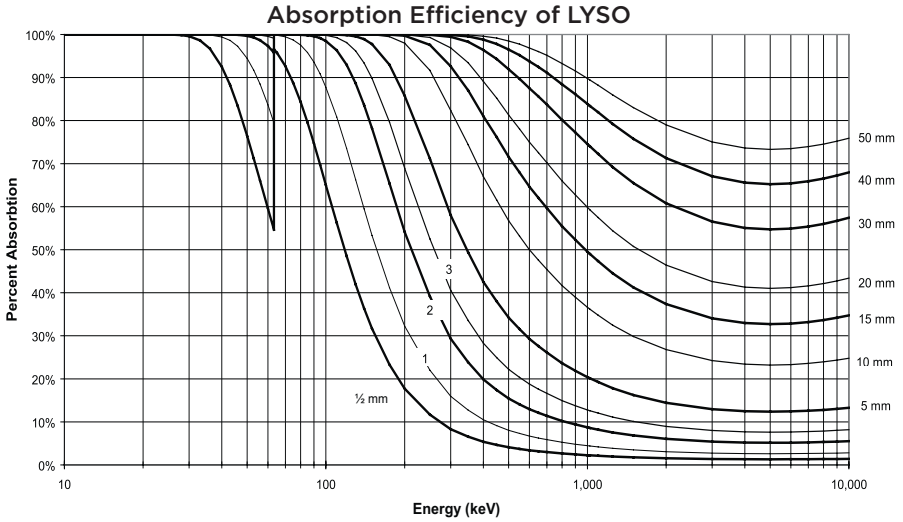

Fig. 2.5. Absorption efficiency for different thicknesses of LYSO(Ce) scintillator as a function of incoming photon energy (from ref. [10]).

been developed and tested in collaboration with GSI, Germany. The aim is to develop a position-sensitive scintillator detector to be employed for interdisciplinary applications. The primary motive is to scan the tracking array detectors, e.g., AGATA. A new campaign has been proposed to get AGATA-like detectors in India. A proposal for the same is being submitted to DST, Government of India.

2.2 Global Status of Gamma Imagers

The complex geometry tracking array detectors require full 3-D characterization. Following is the list of scanning devices:

i **Liverpool Scanning System**: The scanning system consists of a Parker scanning table used to position the gamma-ray source. The source is inserted inside the lead block, acting as a collimator. The table can be positioned along X and Y directions, i.e., radial and azimuthal components in the polar coordinate system, and Z defines the depth. The Z coordinate is studied using scatter detectors placed at 90°to the detector to be scanned. From the Compton scattered events at 90°to the scatter detectors, yields information on the depth of interaction. The scatter detectors consist of BGO and NaI (Tl) scintillator detectors, set up in coincidence with the detector to be scanned. In the article by Dimmock et al. [11], the results of the first scan of the AGATA detector (S002) have been presented. The scan was taken using a 920 MBq ^{137}Cs source, keeping S002 at a fixed

position. The detector was scanned along the front face and side face, as shown in Fig. 2.6(a). The detector 2-D image was reproduced to account for crystallographic effects in the crystal and study the electric field distribution. The position resolution obtained using PSA algorithms was found to be dependent on the electric field simulation code. The first scan results were encouraging, but the time of the full detector scan was challenging, requiring 1-2 months to scan approximately 1200 points.

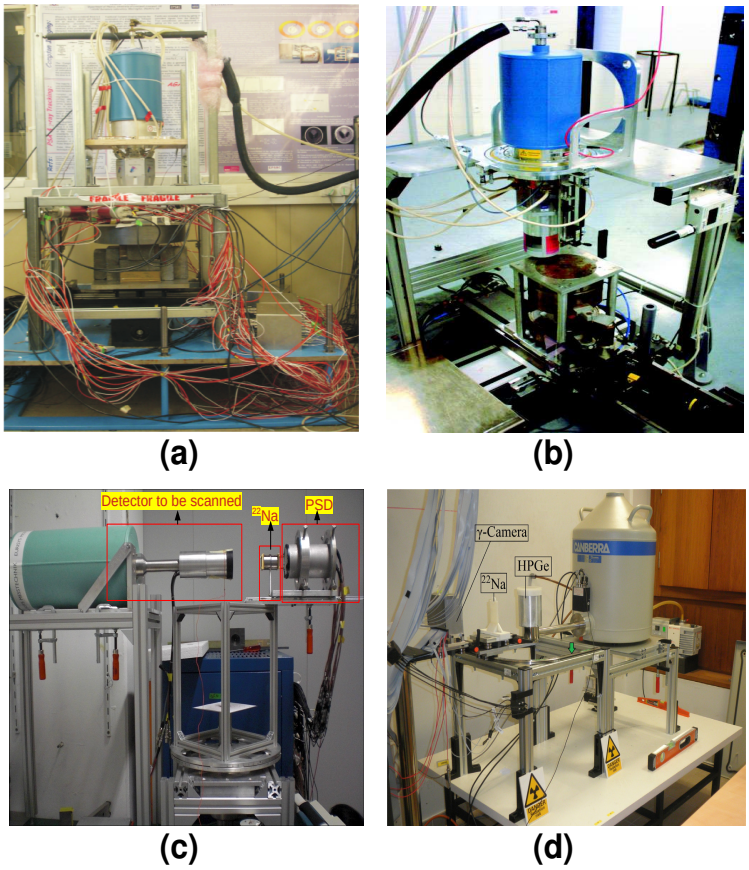

Fig. 2.6. Images of all the scanners (a) Liverpool [11], (b) IPHC [12], (c) GSI [13], (d) Spain SALSA scanning systems [14].

ii **IPHC scanning table**: Another novel scanning approach was developed at IPHC, Strasbourg to perform 3-D scans with good spatial resolution, a large number of scanned points, along with the shorter time of scanning [12]. The scanning method is based on Pulse Shape Comparison

Scan (PSCS) technique. It helps to reconstruct the dataset of traces by comparing pulses in two orthogonal scans (vertical and horizontal geometries). B. De Canditiis et al., have used collimated ^{137}Cs, ^{241}Am, ^{152}Eu sources, where ^{241}Am was used for surface scan, ^{137}Cs for depth scan, and ^{152}Eu for advanced scan with different energies. The setup of the table is shown in Fig. 2.6(b) [81] [12]. The database of traces is obtained for two orthogonal configurations of the AGATA detector and is compared using the chi-square comparison technique. The method allows a full 3-D scan of AGATA in the time frame of 15 days, leading to the creation of a database of 45000 points for a 2 mm scan pitch [12].

iii **GSI Scanning table**: It is a one-shot scanning technique as compared to other point-to-point scanning systems, as described above. Based on the concept of active collimation, a state-of-the-art scanning technique was developed at GSI Helmholtzzentrum für Schwerionenforschung, Germany. The scanner consists of a thin LYSO(Ce) scintillator crystal (cylindrical with dimensions of 7 cm x 3 mm) coupled to a Position-Sensitive PhotoMultiplier Tube (PSPMT) to retain the spatial information of interaction position at the photocathode, represented in Fig. 2.6(c) [13]. The PSPMT is cross-wired consisting of 16 horizontal and 16 vertical anodes from the HAMAMATSU R2486 series. The Individual Multi Anode Readout method (IMAR) has been adopted over the resistive network approach. In the resistive network approach, the anodes are divided into groups and then each group is connected to a resistive charge-dividing network. Therefore, the charge is shared among the anodes. Using the IMAR approach, the readout of all the 16 anodes has been studied independently, which makes it easier to gain match all the anodes individually and provide linear position response across the whole detector [82]. Later, the interaction position is studied using different fitting approaches [13]. The scanning system is based on the principle of Pulse Shape Comparison Scan (PSCS) and Positron Annihilation Correlation (PAC). To scan a gamma-ray detector, the coincidence is set up between the detector and the scanning system using a positron source, ^{22}Na. After positron annihilation, two 511 keV gamma-rays are emitted in opposite directions, used to set up the coincidence between two scanners and the other detector to be scanned. The two orthogonal sets of measurements are taken to find the interaction position using the chi-square minimization technique, i.e., comparing the pulse shapes for the obtained two data sets. This principle, as well as the imaging capabilities of the scanner, makes it a very fast scanning technique. As reported in the literature, it has a spatial resolution of 1 mm along with a large Field Of View (FOV) of 28 cm^2.

iv **Spain SALSA scanner**: Additionally, a gamma-ray scanning system was developed in Spain called Salamanca scanning array (SALSA) [14]. It consists of the LYSO scintillator crystal in cuboidal geometry with dimensions of 52 x 52 x 5 mm^3. The crystal is coupled to PSPMT on the four sides. Each PMT has 64 readout anode outputs, along with one

last dynode output. Therefore, it has in total 260 output channels for signal readout. Similar to the GSI scanner, it is also one shot scanning device based on the principle of PAC and PSCS, using ^{22}Na and comparing pulses obtained in the two orthogonal configurations. The data was obtained for point source scanning along the whole surface of the detector using a collimated source. To reconstruct the image of the scanned positions along the detector surface, an algorithm based on Anger's logic has been used. In the algorithm, the background subtraction is done to get rid of the disturbances due to electronic noise or the light reflection at the edges. Later, the data were fitted with the Gaussian function using ROOT. The position resolution of 0.14 mm has been achieved along the two X and Y directions. It has been used to measure the spatial resolution of various detectors. The analysis shows 1 mm position resolution for the planar germanium detector and 2 mm for the AGATA detector.

Additionally, the gamma scanner development in India is underway owing to efforts to get an AGATA-like array in the country. The recent work shows the initiatives for the development of gamma scanner at Delhi University [83], Tata Institute of Fundamental Research, Mumbai [84], and IIT Ropar 4. In ref. [83], A. Banerjee et al. achieved $\approx$ 1-3 mm position resolution from a setup comprising of LYSO scintillator coupled to R2486 PSPMT. While Biswajit Das et al. reported a GAGG scintillator-based scanner [84], in which a single-crystal coaxial HPGe detector can be scanned, and the results have been compared with the simulations.

2.3 Summary

The growing detector technology is helping in various applications, for e.g., to study exotic nuclei for a better understanding of the universe formation, nuclear abundances, nuclear shell studies, homeland security, medical imaging, etc. The field has progressed with advancements in crystal production, timing and energy resolution, and miniaturization. The advanced segmented detectors have opened new boundaries for gamma-spectroscopy studies and gamma-ray tracking. Detector segmentation is an essential feature to determine interaction location using Pulse Shape Analysis (PSA) as it is sensitive to position. These complex geometry detectors require full 3-D characterization to store a database of pluses for known interaction locations. With this aim, dedicated scanning systems have been developed, contributing to the scanning of such detector arrays and understanding the detector behavior, electric field distribution, defects, etc. With similar motivation, work on characterization techniques, a segmented detector scan, and new scanner development has been carried out and presented in this thesis. The scanner is based on the principle of pulse shape comparison and positron annihilation correlation [85].

Chapter 3

Performance Test of a Position-Sensitive Planar Germanium Detector for Phase-III DESPEC Experiments

The primary motivation for the characterization of the Position-Sensitive Planar Germanium (PSPGe) detector in the present work is to employ the detector as an implantation detector in future Decay SPECtroscopy (DESPEC) experiments. The goal of these experiments is to measure exotic nuclei produced via fragmentation reactions, which are separated and identified through the FRagment Separator (FRS) [86] at GSI. The selected nucleus of interest from FRS is stopped at the active implanter in the DESPEC setup. The general DESPEC setup is shown in Fig. 3.1, consisting of an active implanter, i.e., an AIDA detector (double-sided silicon strip detector) along with a plastic scintillator detector (dedicated to beta particle detection). Further, this assembly is then surrounded by an array of fast scintillators and gamma-ray detectors. The implanted ion undergoes decay via the emission of gamma-rays detected in the array of lanthanum bromide (good timing) and HPGe (good energy resolution) detectors [87]. Due to the high efficiency of the planar germanium detector for low energy gamma-ray/x-ray detection and conversion electron detection, the R&D on the planar configuration has been studied. The detector is segmented, which is an asset for the position determination of the interacting particle. In the present work, the characterization of a planar segmented germanium detector has been performed, and the experimental technique and results are elaborated in the next sections.

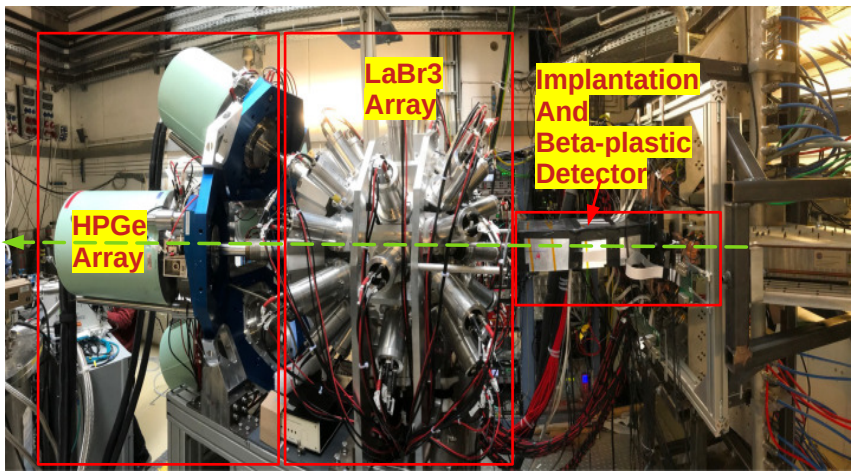

Fig. 3.1. DESPEC setup at GSI for phase-0 campaign.

3.1 Experimental Setup and Methodology

The characterization of a Position-Sensitive Planar Germanium (PSPGe) detector has been carried out at GSI Germany using a scanning setup developed to characterize highly segmented germanium detectors. The GSI scanning system, which consists of a Position-Sensitive Detector (PSD), was deployed in coincidence with the PSPGe detector using a positron source. This technique is helpful in selecting the pulses corresponding to the same gamma interaction event in both detectors within a time window. A detailed description of the PSPGe detector and the experimental setup is given in the following section.

3.1.1 Detector Description

The p-type Planar position-sensitive HPGe detector, produced by Mirion Technologies (former CANBERRA EURISYS), is a double-sided orthogonal strip detector that comprises 10 strips per each side in horizontal and vertical directions. One of the contacts is produced by boron implantation and is DC connected to the preamplifiers, and the other contact is a proprietary Mirion technology and has an AC connection to the preamplifiers. Two guard rings, surrounding the strips at every side, are employed with the aim of reducing the leakage current. The segmentation of the detector is an essential feature in finding the location of gamma interaction by storing pulse shapes for each segment on an event-by-event basis. The physical dimensions of the detector are 6 cm x 6 cm x 2 cm with a thin Aluminium window of thickness 0.5 mm. The layout of the detector segmentation is shown in Fig. 3.2(a), displaying ten segmentations

along the horizontal X (DC connected) and vertical Y-axis (AC connected), and the detector image taken during the experiment is shown in Fig. 3.2(b). The operating bias voltage of the detector at full depletion is −1900 V. The complete detector description is given in Ref. [88], [16].

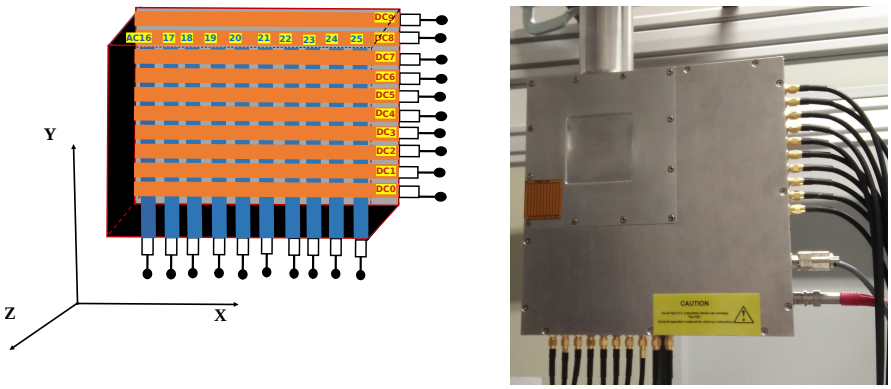

(a) **(b)**

Fig. 3.2. (a) Artistic layout of planar orthogonal double-sided strip HPGe detector. The horizontal and vertical segmentation is indicated by solid orange and blue dotted lines, respectively. The fact that the actual strip size of the strips is much greater than the pitch (of the order of ≈ few micrometers. (b) An image of the corresponding planar HPGe detector used for the present studies.

3.1.2 GSI Scanning Setup

The scanning setup consists of a PSD comprising of Cerium-doped Lutetium Yttrium OrthoSilicate (LYSO) scintillation crystal coupled to a Position-Sensitive Photo-Multiplier Tube (PSPMT). The PSPMT is a mesh of 16 X and 16 Y anodes. In the scanning setup, the detector and positron source ^{22}Na are mounted on an aluminium frame at an optimized distance of 5 cm [13]. In the present work, the PSPGe detector was set up in coincidence with a properly characterized PSD using the ^{22}Na source of activity 169 kBq. The experiment was performed for PSD at an angle 0°, as shown in Fig. 3.3(a) (Set-A), and rotating PSD at an angle 90°in Fig. 3.3(b) (Set-B). The positron source emits two 511 keV gamma-rays emitted in opposite directions after the process of pair annihilation. This figure shows that both gamma-rays are collected in the two opposite-facing detectors. The charge collected in PSD is used to obtain a 2-Dimensional (2-D) image from the coincidence data.

The PSPGe was irradiated with 511 keV gamma-rays obtained from the standard source, selected via its coincidence with the PSD. The source to PSPGe detector distance was 8.6 cm for Set-A and 14.4 cm for Set-B measurements. It may be noted that the source-detector distances were optimized for covering a

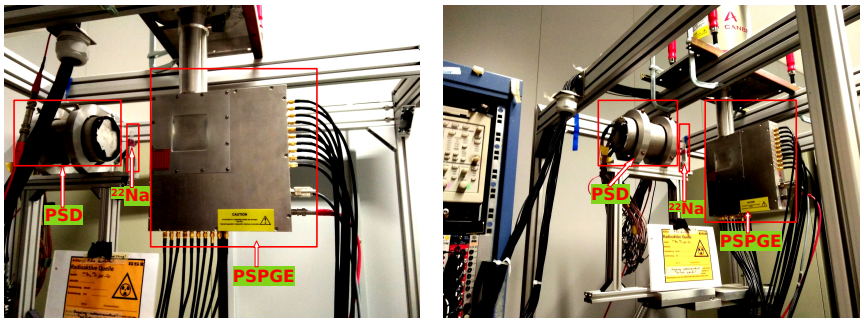

(a) **(b)**

Fig. 3.3. Coincidence setup for PSD and PSPGe at an angle (a) 0° for Set-A, and (b) 90° for Set-B measurements. The detector system and the source are marked inside the rectangular regions for clarity.

whole solid angle around the PSPGe detector. The optimization was made by looking at the ONLINE 2-D images obtained from the PSD using GSI Object Oriented On-line Off-line (GO4) data collection package [89]. The complete electronics block diagram is shown in Fig. 3.4. The 32 anode output signals from the PSD were amplified using Fast Amplifier (N979). The output was fed to Versa Module Eurocard (VME) based multi-event Charge to Digital Convertor (QDC V792) unit with 12-bit resolution. The cathode output from the PSD was used to generate a timing gate, t_1 (depicted in Fig. 3.4), via Constant Fraction Discriminator (CFD - CF4000). The 10 DC and 10 AC outputs of the PSPGe detector were fed to 100 MHz digitizers from Struck Innovative Systeme (SIS3316) modules. It provides information on pulse shape and energy for each interacting gamma-ray on an event-by-event basis. The ADC signal in the SIS digitizer contains ADC FPGA to produce the Moving Average Window (MAW), i.e., the trapezoidal filter, which is used to produce the logic/trigger signal as shown in Fig. 3.5 [15]. The FPGA has a programmable trigger threshold, CFD mode, trigger mode, peaking time (length of MA pulse for moving average unit), and gap time (differentiation time of moving window average unit). Hence, SIS produces the internal trigger from the digitized preamp signal which we get at Trigger Out (TO in electronics schematics). It is a logic pulse that contains information of the OR (OR of the time) of all channels, indicated as time t_2 in Fig. 3.4. t_1 and t_2 were set up in coincidence using the Quad Coincidence unit (CO4001). The data from QDC and SIS3316 was read out using the Multi-Branching Data Acquisition System (MBS). The ENV1 module contains the dead time of the MBS readout, which is put in anti-coincidence with t_1 and t_2 using CO4001. The output was used as an accepted trigger for the QDC and SIS3316 digitizer. This accepted trigger, i.e., Trigger In (TI in electronics schematics that is basically the coincidence between PSD and PSPGe), opens a validation gate, and with the help of delay parameters (controlled through Graphical User Interface (GUI)), the gate covers/validates the

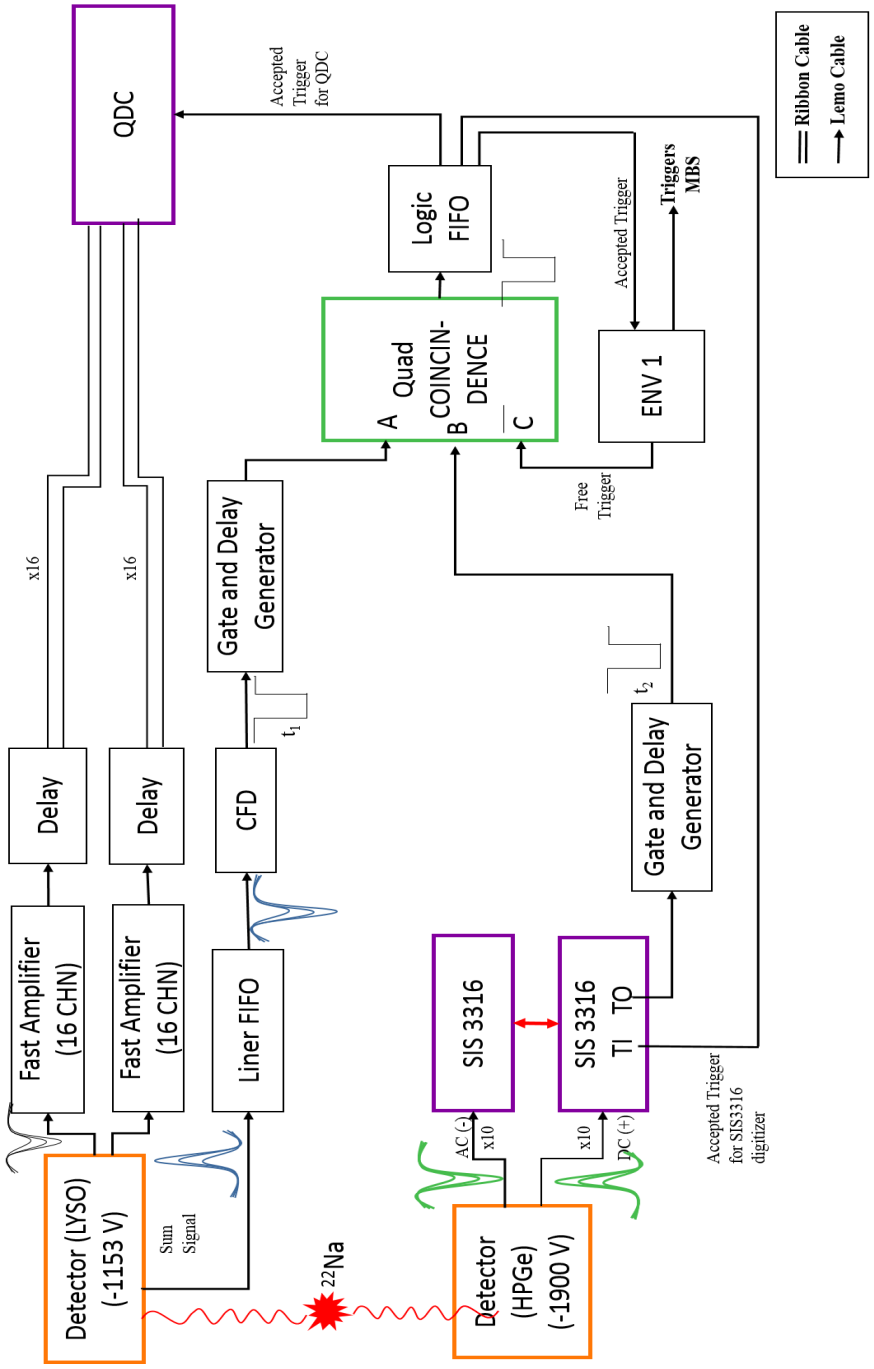

Fig. 3.4. Schematics of the electronics used for coincidence setup.

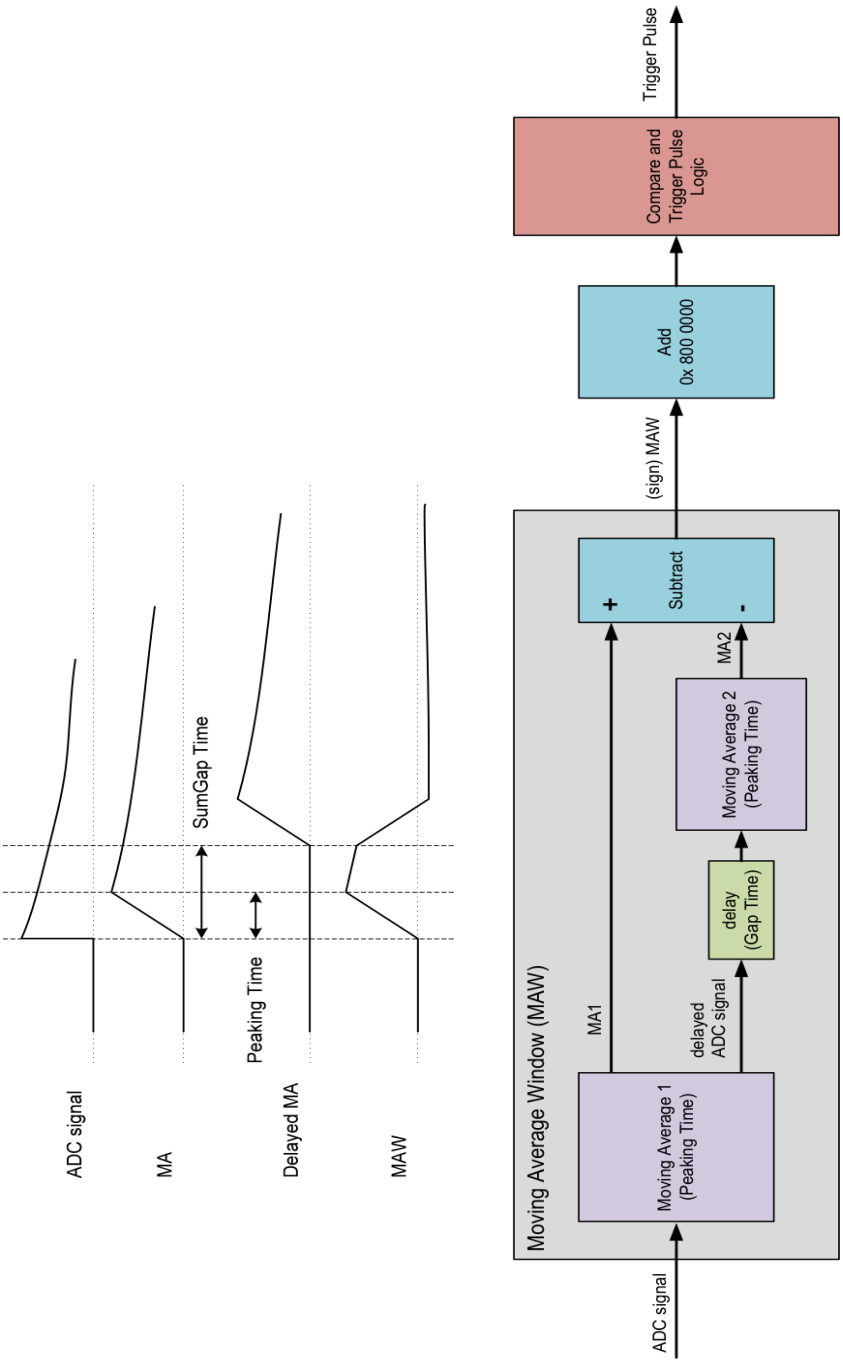

Fig. 3.5. Signal handling and processing in SIS digitizer [15].

internal trigger/digitized detector signal. Therefore, we read only the event that comes with the accepted trigger. The settings of the digitizer were made using a desktop Graphical User Interface (GUI). The SIS GUI settings are shown in appendix B. The monitored data rate was 250 Hz. The data was collected using the Multi Branching System data acquisition (MBS - DAQ) and GO4 for online monitoring.

3.1.3 Collimated Source Scanning

^{241}Am source scanning was performed at steps of 1 mm using a lead collimator with a hole of diameter 1 mm. It is a low-energy source with photopeak energy at 60 keV. The attenuation depth of 60 keV in germanium crystal is 0.6 mm calculated using NIST - XCOM database [1]. Hence, the scan was performed on both sides, i.e., one side with AC strips and the other with DC strips. The detector-to-source distance was kept at 2 mm. The two scans were performed for one of the middle strips and a side strip. The vertical strips, AC21 and AC16, were scanned in the horizontal direction at a fixed vertical position (center). The horizontal strips, DC4 and DC8, were scanned in the vertical direction, at a fixed horizontal position (center). The collimated source holder was kept at the scanning system in the place of ^{22}Na source holder. PSPGe was operated with self OR accepted trigger mode. The scanning table was used to move the source in millimeter steps. In the first step, the center of the strip (to be scanned) was located by moving the source to get the maximum counts in the photopeak, and later, it was moved to either direction covering three positions in the left and three in the right at steps of 1 mm (covering the approximate size of the strip).

3.2 Data Collection and Analysis

The data was collected for two days for Set-A and Set-B positions using MBS. The offline data analysis was performed using GO4 and C++-based ROOT platform [90]. The position resolution of the PSPGe detector has been determined by analyzing pulse shapes at various gamma interaction points inside the detector. As shown in Fig.3.2, the detector is segmented along the horizontal and vertical directions, but not along the depth. Despite this, the position resolution measurements for three coordinates can be extracted independently. In order to find the depth of gamma-ray interaction, a method of small pixel effect has been employed [91]. The depth has been estimated using the rise-time difference between the two opposite surfaces of the double-sided strip detector. For finding position resolution along the lateral faces, the amplitude ratio of the image charge carriers in the neighboring segments is calculated as given in Ref. [92][29].

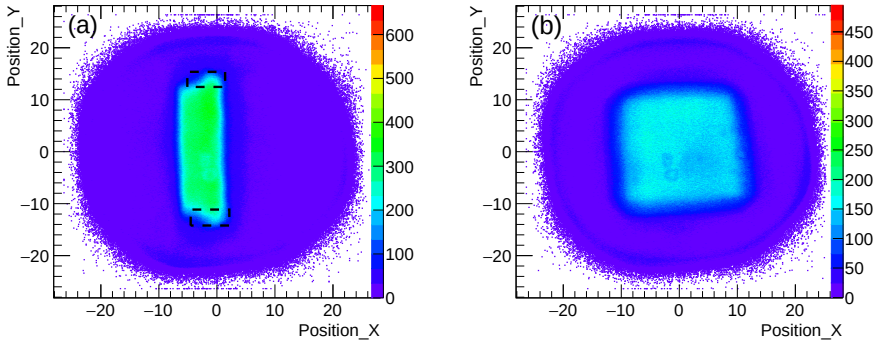

Fig. 3.6. 2D images obtained from PSD for (a) Set-A and, (b) Set-B measurements using centroid method for coincidence setup. The dip at the top and bottom of the image, indicated by a black rectangle, in (a) represents the guard ring (The details are provided in Ref. [16]). The projection of both images has been shown in appendix F as supplementary information.

3.2.1 Key Procedures

- The analysis has been performed to reconstruct the 2-D image from the PSD using the centroid fitting approach. It has been attained through charge collected at X and Y anodes in PSD using QDC. The 2-D images obtained from this analysis are given in Fig. 3.6(a) (for Set-A) and 3.6(b) (for Set-B) representing the depth and the lateral view of the detector, respectively.

- The energy spectrum obtained from the SIS3316 digitizer has been used to select the electrode of interest for further analysis through gating on the Photopeak or Compton edge after calibration.

- For Set-A measurements, the 2-D image is projected onto the X-axis for dividing the axis, as the PSPGe detector is not segmented in depth.

- For Set-B, the strip is further divided using the 2-D image cut to get better position resolution than the segmentation itself. In addition, ^{241}Am collimated source scan data has been analyzed to find the position resolution using 60 kev gamma-ray photopeak. The two source measurements (^{22}Na and ^{241}Am) are independent.

- The 2-D image is projected onto the respective axis to obtain calibration. The calibration of the projected image is performed following the known dimensions of the PSPGe detector. In Set-A, Position_X in PSD image (Fig. 3.6(a)) represents the depth of the PSPGe detector (shown by Z-axis in the Fig. 3.2) [1]. In Set-B, Position_X represents the X-axis of

[1]The depth represents Z-axis in the PSPGe detector. The 2-D image from set-A measure-

the PSPGe detector. The Position_Y indicates the Y-axis in both sets of measurements.

- The traces obtained from the digitizer SIS3316 are further processed as quantified in the literature [93], i.e., performing baseline subtraction, normalization, and finally, the time aligning of the traces.
- Traces have been time-aligned at 10% of the final amplitude, shown in Fig. 3.7.

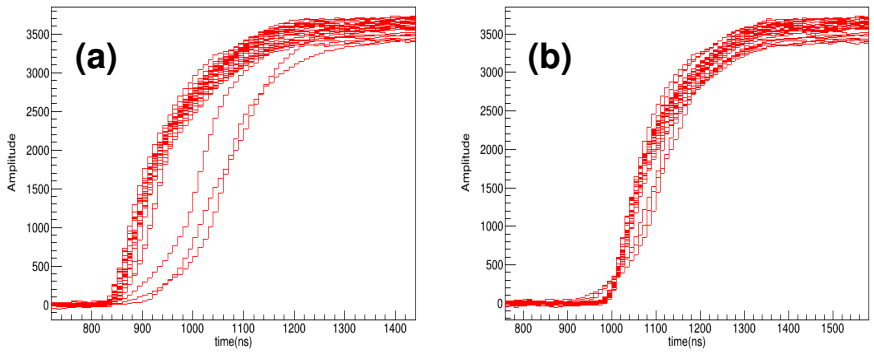

Fig. 3.7. Pulse shapes (a) before and (b) after time alignment.

3.2.2 Depth of Gamma Interactions

The Set-A measurements, performed with PSD at 0°, have been used to calculate gamma interaction depth. It implies that the PSD has been facing the crystal depth as displayed in Fig. 3.3(a). It may be pointed out that the position sensitivity and fast imaging capabilities of PSD help to accomplish the experimental goals solely through one measurement [94]. The 2-D image from PSD is projected on to X-axis and is subdivided into fifteen segments for calibration since there is no segmentation along the detector's depth. The DC and AC strips have been numbered from 0 to 9 and 16 to 25, respectively, as represented in Fig. 3.2. In this work, the analysis has been performed for one middle DC-AC strip and one side DC-AC strip pairs, referred to as DC4 - AC20, and DC0 - AC16, respectively.

The gate on energy helps to understand the response of the detector for the gamma-ray of interest. The energy information obtained from the SIS3316 digitizer has been used to make an energy cut on the 511 keV photopeak to select

ment (depth scan) has DC segments on the left side and AC segments on the right side of the central densely populated detector image.

DC4 and AC20, DC0, and AC16 electrodes. Further, the traces obtained from the energy cut have been studied for each of the fifteen cuts on the 2-D image. The acquired trace information has been used to find the rise time for AC and DC electrodes after processing digitizer pulses for each interaction event in these cuts. The rise-time difference of pulses has been calculated between the front and the back faces to get the depth of the gamma interaction point, which is useful due to the difference in mobility of electrons and holes, implying separate charge collection of the two charge carriers at the respective electrodes. Therefore, the difference in mobility leads to different rise-time values [91] [95]. Tn rise-time has been calculated as a function of depth in the detector, where Tn is defined as the time required for the pulse to reach n% of maximum amplitude - the time required for the pulse to reach 10% of maximum amplitude. The T50 rise-time difference has been calculated between AC20 and DC4, i.e., $T50_{AC20} - T50_{DC4}$, and between AC16 and DC0. i.e., $T50_{AC16} - T50_{DC0}$. The analysis of the results for AC and DC electrodes' behavior along the depth has been discussed analytically in section 4 using χ^2 comparison and rise-time difference.

3.2.3 Lateral Position Resolution

The measurements have been carried out to find the position resolution of the detector along the X and Y directions. Fig. 3.3(b) shows the set-B measurements, in which PSD is positioned at an angle of 90°. The analysis procedure remains the same for processing the trace of the selected strips in the data set. As a representative case, the 2-D image for the Compton edge cut on strip DC4 is given in Fig. 3.8.

The 2-D image for the selected strip (the red dashed rectangular region in Fig. 3.8 is projected onto the Y-axis for DC4 (and for the vertical strip, the selected 2-D image is projected onto the X-axis). This analysis has been performed for DC4 and AC21 segments. The selected segment is sub-divided into seven positions using the projections, where the position difference between each division is considered to be 1 mm, as the strip thickness is 6 mm. The transient charges in the adjacent segments have been analyzed for each position. The applied bias does not affect the induced charge on the electrode produced due to the moving charges as it depends on the instantaneous electric field at each point of its path [29]. For the strip semiconductor detector, the amplitude of the induced charge on an electrode would be lower if it is farther away as compared to the pitch of the electrode. The most pronounced weighting potential would be near the electrode surface. In the case of an orthogonal strip detector, the electrons and holes are collected at the anode and cathode surfaces, respectively.

The image charges are shown in Fig. 3.9, where one of the Compton events is selected in the DC segment, DC4. The corresponding image charges in the neighboring segments are shown in Fig.3.9(a)-(b). As indicated in the figure, the closest neighboring segments, DC3 (strip below DC4) and DC5 (strip above DC4), are represented in blue. The next neighbors, DC2 and DC6, are shown in black, followed by DC1 and DC7 segments in green color. Due to the maximum amplitude of the mirror charge in DC3, it may be inferred that the interaction

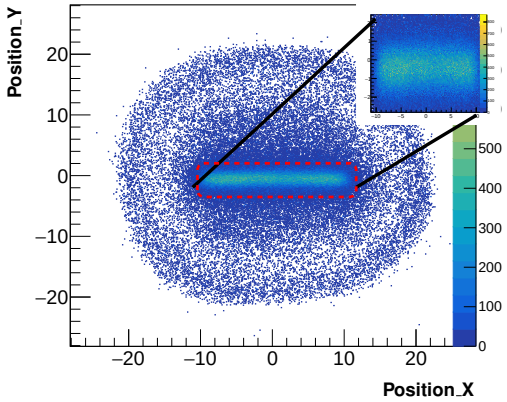

Fig. 3.8. 2-D Image obtained from PSD for Set-B gated on Compton edge of the horizontal electrode, DC4. The image on the top of this image is the zoomed one on a rectangular portion marked with red dashed lines in the center. It has been marked as one of the representative cases to show the boundaries of the electrode selected.

occurred close to the lower edge of DC4. Moreover, it has been observed that corresponding to the moving charge created in DC4, the charge is induced on the far neighbors along with adjacent segments. The amplitude of the induced charge depends on the electrode's hit location, along with the amount of energy deposited by the incoming gamma-ray. The analysis has been further progressed in two steps. First, the 2-D image was constructed for Compton edge cut on both DC4 and AC21 segments, i.e., by selecting the events in which both the strips fire together and eventually, obtaining a corresponding voxel (with a dimension of $\approx$ 6 mm X 6 mm X 2 cm). As a next step, the projection of the 2-D image is further divided into seven segments. As an example for two middle strips, the image has been reproduced, showing the amplitude of image charges in the neighboring strips, given in Fig. 3.10. In these figures, the central part represents an interaction event with two middle strips (DC4 and AC20) firing at the same time, where DC4 is represented by red color and AC20 by black color. The corresponding image charges of the two strips are shown in blue color. The left and right image charges correspond to AC19 and AC21 electrodes. The top and bottom image charges represent the induced charge in DC5 and DC3, respectively. As shown in Fig. 3.10(a), AC20 has a faster rise-time as compared to DC4. The T50 rise-time difference is found to be -40 ns. The 2-D image cut is -1.9<Position_X<-1.5 and 0.5<Position_Y<1 (corresponds to the upper left part of the voxel). For this specific location, it has been found that the polarity of image charges in the neighborhood of AC20 is negative, while the DC4 has positive image charges. The amplitude of image charges in the AC19

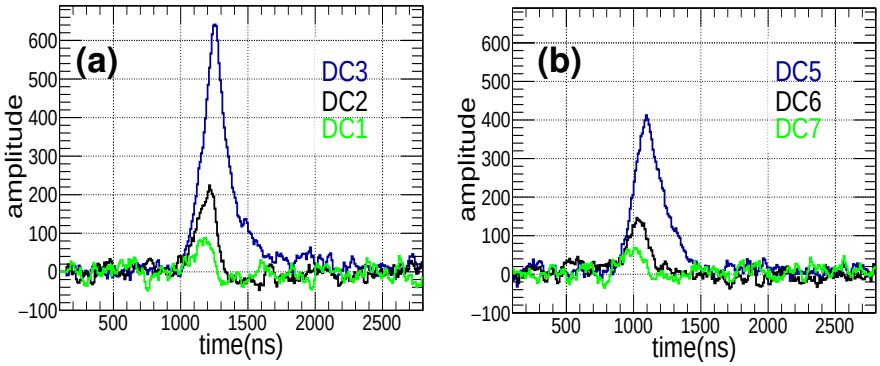

Fig. 3.9. Compton event in DC4, and the corresponding amplitudes of transient charges in the neighboring strips (a) below, and (b) above DC4.

and DC5 segments are high, indicating interaction occurred in the vicinity of these segments. Further, for an event shown in Fig. 3.10(b), DC4 has less rise-time than the AC20 segment. The T50 rise-time difference of 140 ns has been obtained. The 2-D image cut is -0.5<Position_X<0 and 0.5<Position_Y<1, i.e., the upper right voxel. As indicated in the figure, the polarity of image charges in the neighborhood of DC4 is negative, and the polarity of image charges in the AC19 and AC21 segments is positive. The amplitude of the image charges in DC5 and AC21 is more pronounced than in the DC3 and AC19 segments.

This implies that the time difference between the two segments for the defined interaction locations in Fig. 3.10(a)-(b) affects the polarity of the image charges. Hence, the interaction location affects the amplitude of the image charges. Therefore, it may be concluded from Fig. 3.9 and 3.10 that the ratio of the amplitudes in the adjacent of the hit segment can be employed to find the position resolution. It is further pointed out that for all interaction voxels, the gamma-ray interaction depth may have all possibilities to interact, i.e., depth may differ. Moreover, based on different gamma interaction depths, the polarity of image charges will differ. [2]

Additionally, for independent ^{241}Am collimated source scan, the image charges amplitude study has been performed by gating on the 60 keV photopeak energy. Because of the lower penetration depth of 60 keV gamma-rays in germanium, the image charges have been obtained with negative polarity. It indicates the specific rise time difference between the horizontal and vertical strips. For the AC segment scan, the centroid of the T50 rise-time difference distribution plot for each measurement position between DC5 and AC21 obtained is ≈ 5 ($\pm$ 0.5)

[2]Further to note, the 2-D set-B measurement was performed for both orthogonal sides, i.e. one side with vertical strips (AC segments) and the other side with horizontal strips (DC segments). For the vertical strip scan, the AC21 segment has been analysed for position resolution measurement. For the horizontal strip scan, the DC4 segment has been analysed for position resolution measurement.

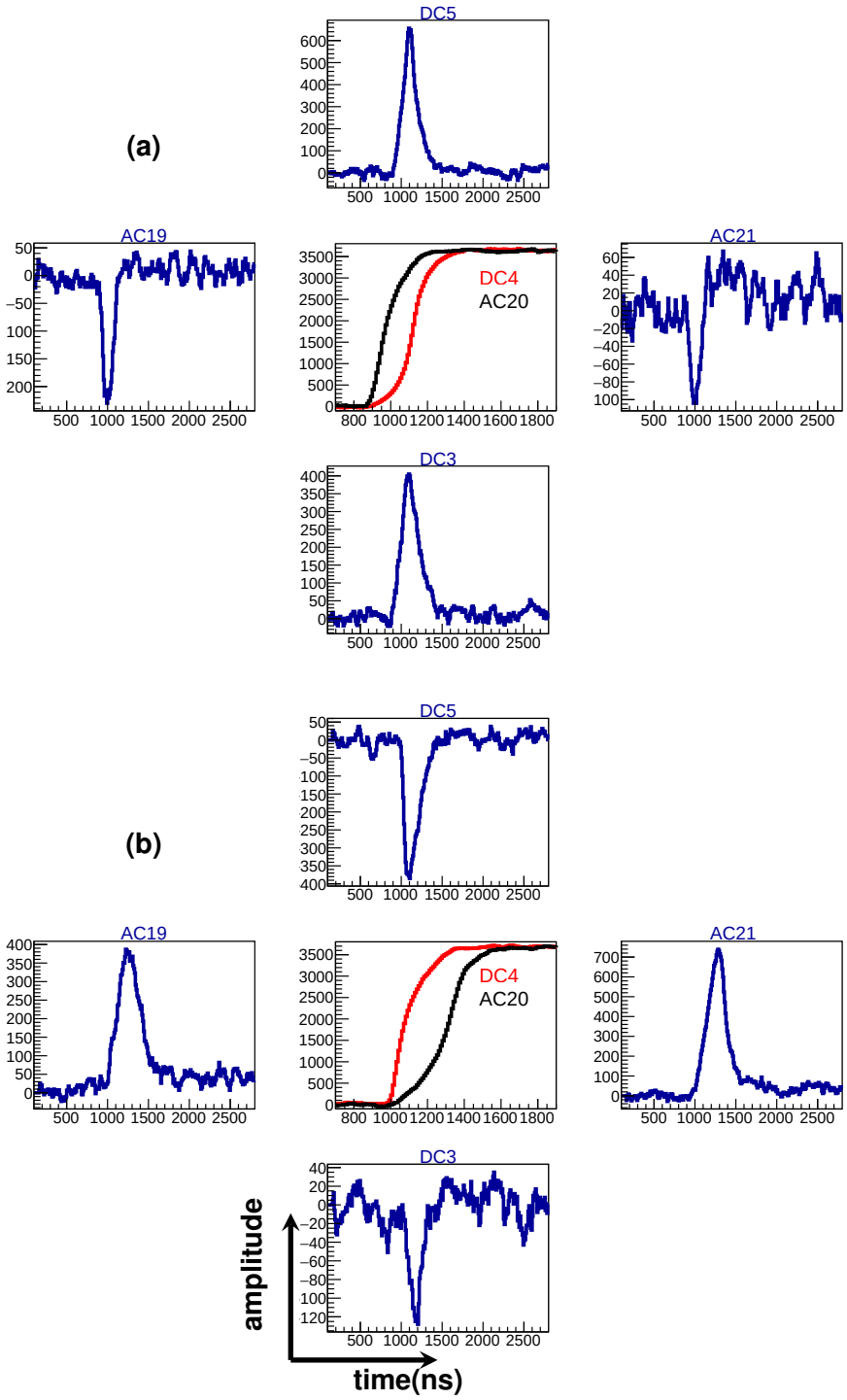

Fig. 3.10. Image Charges obtained by gating on 2-D PSD spectrum (for set-B measurement) in the voxel with 2-D cut given by (a) -1.9<Position_X<-1.5 and 0.5<Position_Y<1 (b) -0.5<Position_X<0 and 0.5<Position_Y<1.

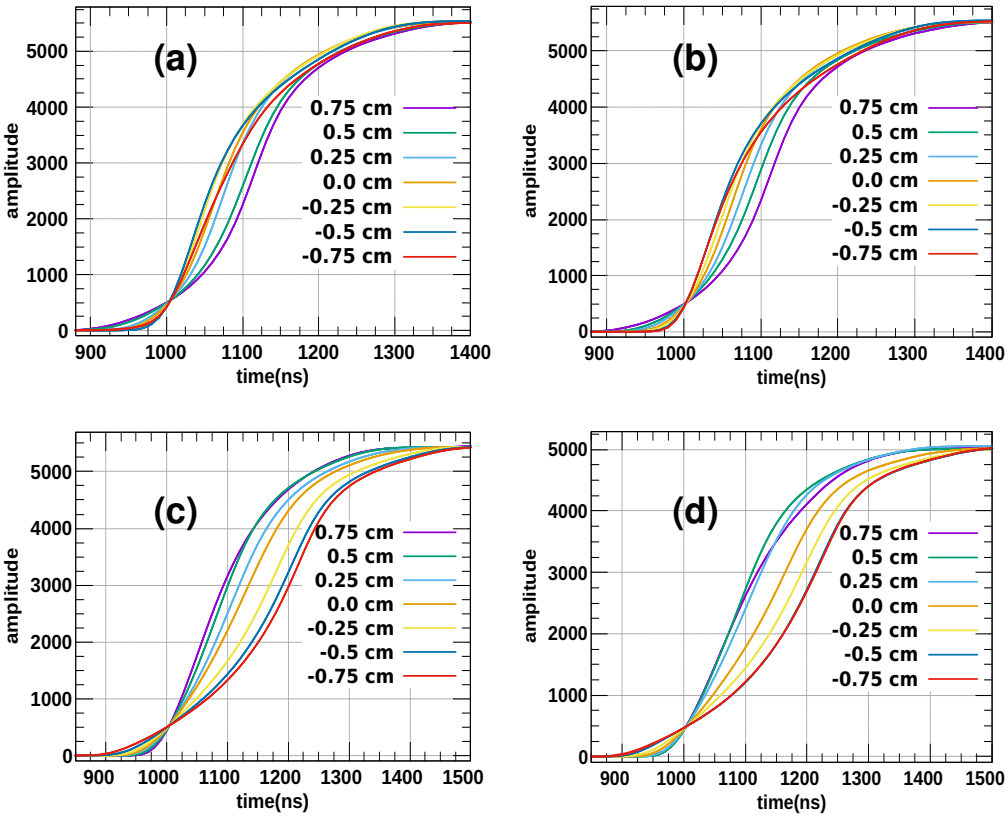

Fig. 3.11. (a) Mean pulse obtained after pulse shape comparison using χ^2 minimization for strip (a) DC0 (b) DC4 (c) AC16 (d) AC20. The legend represents different depth cuts in the 0°scan /set-A 2-D image (depth dimension is 2cm).

ns. For the DC scan, the T50 rise-time difference between DC4 and AC21, it is $\approx$ 140 ($\pm$ 1.5) ns. The amplitudes of the image charges in the neighbourhood of the scanned segment have been analysed and discussed in section 4.

3.3 Results and Discussion

The segmentation of the PSPGe detector along the X and Y-axis makes it position-sensitive for the gamma-ray hit. The higher degree of segmentation helps to record each event in a different segment. The coincidence technique has been employed to characterize the PSPGe detector. The detector has energy resolution (full width at half maximum) of $\approx$ 1 keV for the DC segment and $\approx$ 1.5

keV for AC segments. In Fig. 3.6(a), the guard ring is observed, represented by a black-dotted rectangular region, which accounts for the homogeneous charge collection at the electrodes. The presence of only one guard ring despite the information of the producer for two guard rings may be attributed to the electric field distribution built on 2-D structures. It may be noted that the presence of the guard ring does not prevent the trapping of the charge carriers at the open surface of the detector. Then, the surface charge there creates a "field defect" [96], [97] – an area with a specific fringe field which diverts the charge carriers toward the open surface of the detector thus eliminating them from the charge collection and pulse generation.

The pulse shape comparison scan has been performed for pulses along the 0°and 90°scans using χ^2 minimization to understand the depth of gamma-ray interaction. The χ^2 has been performed between a strip along the 0°(set-A) scan and the same strip along the 90°(set-B) scan. The pulses at different positions were selected along the depth (using the 2-D image from the PSD) and were compared to pulses in a single cut in the 90°(representing the front side of the detector) scan [13]. The formalism used for χ^2 calculation for a matrix with i pulses in one scan and j pulses in the other scan is given as follows:

$$\chi^2_{i,j} = \frac{\sum_{k=k_0}^{k_{max}} \left(Pulse_0[i,k] - Pulse_{90}[j,k]\right)^2}{k_{max} - k_0}$$

Where k represents the bin number of the pulse, which corresponds to time. k_0 represents the initial bin number where the pulses have been time aligned. k_{max} denotes the bin number with maximum pulse amplitude. $k_{max} - k_0$ corresponds to the slope of the pulse, i.e., when charge carriers are moving between the opposite electrodes. $Pulse_0$ and $Pulse_{90}$ represents pulse in the 0°and 90°scans, respectively. After comparison or χ^2 calculation, the mean of the pulses was taken for a specific χ^2 range or minimum value of χ^2. The calculation of an average pulse from the orthogonal data set comparison using χ^2 is provided in appendix C. The mean pulse was then plotted for different depth cuts. The analysis has been shown for DC0, DC4, AC16, and AC20 strips, compared along the two sets of scans. The compared pulses consisted of a matrix of $\approx$ 30000 pulses. The mean pulses plotted have been shown in Fig. 3.11. The pulse shape comparison helps to understand the interaction location of the gamma-ray inside the detector. The mean pulse calculated at various depths has different shapes. This behavior is attributed to the difference in the velocity of charge carriers moving toward the respective electrodes. From Fig. 3.11(a)-(b), it is concluded that for the DC segments, the rise-time of the pulse increases with an increase in depth. While the rise-time decreases for AC segments with the increase in depth, shown in 3.11(c)-(d). The results are consistent for the middle and edge strips. This method helps to validate the sensitivity of the scanning device to find the gamma-ray interaction depth in the PSPGe detector (for coincidence between scanner and PSPGe) using χ^2 minimization method for a set of pulses in orthogonal scanned positions.

Further, in order to understand the behavior of charge carriers along the depth generated by the incoming gamma-rays collected at opposite electrodes,

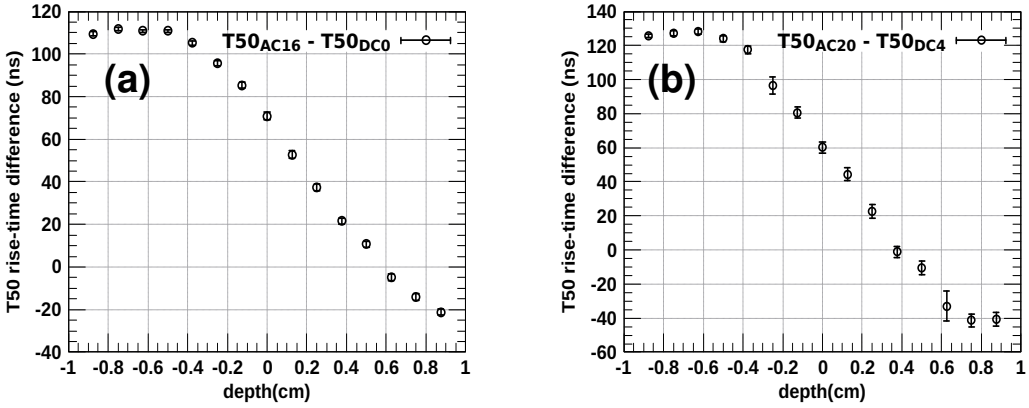

Fig. 3.12. (a) Plot of T50 rise-time difference between (a) AC16 - DC0 pair (at the detector edge) (b) AC20 - DC4 pair (middle strips) plotted as a function of depth.

the rise-time T50 has been calculated for traces obtained from the SIS3316 digitizer. The rise-time difference has been calculated between two middle strips (DC4 and AC20) and two edge strips (DC0 and AC16) by a selected segment using a 511 keV energy cut. The T50 rise-time difference has been calculated for both the strip pairs, for each of the fifteen cuts, in the 2-D image.

The T50 rise-time time difference between AC16 - DC0, and AC20 - DC4 is plotted as a function of the interaction depth in Fig. 3.12(a) and 3.12(b), respectively. The centroid of the difference in the rise-time distribution has been plotted as a function of the hit location. The Gaussian fit has been performed for each set of T50 rise-time difference values distribution. The error in each data point represents the uncertainty in the centroid after the fit. The rise-time difference between the two electrodes can help to identify the interaction location as the trace would be different for each interaction point for both types of electrode but within the position resolution of the detector, as indicated also from χ^2 analysis. The higher values of the time difference between the two electrodes describe that the interaction location is closer to the DC electrode or, vis-à-vis, far from the AC segment. The holes travel longer than the electrons to reach the AC electrode, where it deposits its energy in the processing time window of electronics for an event. This trend remains almost constant for the interaction depths at the boundaries of the detector. It becomes challenging to locate the exact point of gamma interaction in this depth region. However, in the middle/active region, the time difference shows a decreasing pattern. The decrease in time difference happens because of the relatively fast charge collection at the AC segment with an increase in depth. For AC20 - DC4, the T50 rise-time difference values vary from $\approx$ 130 to -40 ns at the extreme ends,

and for AC16 - DC0, the range is 110 to -20 ns. Hence, the difference in T50 rise-time between the two orthogonal strips helps to estimate the interaction depth independent of X and Y coordinates. The linear fit has been performed for the values of depth ranging from -0.4 to 0.7 cm. The slope of the fit was further used to obtain position difference (dX or dY) for pairs of all points, and the corresponding error was calculated through error propagation. The weighted mean has been calculated to determine position resolution as discussed in detail in appendix D.

The position resolution obtained from Fig. 3.12(a) and Fig. 3.12(b) is 1.2 $\pm$ 0.09 mm, and 1.2 $\pm$ 0.14 mm, respectively.

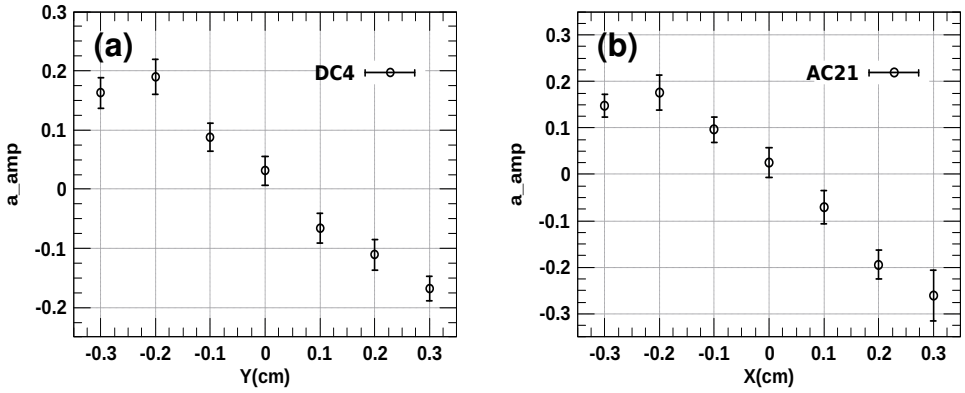

Fig. 3.13. a_amp parameter calculation for comparison of image charges in neighborhood of (a) DC4 and (b) AC21 for coincidence setup using ^{22}Na source.

In order to determine the position resolution along the X and Y-axis, the Set-B coincidence setup has been utilized. As discussed in the analysis procedure for finding the lateral position resolution, the amplitude ratio is calculated for each induced charge in the neighboring segments. The amplitude ratio between the image charges estimates how close the two interactions could be resolved. The minimum resolving would correspond to the thickness of the segment itself, as there would always be a pulse generated corresponding to an event in a specific segment. The axis of the projected 2-D image is calibrated according to the dimensions of the strip, i.e., 6 mm. For each interaction location, the amplitudes of the induced charges in the neighboring segment have been studied. In the present work, the difference in amplitude ratios has been calculated by the asymmetry parameter a_amp, which is defined as,

$$a\_amp = \frac{A1 - A3}{A1 + A3},$$

where A1 and A3 correspond to the amplitude of image charges in strip 1 and

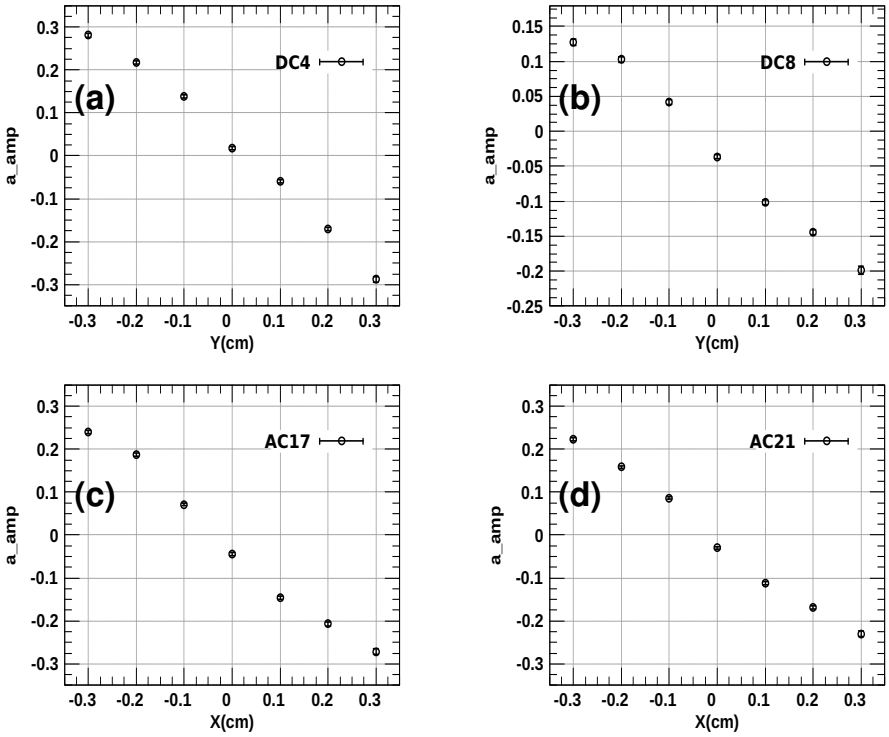

Fig. 3.14. a_amp parameter calculation for comparison of image charges in neighborhood of (a) DC4 and (b) DC8 (c) AC17 (d) AC21 using independent collimated ^{241}Am source scan.

Table 3.1: Lateral position resolution using two scan methods, i.e., coincidence scan using ^{22}Na source and ^{241}Am scan. For horizontal (DC) and vertical (AC) segment scans, the resolution has been calculated along Y and X-axis, respectively, mentioned in column 2. The neighbouring or adjacent segments (to the left and right of the scanned/hit segment) are given in column 4. The orthogonal strip, w.r.t. which the rise-time difference has been calculated, (accounting for the depth of gamma-ray interaction), is provided in column 5, and the corresponding rise-time difference values in column 6. The resolution obtained is given in column 7.

Source Scan	Scanned Axis	Scanned Strip No.	Neighbouring Strip No.	Orthogonal Strip No.	T50 rise-time difference (ns)	Position Resolution (mm)
^{241}Am	Y	DC4	DC3, DC5	AC21	140	1.0 ± 0.04
^{241}Am	Y	DC8	DC7, DC9	AC21	75	1.1 ± 0.05
^{241}Am	X	AC17	AC16, AC18	DC5	-20	1.2 ± 0.05
^{241}Am	X	AC21	AC20, AC22	DC5	5	1.1 ± 0.04
^{22}Na	Y	DC4	DC3, DC5	AC21	59.5	0.9 ± 0.25
^{22}Na	X	AC21	AC20, AC22	DC5	59.5	0.9 ± 0.27

strip 3 for interaction in strip 2 and A3<A1. In the present analysis, a_amp has been calculated for the interaction in DC4 and AC21 electrodes. For an event in the DC4 segment, the amplitude of image charges in the neighborhood of DC4 has been calculated. A3 and A5 represent the amplitudes of image charges in the DC3 and DC5 segments, respectively. Similarly, A20 and A22 represent the amplitudes of image charges in AC20 and AC22 strips, respectively, for a gamma-ray interaction in the AC21 electrode. The special note is that the a_amp has been calculated for specific depth obtained by calculating the rise-time difference between the segment and one of the orthogonal segments for both the data sets of scans (mentioned in footnote [2]). For DC4 scan, rise-time difference is calculated between AC21 and DC4 ($T50_{AC21} - T50_{DC4}$). For AC21 scan, rise-time difference is calculated between AC21 and DC5 ($T50_{AC21} - T50_{DC5}$). The values of the obtained rise-time difference have been tabulated in table 3.1 for both horizontal and vertical strip scanned data. For each of the seven cuts, a_amp is obtained using centroid from the Gaussian fit to the distribution plot and error is the error in the centroid value. The a_amp has been plotted as a function of respective axis Y (for DC4 hit segment) and X (for AC21 hit segment) as shown in Fig. 3.13(a) and 3.13(b), respectively. As we move along the axis, the amplitude of the left neighbourhood image charge decreases while the right image charge amplitude increases. Therefore, we obtain a linear decay line with a negative slope. The linear fit is performed on the data to obtain the slope. The weighted mean is calculated as explained in equations (D.1)-(D.10). The position resolution obtained has been tabulated in table 3.1.

Additionally, the analysis has been performed for position resolution calculation for collimated ^{241}Am source scan. The resolution has been studied using 60 keV photopeak selection for the scanned electrodes DC4, DC8, AC17, and

AC21. The corresponding neighbourhood image charges are stored for each hit electrode. The scan was performed for 7 data points starting from the middle of the electrode and moving collimated source in steps of 1 mm in each direction [3]. A similar analysis is performed to calculate the a_amp values from the distribution plot for each measurement position and then plotting a_amp as the function of the respective axis, shown in Fig. 3.14. The linear fit is performed to obtain the slope and further calculate position resolution as described in appendix D. The resolution measurements are tabulated in table 3.1.

3.4 Summary

From the analysis, it is inferred that the resolution along the X and Y axis for both the ^{241}Am and ^{22}Na scans, is of the order of ≈ 1 mm. The error bars differ in the two cases because of precise collimation source measurement using ^{241}Am. It has low energy gamma-ray with low attenuation depth as compared to ^{22}Na, leading to more accuracy due to surface scanning. Using ^{241}Am independent source scan, it is also concluded that the resolution is consistent along the center and edge of the detector (from table 3.1). Therefore, it is concluded that the a_amp and/or amplitude ratio between the image charges adjacent to the hit segment provides gamma-ray hit location along the X and Y-axis. The polarity of the image charges will depend upon the instantaneous electric field generated by the moving charge in the hit segment and the interaction depth.

The performance of one of the double-sided segmented planar germanium detectors has been carried out in collaboration with GSI. The aim is to employ the detector for future decay spectroscopy studies, in which the detector will be deployed as an active implantation detector. The energy and position resolution has been calculated. The resolution along the detector depth has been calculated using the difference in the rise times of charge carriers at the opposite electrodes. Further, the present analysis shows an appreciable difference in amplitudes in the neighboring strips for an event near the edges of the strip, used to calculate position resolution along the X and Y axes. This analysis provides a confidence limit of position resolution to be approximately 1 mm.

[3] The position axis in the ^{241}Am source scan shown in Fig. 3.14 is different from the axis in the coincidence setup set-B analysis shown in Fig. 3.13 as the later is calculated from the 2-D image projection while the former is from the real moving source positions.

Chapter 4

IIT Ropar Gamma Imager

The present work deals with the development of a position-sensitive gamma-ray imager/scanning device dedicated to interdisciplinary applications. The scanner is based on the principle of pulse shape comparison and positron annihilation correlation, depicted in Fig. 4.1. The two sets of measurements are performed to scan a reference detector using a Position-Sensitive Detector (PSD) and ^{22}Na source, positioned at 0°and 90°. The aim is to employ the device for scanning highly segmented tracking array detectors in order to understand interaction location, electric field distribution, defects, etc. These detectors are based on the principle of the Pulse Shape Analysis (PSA) technique for position reconstruction, implying the shape of the pulse is dependent on the point of interaction inside the detector. The work is an R&D for future scanning device development with simple configuration, employing affordable, higher gain, easy-to-handle integrated circuits. In this work, a position-sensitive detector, i.e., LYSO(Ce) monolithic scintillator crystal coupled to the matrix of 96 SiPMs, has been developed (based on comparison with other scintillators/electronics in the market, as mentioned in table 2.5). The work includes testing of the detector along with preliminary position resolution calculations, discussed in upcoming sections.

4.1 Experimental Setup and Methodology

The detector has been assembled, built, and tested in collaboration with GSI, Germany. The complete detector description, along with the experimental setup, is discussed in the following sections.

4.1.1 Detector Description and the Principle of Gamma Scanning

The new Position-Sensitive Detector (PSD) consists of a cylindrical LYSO scintillator crystal of dimensions 7 cm (diameter) x 3 mm (thickness). The scintillator has been coupled to the matrix of 96 SiPMs using RTV615 silicone

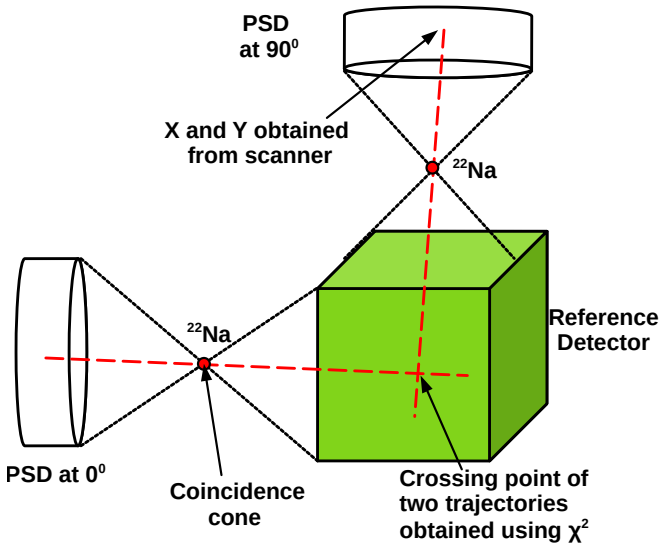

Fig. 4.1. The principle of gamma-ray scanning, i.e., pulse shape comparison performed between two data sets, for imaging of a reference detector, at 0°and 90°using positron source (^{22}Na) and a Position-Sensitive Detector (PSD). The ^{22}Na source undergoes positron decay ($e^- + e^+ - > \gamma + \gamma$), emitting two 511 keV gamma-rays in the opposite direction, used to set up the coincidence between the scanner and the reference detector.

compound-based optical glue [98] for efficient light transmission from LYSO to SiPM. The compound is mixed with a curing agent (provided together by the company) in a ratio of 10:1 by weight. The other benefits include good shock-absorbing power and insulation properties due to less viscosity.

Further, c-type 3 mm x 3 mm SiPMs (serial No. 30020) have been employed, manufactured by Sensl [99]. The array has been constructed on a PCB with a back-end containing an RC circuit for pulse readout, i.e., reading electrical pulse produced after electron-hole pair generated by scintillation light falling on the SiPM/p-n junction. Fig. 4.2 shows the scintillator coupled to the SiPM front-end and back-end of the SiPM matrix. The front SiPM matrix panel is shown in Fig. 4.3(a) consisting of 96 SiPMs. The back panel contains CLP connectors (CLP 125-02-L) 4.3(b). The details of this connector are provided in Ref. [100]. Additionally, the board has been coupled to another PCB containing FTSH connectors which have been inserted inside the CLP connector (in the same configuration) on the front panel of PCB 4.3(c), while the back side contains a connection for flat cables 4.3(d). The scintillator has been covered by thin Aluminized Mylar foil for increased reflectivity. Lastly, the whole assembly has been enclosed in a tight-packed black box. For further blocking the outside light, black tape (made of polyesters that can sustain Temperatures from -40

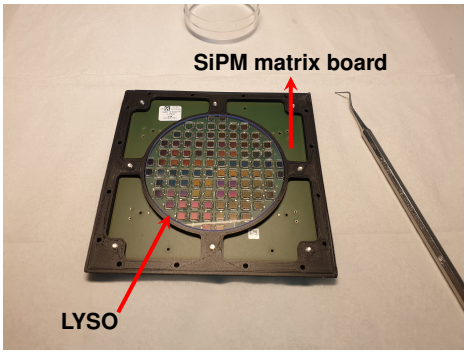

Fig. 4.2. Image of thin cylindrical LYSO scintillator coupled with SiPM board (green PCB). An outer black body is used to completely secure the scintillator crystal with the SiPM board.

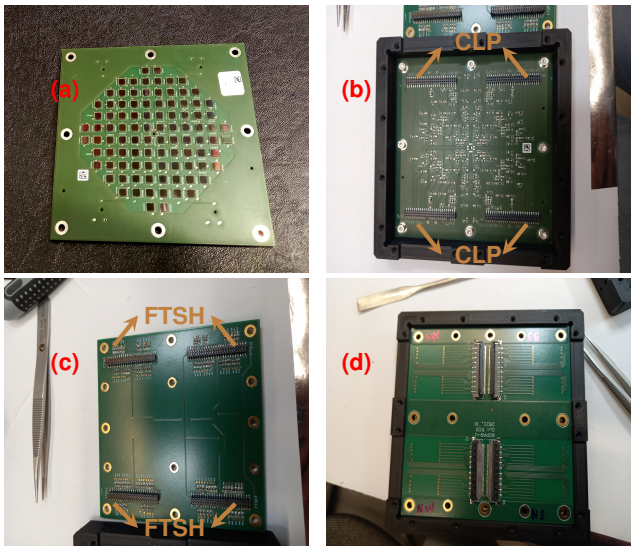

Fig. 4.3. Different development stages of various PCBs carried out at GSI (a) SiPM matrix front panel, (b) SiPM matrix back panel, (c) PCB front panel containing male FTSH connectors that are inserted into CLP connectors on the SiPM PCB back side, (d) FTSH connector PCB back panel having X-connectors for flat cable connection.

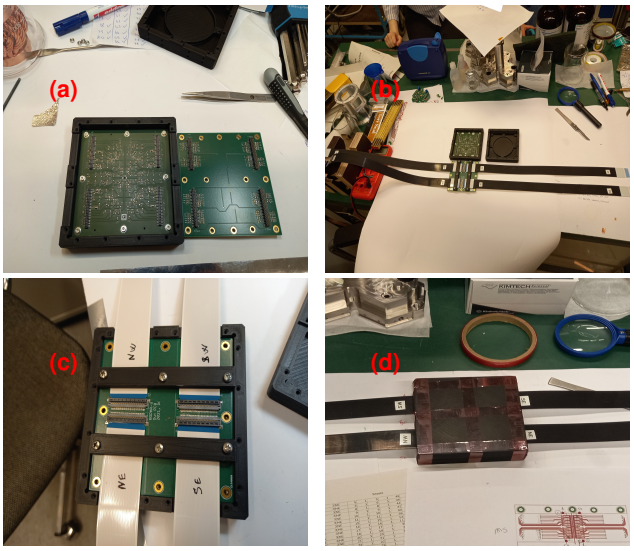

Fig. 4.4. Different stages of development of various PCBs (a) SiPM matrix front panel already coupled to scintillator and enclosed in the black box from that side (b) Flat cables connected to FTSH PCB back panel, (c) SiPM matrix back panel connected to FTSH board front panel, (d) full assembly covered with the black box.

to 121°C) has been wrapped along the complete detector geometry. For ease of reading/understanding, the SiPM matrix is contemplated as a combination of four quadrants, defined as North-East (NE), South-East (SE), South-West (SW), North-West (NW), being marked on the top of the detector front surface.

All the developmental stages of the detector are shown in Fig. 4.3, including the SiPM matrix array to the second PCB connection to the flat cable on the final PCB board. Additionally, full mapping has been defined in stages from quadrant number → SiPM number → CLP pin number → FTSH pin number → X-connector → pin number → flat cable channel number.

For readout from flat cable, the distributor board has been developed consisting of Lemo connectors as well as flat cable connectors for output depending upon the type of electronics to be used with the setup. This has also been further mapped with the known flat cable channels. The PCB with Lemo output connection has been used in the present work for signal readout, denoted in Fig. 4.5. The final detector assembly is shown in Fig. 4.6.

The output signal has been studied using a scope, as shown in Fig. 4.7 without source. The detector was biased at -30 V. Due to the self-activity of LYSO, the background looks prominent in the detector. At -20 mV pulse height, the rise time and pulse width are approximately 50 ns and 400 ns, respectively.

The biasing to the detector depends upon the SiPM configuration used.

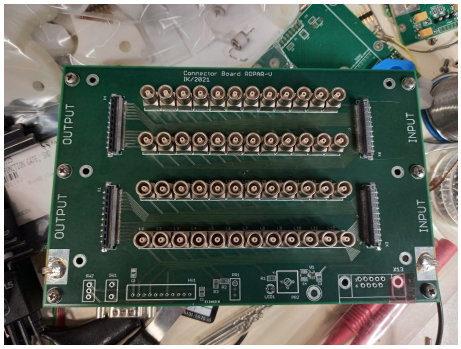

Fig. 4.5. PCB with Lemo connectors. The detector output signal via flat cable is connected here. Each PCB has 48 channels, and 2 such cards were used in the setup.

Fig. 4.6. POS2 detector assembly (a) front view (b) side view (c) top view of the detector.

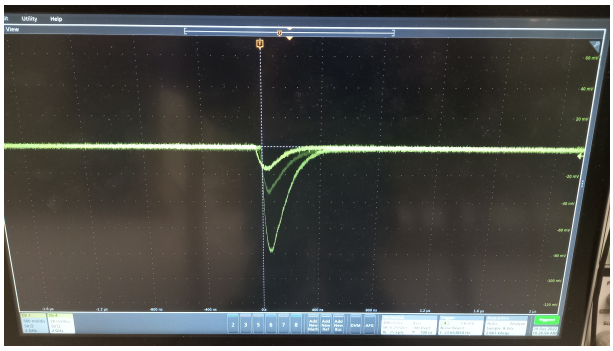

Fig. 4.7. An image of a background signal in POS2 captured directly from the oscilloscope.

In the present development, output has been taken from the p-side (Anode), implying negative biasing to the detector for reverse biasing condition, and standard output has been used for pulse readout, as described in section 1.1.4. The detector is operated in the avalanche breakdown region to compensate for the temperature sensitivity of the SiPMs as in the present development, and there isn't a temperature sensor, which will be taken care of in the future). Moreover, the employed readout electronics do not have an amplifying/booster circuitry. Therefore, the detector was operated at -30 V using Rhode & Schwarz voltage unit.

4.2 Experimental Setup

The preliminary detector characterization/testing has been carried out through different sets of measurements, listed in the following points,

1. **Test 1**: In the first step, the VME electronics setup has been used with 24 detector channels, and characterization has been performed using ^{22}Na radioactive source, with an activity $\approx$ 84 kBq, to understand the detector response towards incoming gamma-rays.

2. **Test 2**: The second test was performed using a coincidence setup between the GSI scanner and the new PSD.

4.2.1 Test 1

The different sets of measurements were performed with the source at various corners of the detector surface. Because of limited Analog electronics, 24 detector channels were employed, i.e., one quadrant (SE). It has SiPMs numbered between 1 to 24. The source was placed at the top of the detector surface (attached with tape). For the 24 channels, the Lemo output of the PCB (Fig. 4.5) was fed to the 16-channel Fast Amplifier (FA), and after zero offset correction in

FA, the output was connected to VME-based charge to digital convertor (QDC). The trigger of the QDC was chosen as the OR of all channels. To obtain this, the second output signal from FA was fed to three 8-channel Constant Fraction Discriminators (CFD). The common OR output of each CFD was connected to a coincidence module, in which further the OR of the 3 channels was performed. The QDC was read through GSI Multi Branching System (MBS). The anti-coincidence was performed between OR output from the previous coincidence unit and the DAQ deadtime to obtain the accepted trigger. The accepted trigger further triggers the MBS through the TRIVA7 module. Similar electronics schematics have also been discussed in Ref. [16] for the MBS system. This trigger was fed to the QDC module. In order to read the same event from the FA output and the accepted trigger, the FA output was delayed using a delay module, before feeding the signal to the QDC. QDC gate window was ≈ 1.5 μs. The complete electronic schematic is shown in Fig. 4.8.

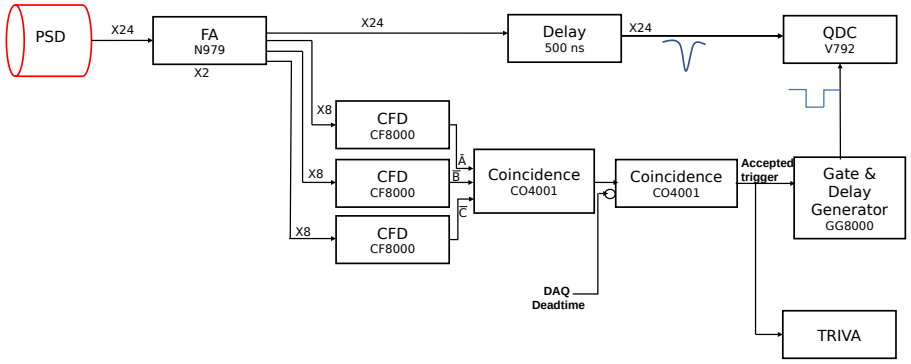

Fig. 4.8. Electronics schematics used for the characterization of PSD - Test 1.

The raw detector signal had a pulse height of the order of 20-30 mV for 511 keV gamma-rays, for the detector biased at -27 V. The rise time of the pulse was $\approx$ 50 ns, and pulse width $\approx$ 400 ns.

After the full electronics setup, the measurements were performed for the source at the center of the detector (set-A), and changing its position to the edge/corner in the same column (set-B). The measurements were performed for 10 minutes for both sets. Before this measurement, background measurement was performed to perform gain matching of each of the channels with good statistics. The typical background data rate was $\approx$ 500 Hz. The set-A measurement had accepted trigger rate $\approx$ 2900 Hz, while for set-B, it was $\approx$ 1400 Hz. Fig. 4.9 (a) depicts the SiPM matrix with channels being numbered. The corresponding QDC mapped channels to SiPMs for the SE quadrant are represented in Fig. 4.9 (b). The source position for the quadrant SE for set-A and set-B has been marked with a star in Fig. 4.9 (b). The results obtained are

discussed in the section 4.3.

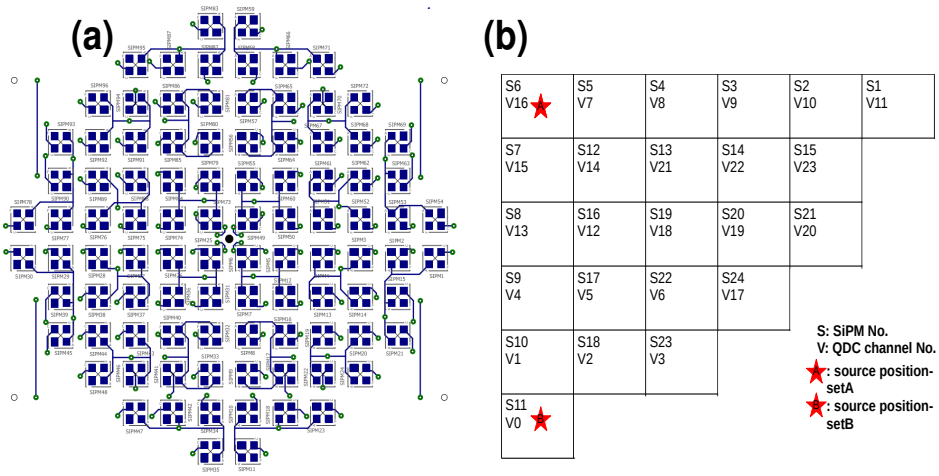

Fig. 4.9. (a) Mapping of SiPM matrix, (b) SE quadrant mapping with QDC channels - Test 1. The two source positions are represented by a star.

4.2.2 Test 2

In test-2, the coincidence was set up between the GSI scanner (detailed in section 3.1.2) and the PSD. The coincidence detector setup is shown in Fig. 4.10. The distance between the ^{22}Na source and the PSD was $\approx$ 8.2 cm. The distance was optimized for full solid angle coverage around the PSD, by checking 2-D images online using GO4 software. The electronics arrangement for the GSI scanner was the same as discussed in the section 3.1.2 and Fig. 3.4, i.e., VME based 32 channel QDC was used. For PSD, the Lemo output was connected to GSI's in-house developed new FPGA-based digitizer, TAMEX.

A GSI in-house developed FPGA-based advanced readout TDC (Time to Digital Convertor) module - TAMEX has been employed. The primary motivation for employing this digital electronics, over conventional readout TDCs is to attain a simpler and cost-effective readout method, with improved timing measurements. FPGA is an IC that consists of logic blocks that can be programmed (with descriptive language) at any time according to operational needs and don't require any change in the circuit. Hence, FPGA-based electronic chips are flexible in terms of working. FPGA-based TDCs are developed using delay lines as discussed in Ref. [101] [102]. It depicts a compromise between accuracy and resolution. In order to optimize the two, care in circuit designing is necessary.

The TAMEX cards provide timing with RMS precision of 15 ps [101]. It has 32 channel readout and deadtime $\approx$ 20 μs. It can measure the timing of

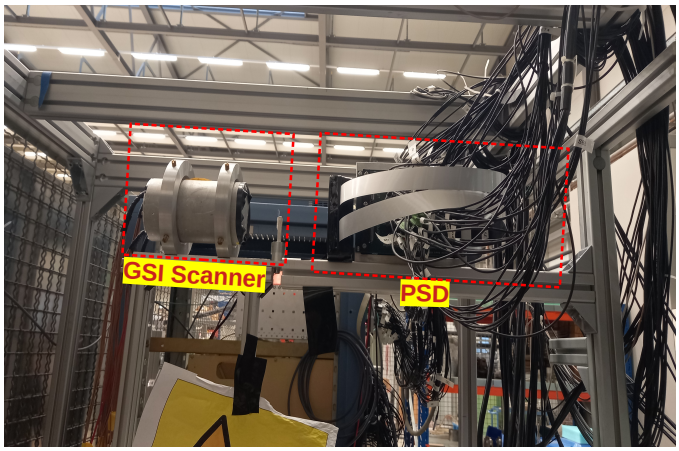

Fig. 4.10. Coincidence setup between GSI scanner (left) consisting of LYSO scintillator detector + ^{22}Na source and PSD (right).

logic signals by using a timestamping method. One can apply the logic outputs of standard NIM/VME etc., discriminators (Leading edge or Constant fraction discriminator) or use custom-made frontend discriminators plugged directly into the Tamex card. The newest analog frontend discriminator development of GSI is the twin peaks card. Twinpeaks can provide signals for time and energy measurement by using two independent branches. Inside the card, the input is split into two branches (a) fast branch - to measure the leading edge time of the input signal, (b) slow branch - for energy measurement. The fast branch provides log amplification for timing, and the slow branch has linear amplification for energy measurement, which is based on the time over threshold principle. In both branches, both signal edges can be discriminated, and the TAMEX TDC can measure both leading and trailing edge time. The time difference in the slow branch is a direct measure of the signal energy. For the fast branch, the output is proportional to the logarithm of the input signal, as shown in equation (4.1). For slow, they are directly proportional, as represented through equation (4.2).

$$V_{OF} \propto log(V_{in}) \tag{4.1}$$

$$V_{OS} \propto V_{in} \tag{4.2}$$

In the above equation, V_{in} represents the input signal to the card/ detector output. V_{OF} and V_{OS} denote fast and slow output signals, respectively.

The difference between the two branches is the intermediate processing electronics/amplifiers. The pulse is measured from the leading edge to the trailing edge (which is measured above the threshold set). Therefore, the difference in leading and trailing edges leads to different amplitudes and, therefore, proportional to the amplitude or, say, energy deposited by the particle. The comparator thresholds can be set to both positive and negative amplitude values.

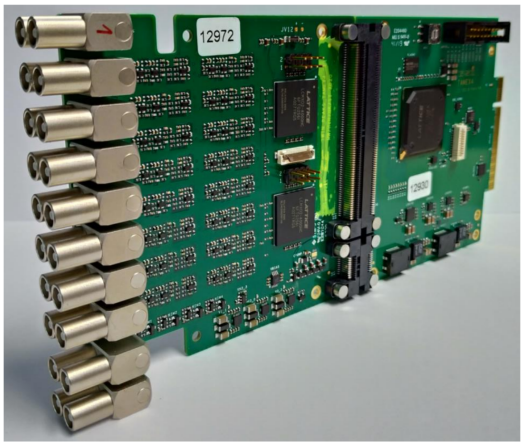

Fig. 4.11. Tamex Electronics card.

The time over the threshold (TOT) (or pulse width, i.e., lead minus trail) is calculated for the amplitude of the signal. For timing measurements, lead is considered. It has two timings, i.e., coarse and fine time. Coarse time is 5 microseconds, and fine time runs between 0 to 5 microseconds. The signal in TDC is recorded after 1.2 μs, i.e., the long pulse width can be achieved. For fast output signal, the discriminator threshold values have to be adjusted, while for slow, it is preset to an optimal value. The selection of a specific threshold for the fast branch is necessary as there is a predefined minimum value, below which pulses are not registered in the electronicsThe time resolution obtained is $\approx$ 270 ps using a Lanthanum bromide scintillator detector with the twin peak TAMEX card. For 96 channel readout, six TAMEX cards have been employed, each consisting of 32 input channels, coupled to front-end twin peak readout with 16 channels shown in Fig. 4.11.

The electronics schematic for this setup is shown in Fig. 4.12. The scanner 32 outputs are fed to FA, followed by a delay unit to take care of the event reading with the trigger. Later, the output was fed to QDC. The first anode output was used for timing, being connected to Timing Filter Amplifier (TFA), followed by CFD to obtain a logic pulse. For the TAMEX crate, the trigger selection was performed using a unit called exploder [103]. The VME MBS and the TAMEX MBS systems use different hardware with different dead times. By connecting the two trigger modules, TRIVA (VME) and TRIXOR (TAMEX), with the GSI trigger bus, they run in common trigger mode. One of the systems has to be configured as the master trigger (TRIVA in the present setup). In the combined DAQ, the deadtime locking was performed in the master trigger crate VULOM, and the accepted trigger was sent directly to the TAMEX cards. The DAQ trigger is the AND of the TAMEX OR and the scanner CFD. It was connected as a free trigger to the master trigger crate (VME). The accepted trigger was the anticoincidence of the free trigger with the DAQ deadtime. The accepted

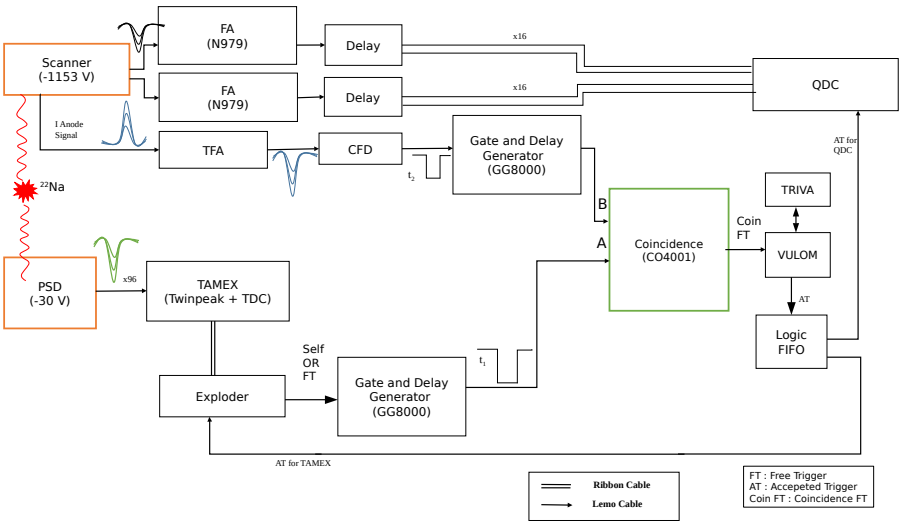

Fig. 4.12. Electronics schematic for Test 2.

					S83 T0	S59 T1					
			S95 T2	S87 T3	S82 T4	S58 T5	S66 T6	S71 T7			
		S96 T8	S94 T9	S86 T10	S81 T11	S57 T12	S65 T13	S70 T14	S72 T15		
	S93 T16	S92 T17	S91 T18	S85 T19	S80 T20	S56 T21	S64 T22	S67 T23	S68 T24	S69 T25	
	S90 T26	S89 T27	S88 T28	S84 T29	S79 T30	S55 T31	S60 T32	S61 T33	S62 T34	S63 T35	
S78 T36	S77 T37	S76 T38	S75 T39	S74 T40	S73 T41	S49 T42	S50 T43	S51 T44	S52 T45	S53 T46	S54 T47
S30 T48	S29 T49	S28 T50	S27 T51	S26 T52	S25 T53	S6 T54	S5 T55	S4 T56	S3 T57	S2 T58	S1 T59
	S39 T60	S38 T61	S37 T62	S36 T63	S31 T64	S7 T65	S12 T66	S13 T67	S14 T68	S15 T69	
	S45 T70	S44 T71	S43 T72	S40 T73	S32 T74	S8 T75	S16 T76	S19 T77	S20 T78	S21 T79	
		S48 T80	S46 T81	S41 T82	S33 T83	S9 T84	S17 T85	S22 T86	S24 T87		
			S47 T88	S42 T89	S34 T90	S10 T91	S18 T92	S23 T93			
					S35 T94	S11 T95					

S : SiPM No.
T : Tamex channel No.

Fig. 4.13. Mapping of SiPM matrix and the corresponding TAMEX card channel numbers.

trigger was used in the VME for the QDC gate generation and for TAMEX data validation in TAMEX. It also triggered the VME and TAMEX data readout. Before taking the data, the online fine time calibration was performed using an internal pulser in the TAMEX (by communicating through the MBS terminal using the command line). The idea is to bring all the channels to the same binning, i.e., the procedure for uniform binning. Otherwise, the non-uniform binning may lead to unwanted spikes in the TOT spectrum. Further, important settings were performed in the setup file for TAMEX, i.e., threshold settings for each channel, selecting trigger as OR of all the channels. The different sets of coincidence measurements were performed by changing thresholds in the tamex. In the present work, the results have been presented for the optimized threshold settings. The mapping between PCB Lemo channels of PSD and the TAMEX channels was performed, as shown in Fig. 4.13. The PSD bias voltage was kept -30 V. The coincidence data rate was $\approx$ 100 Hz.

4.3 Analysis and results

The analysis has been performed for both Test 1 and Test 2 measurements independently. The key procedure of analysis is given below:

- Performing gain matching of all the channels using background measurement for both tests.
- Neighboring amplitude spectra have been constructed after gating on one of the references SiPM channels.
- For Test2, a 2-D image from the scanner has been reconstructed for the coincidence data.
- SiPM gated amplitude spectrum has been studied using slow TOT. For slow TOT spectrum, refer to the appendix E.
- The 2-D image is reconstructed for one of the selected SiPM channels by gating on the TOT. Further, Sub-dividing the projected image on to X-axis.

4.3.1 Test 1

The background data of an overnight run for approximately 12 hours have been used to gain match the channels. The gain matching procedure is important to produce the sum spectrum later, which provides total charge distribution in the detector. The channels before and after gain matching are shown in Fig. 4.14 (a)-(b). The matching is performed by subtracting the pedestal value (noise in the QDC channel produced due to bias and is independent of the signal) is subtracted. Later the gain of the channels is set w.r.t one of the channels.

Further, the comparison of results between background, setA, and setB measurements is shown in Fig. 4.15 (a), (b), and (c), respectively. The plot is

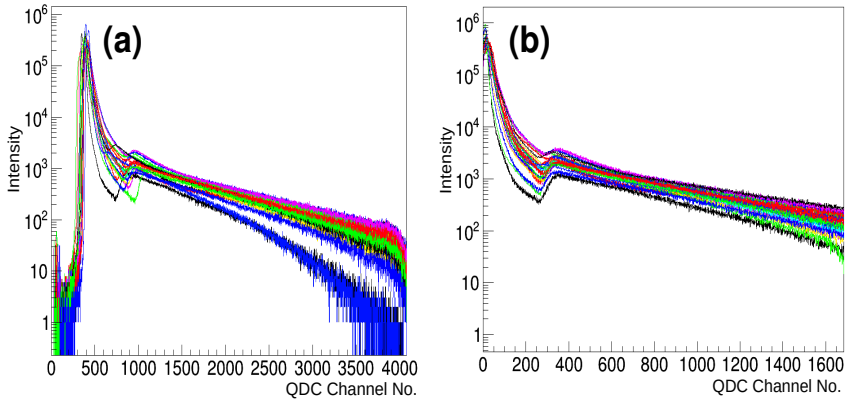

Fig. 4.14. QDC channels (a) before and (b) after gain matching procedure.

obtained for Position_X along the X-axis, Position_Y along the Y-axis for the PSD SiPM positions, and channel amplitude is shown along the Z-axis. From Fig. 4.15, it is observed that the background has a uniform charge distribution. Further, setA has higher amplitude for Position_X, and Position_Y equals -120, while for setB measurement, more charge region is for Position_X equals -120 and Position_Y equals -1380, i.e., when the source was moved directly to the opposite corner.

One of the reference channels has been selected with the condition that the amplitude is greater than 250 (to take into account only higher energy events) as well as the same channel has fired with the maximum amplitude. With this selection, amplitude in the neighboring channels has been investigated with the threshold condition of above 50 (to be fairly above the noise). The normalized amplitudes have been calculated between the reference channel (A[reference]) and the neighboring channels (Amplitude[i]), denoted by the ratio Amplitude[i]/A[reference].

The 1D plot obtained for the normalized amplitudes has been plotted and shown in Fig. 4.16 for setA measurements. The reference channel is S6, and the first neighbors are S5 and S7 (red and blue curves, respectively); the first diagonal is S12 (magenta colored), second neighbors are S4 and S8 (shown as black and green, respectively). It is evident that the amplitude in the neighboring segments is sensitive to the hit location. From this analysis, it is observed that the ratio in amplitudes for the first and second neighbors is of the order of ≈ 3.5. Hence, a similar analysis can be extended to further determine the gamma-ray interaction inside a single SiPM and hence, the resolution of the detector.

The multiplicity for the PSD with the coincidence data for Test 2 measurements is shown in Fig. 4.17. It denotes the number of SiPMs firing in each event. From the plot, it is observed that most of the time only one SiPM fired,

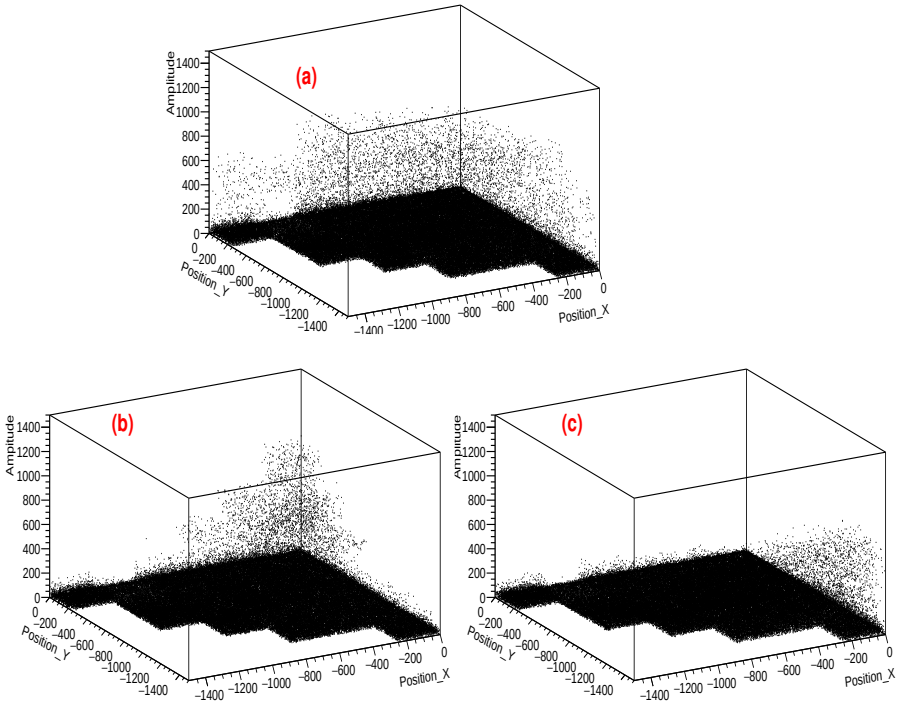

Fig. 4.15. 3-D plot for Test 1 measurements with (a) background, (b) setA, (c) setB data. The slow TOT amplitude has been plotted as a function of Position_X and Position_Y of the SiPM matrix.

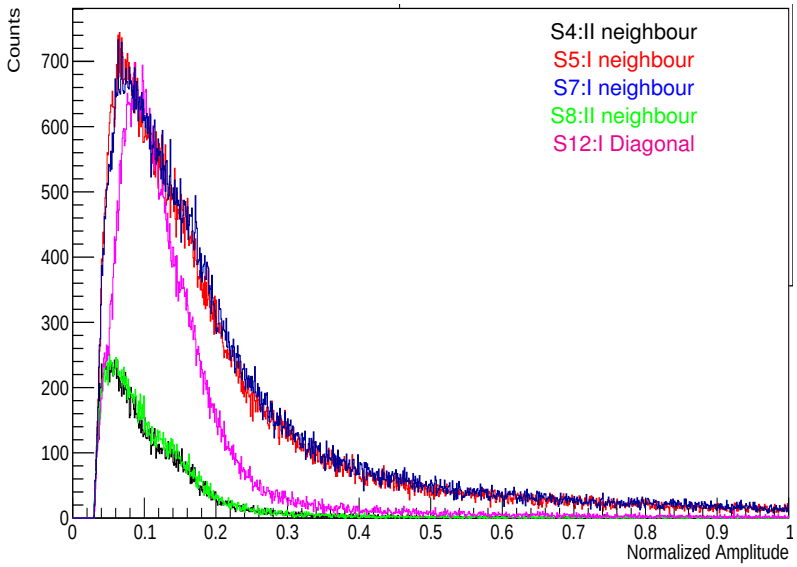

Fig. 4.16. 1D plot obtained for normalized amplitudes of the neighboring channels for reference selection channel S6 for setA measurement (Test 1).

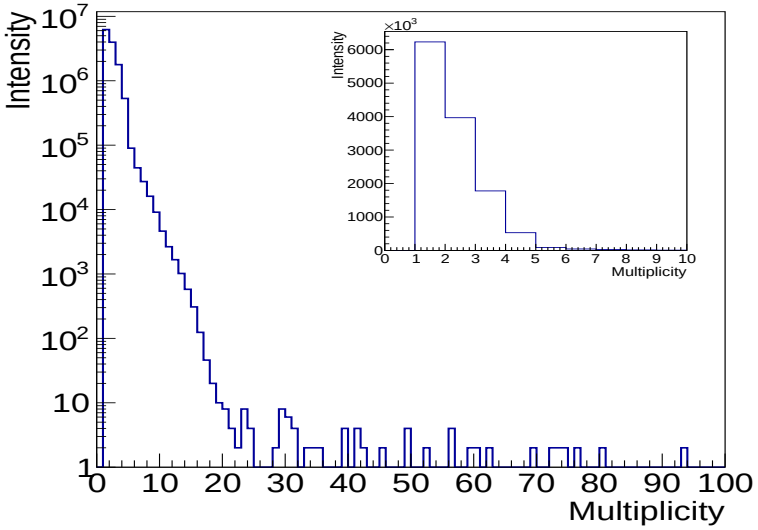

Fig. 4.17. PSD multiplicity spectrum obtained for the coincidence setup. The inset shows a linear scale of the same spectrum zoomed to events up to multiplicity 10.

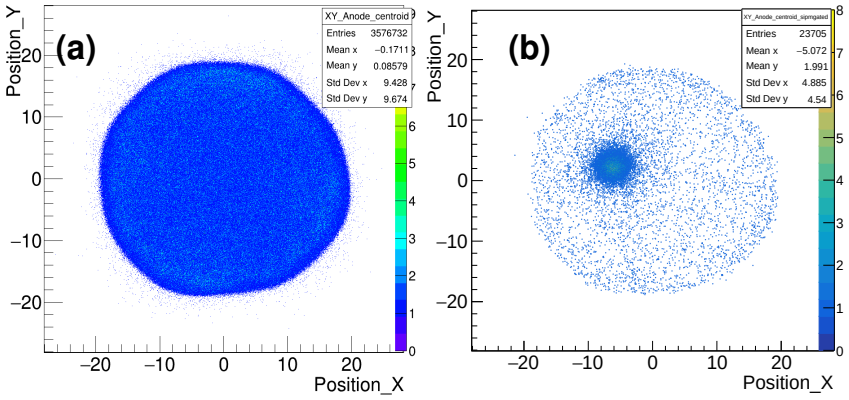

Fig. 4.18. (a) 2-D coincidence image obtained from the scanner, and (b) SiPM channel S26 gated 2-D spectrum.

i.e., multiplicity equals 1. It may be attributed to the threshold selection in TAMEX and the small input signal amplitudes. The ratio of multiplicity 2 events to multiplicity 1 events (Intensity(M2)/Intensity(M1)) is $\approx 65\%$, i.e., the more events are obtained with one channel firing the most.

The 2-D image for the coincidence setup has been reconstructed from the GSI scanner using the centroid fitting approach. It has been attained through charge collected at X and Y anodes in PSD using QDC. The 2-D images obtained from this analysis as shown in Fig. 4.18 (a). The image shows uniform distribution of the charge for the coincidence data. This measurement has been obtained after many threshold settings to get some optimized charge distribution. Further, the 2-D image has been reconstructed from the scanner for one of the SiPM firing, i.e., S26. A threshold of $400\text{x}10^3$ has been applied on the TOT spectrum to investigate the amplitude of neighboring channels being fired. The 2-D image is projected onto X-axis, and after fitting, the centroid (C) and standard deviation (σ) have been used to sub-divide the segment from C-σ to C+σ. It is calibrated using known dimensions of the SiPM, i.e., 3 mm. The asymmetry parameter has been calculated and defined as:

$$asym\_param = \frac{A1 - A3}{A1 + A3}, \tag{4.3}$$

where A1 and A3 represent slow TOT values in the neighborhood of the hit channel.

The parameter has been calculated for different cuts along the X-axis, and the plot is represented by Fig. 4.19 (a). The reference channel chosen has been S26. The neighboring channels along X are S25 and S27. A similar analysis has been performed for asymmetry parameter calculation along Y-axis, shown in Fig. 4.19 (b). The reference channel is S31, and the neighboring channels are S25 and S32 along Y-axis. The linear fit has been performed to the data to

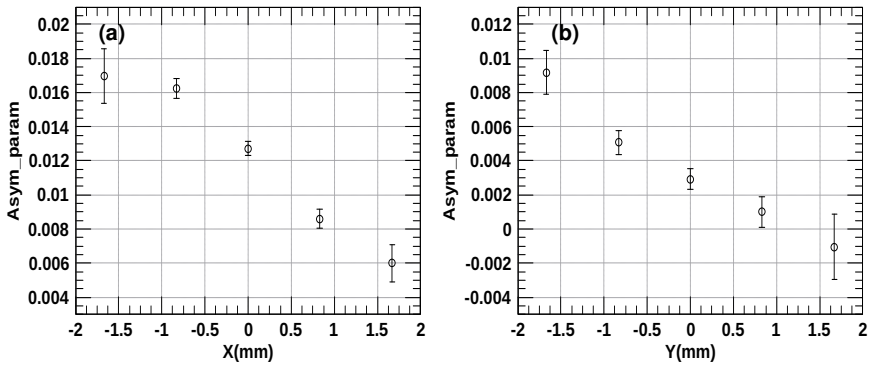

Fig. 4.19. Asymmetry parameter calculation for different interaction positions along (a) X (b) Y-axis.

calculate the position resolution using weighted mean calculation, as described in appendix D. For X-axis, the resolution is of the order of $\approx 0.9 \pm 0.3$ mm, and for Y-axis, it is $\approx 0.8 \pm 0.2$ mm.

On the basis of the present findings, it can be inferred that the difference in amplitudes obtained in the neighboring segments is sensitive to position determination of the order of 1 mm. The events with multiplicity 1 need to be further investigated by employing an amplifier before feeding the detector signal to the TAMEX front card.

4.4 Summary

The new gamma-ray imager has been developed in collaboration with GSI using advanced readout technology, being affordable, miniature, compact, and with a better spectral response. It consists of Cerium doped LYSO scintillator crystal coupled to the matrix of 96 SiPMs. The preliminary detector testing has been performed using independent source measurement as well as imaging with an existing GSI scanner. The chapter includes detector details, a description of the electronics setup, measurements performed, and finally, the results obtained. The analysis has been performed by investigating the amplitude difference in the neighborhood of the hit channel, checked qualitatively for both measurements. Further, the asymmetry parameter has been calculated between the amplitudes of the neighboring channels as a function of X/Y, providing a resolution of the order of 1 mm. The results are promising for further detector response studies using various position reconstruction algorithms.

Chapter 5

Summary and Future Prospects

In summary, this thesis deals with the characterization and performance test of a scintillator and a segmented high-purity germanium detectors (HPGe) employing gamma scanning devices / imager at GSI Germany. In recent years, the field of gamma-spectroscopy with imaging capabilities has progressed significantly with the advancements in crystal production, very good timing and energy resolution, and miniaturization of pulse processing electronics. The development of new highly segmented detectors has opened new boundaries for gamma-spectroscopy studies with gamma-ray tracking, built with an aim to obtain increased efficiency, high solid angle coverage, along with the Doppler shift correction owing to better energy resolution. It has been narrated that complex geometry detectors require full 3-D characterization to store a database of pluses for known gamma interaction locations, referred to as the pulse shape analysis (PSA) technique, to determine the gamma-ray interaction position inside the detector. Aiming to achieve a rich data set for gamma interaction points, dedicated scanning systems have been developed contributing to the scanning of such detector arrays to understand the detector response, electric field distribution, defects, etc. This thesis reports on the characterization of a segmented planar Ge detector and R&D for a new and/or advanced gamma imager for IIT Ropar.

In the first set of investigations, the response of the Position-Sensitive Planar Germanium (PSPGe) detector has been studied using the coincidence technique, along with independent collimated source measurement. The analysis is performed to select an electrode of interest (middle and edge) in horizontal and vertical directions using an energy gate. For resolution along the Z-axis (depth of the PSPGe detector), the 2-D image obtained using the coincidence setup has been used to divide the axis in depth as it is not segmented. The χ^2 comparison has been performed between the 0°and 90°coincidence scan using scanning setup for different depths. The mean pulse obtained for the different

depths provide information on the mobility of charge carriers moving toward the respective electrodes. Further, the interaction depth of the PSPGe detector has been studied using the rise-time difference between the two opposite surfaces as a function of depth for middle and side strips. The appreciable rise-time difference has been obtained at various depth locations with position resolution of the order of $\approx$ 1.3 mm, consistent at the borders of the detector. In order to achieve position resolution better than 6 mm (the size of the segment itself), the strip has also been divided using the 2-D image projection cut along both X and Y directions from the coincidence ^{22}Na source scan data. The position resolution along the horizontal and vertical directions is measured using the difference in amplitudes of the image charges in the neighborhood of the selected hit segment. The measured amplitude difference is considered to account for the gamma hit location. The analysis for the front crystal scan (providing X and Y resolution) has also been performed using collimated ^{241}Am. The obtained position resolution along X and Y axis using both scans is around 1.1 mm. The detector has an energy resolution of $\approx$ 1 keV for the DC segment and $\approx$ 1.5 keV for AC segments. As an extension of this work, the plan is to study PSA using simulations.

In the second set of investigations, a new gamma-ray imager/Position-Sensitive Detector (PSD) setup has been developed for IIT Ropar in collaboration with GSI, Germany. The gamma imager is based on the principle of positron annihilation correlation and pulse shape comparison. The first phase of the detector testing was performed at GSI using different sets of measurements. The experiment has been performed with an independent source measurement and a coincidence setup between the GSI scanner and the new PSD. The independent analysis has been performed for two sets of measurements by selecting a reference channel with a threshold accounting for photopeak events followed by the investigation of amplitudes in the adjacent channels. The analysis shows that the amplitudes are sensitive in the adjacent channels, checked qualitatively. For coincidence source measurement, a reference channel is selected to reproduce a 2-D image and sub-dividing the projected image, calibrated using known SiPM dimensions. The asymmetry parameter has been calculated between the amplitudes of the adjacent channels as a function of X/Y. The resolution obtained along X and Y is typically of the order of $\approx$ 1 mm. The preliminary results obtained are promising to further investigate the resolution at the edges. The algorithm is in progress to construct a 2-D image from the new PSD. It has been difficult in the present experimental data due to the less intensity of multiplicity greater than 1 event obtained with the current threshold settings. The SiPMs have been found to be extremely sensitive to the gamma-ray hit, source position, and amplitudes of the adjacent channels. This is further to be investigated for future work with different threshold settings and employing an amplifier for the detector output signal because of the small amplitude signal from the detector.

5.1 Future Prospects

- The extension of this work involves the advancement of pulse shape analysis (PSA) using highly optimized simulations for PSPGe scanning. In order to get a better approximation, we plan to implement Artificial Intelligence (AI) to predict pulse shapes and compare them with the present database of experimentally measured pulses. In addition to the performance test presented in this thesis, the detector has been used in one of the test beam experiments using the fragment separator (FRS) facility at GSI Germany in mid of 2022. The experiment was performed with ^{197}Au (projectile) + ^{63}Cu (fixed target). In this experiment, the ^{184}Pt fragments produced due to fragmentation with an energy of 200MeV/U have been guided through the separator and stopped at the PSPGe detector. The primary aim was to test the detector's performance towards an incoming heavy-ion beam, its position determination, and the simultaneous detection of low-energy gamma-rays. The analysis of the experiment described above needs to be extended and concluded to understand the performance of the system.

- For new gamma imager/scanner development, the R&D has been carried out using advanced readout electronics. The present detector characterization suggests the sensitivity of the detector towards the threshold selection in the new TAMEX digitizer. The next step is to experimentally check the detector threshold values and test the signal using an amplifier before feeding it into the digitizer. Further, the future development step in the detector involves the inclusion of a temperature sensor for SiPM for real-time monitoring of the temperature. The detector resolution needs to be tested at the boundaries. Additionally, work on Geant4 simulations is under progress to compare the experimental detector performance with the simulations and further use to develop a position reconstruction algorithm using advanced machine learning algorithms.

APPENDIX A

Signal/Pulse formation in semiconductor detectors

A.1 Current induced by moving charge

The radiation falling on the detector produces charge carriers, i.e., electron-hole pairs in the depleted region in the semiconductor detector. These charge carriers move under the influence of the applied field. The movement or transportation of these charge carriers induces a current signal on the electrode. The effect due to opposite charges is summed. This method calculates charge transport and current induced in a semiconductor detector. Shockley-Ramo theorem is used to find the instantaneous current induced due to the motion of charge carriers [29]. It states that the current induced at an electrode depends upon the instantaneous electric field lines at that point and time in the detector. The instantaneous induced current is given by:

$$i(t) = q\frac{E(x)_{v_d}}{V(x)}, \tag{A.1}$$

where, q = charge of the moving particle, E(x) = applied electric field at any instant of position x, v_d = drift velocity of the particle, V(x) = electric potential of the electrode. For two infinite parallel plates separated by a distance d, such that they maintain a uniform electric field, the then induced current is given by,

$$i(t) = q\frac{v_d}{d} \tag{A.2}$$

Further, the weighting potential is defined as the measure of coupling between the moving charge and the electrode where a charge is moving. It is calculated by solving Poisson's equation considering the electrode of interest is at unit potential, and the rest are at zero volts. To derive the induced charge in a pixelated detector, work has been performed in the literature [104]. In this work, they have considered all electrodes to be grounded and one electrode

connected to the potential, called the sensing electrode. Due to the potential at a say infinitesimal electrode, it will induce a charge on the sensing electrode. It implies that the moving charge will also induce a charge on the sensing electrode, given by the reciprocity theorem, i.e.,

$$\sum_i \frac{Q_i}{V_i} = \sum_i \frac{Q_i^{'}}{V_i^{'}} \tag{A.3}$$

In this case for two electrodes, if V_s induces charge Q_m on infinitesimal electrode, and V_m induces Q_s on sensing electrode, then from the equation (A.3),

$$Q_s V_s = Q_m V_m \tag{A.4}$$

The corresponding current induced on the sensing electrode is:

$$i_s(t) = \frac{dQ_s}{dt} \tag{A.5}$$

This represents current due to the charge moving along the dx direction with drift velocity (v_d=$\frac{dx}{dt}$). Therefore,

$$i_s(t) = \frac{d\frac{Q_m V_m}{V_s}}{dt} = \frac{Q_m}{dx}\frac{V_m}{V_s}\frac{dx}{dt} \tag{A.6}$$

Using weighting potential for normalized field (with weighting electric field, $E_w = -\Delta(V_m V_s)$), the equation (A.6) can be written as,

$$i_s = -Q_m E_w v_d \tag{A.7}$$

The induced charge at the sensing electrode is,

$$\begin{aligned} Q_s &= \int i_s dt \\ &= -Q \int_{x_1}^{x_2} E_w dx \\ &= Q[V_w(x_1) - V_w(x_2)] \end{aligned} \tag{A.8}$$

This implies the induced charge depends upon the potential difference for the charge moving between points x_1 and x_2, as also described in Ref. [92].

A.2 Charge carrier drift in the planar HPGe

After the gamma-ray deposits or gets absorbed by the semiconductor detector, followed by any of the processes, i.e. PEE, CS, and PP, it emits/generates e^- - holes in the depletion region, which drifts in the presence of electric field towards the opposite electrodes, as shown in Fig. A.1. Therefore, the drift of the charge

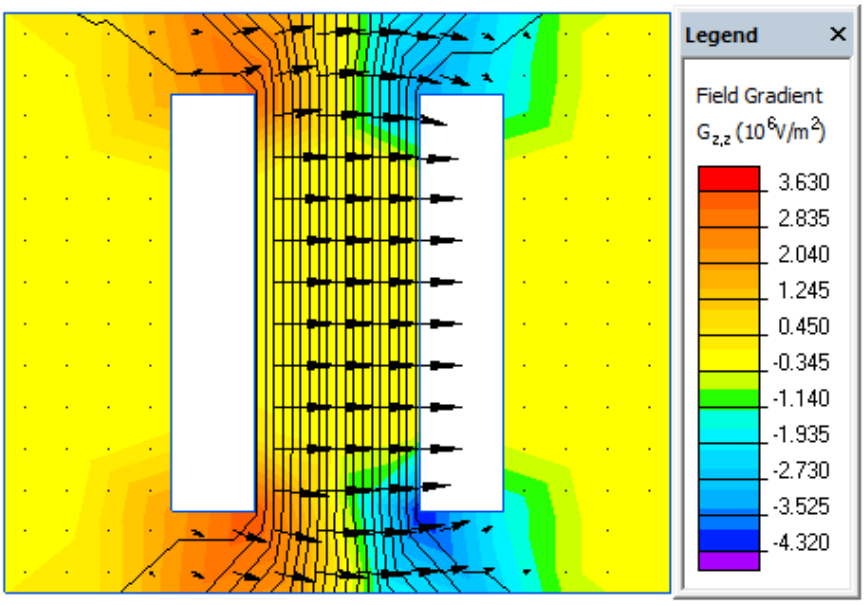

Fig. A.1. Electric field gradient in a planar detector with two electrodes maintained at opposite potential, calculated using Ref. [17].

carriers is dependent on the electric field, which is determined using the Poisson equation, i.e.,

$$\begin{aligned} \nabla^2\phi &= \frac{-\rho}{\epsilon_0\epsilon_r} \\ &= \frac{-Ne}{\epsilon_0\epsilon_r}, \end{aligned} \tag{A.9}$$

where, N = Impurity concentration given by N_A - N_D, e = Electronic charge = 1.6 x 10^{-19} C, ϵ_0 = Absolute permittivity of free space = 8.854 x 10^{-12} F m^{-1}, ϵ_r = Dielectric constant (16 in Germanium).
For symmetric potential along the Y and Z-axis, equation (A.9) can be written as:

$$\frac{d^2\phi}{dx^2} = \frac{-Ne}{\epsilon_0\epsilon_r} \tag{A.10}$$

The solution to the equation (A.10) is calculated using the boundary condition:

$$\phi(d) - \phi(0) = V \tag{A.11}$$

The general solution is given by [18]:

$$\phi(x) = \frac{-\rho}{2\epsilon}x^2 + \frac{V + \frac{\rho}{2\epsilon}(d^2)}{d}x \tag{A.12}$$

The signal/pulse produced at an electrode at any instant t depends on the charge carrier's drift velocity, a function of the electric field as described in equation (A.8). With the increase in the field, drift velocity increases and reaches maximum or saturation at a high field. The charge drift also depends on the crystalline lattice direction, as studied by Mihailescu et al. in Ref. [105]. The velocity is maximum along the [100] direction. Therefore, the anisotropic nature of crystallines affects signal formation.

A.3 Gamma-ray interaction process and peak formation

Due to nuclear de-excitation in a radioactive source, the gamma-rays are emitted in a 4π solid angle. When gamma-rays enter the detector, it undergoes interaction in the detector volume with one or two successive mechanisms amongst PEE, CS, and PEE. After the interaction, the detector material produces an electrical signal, which is further detected with accompanying electronics. The important factor for any detector to collect photons is that the amount of charge carriers produced in the detector is proportional to the number of photons interacting. Therefore, there is no loss of signal. Depending upon the detector material, the photon energy conversion may be different. For e.g., in a scintillator detector, there is the production of photoelectrons from lower energy light from crystal and electron-hole pair generation in a semiconductor detector. The dominant interaction processes occurring in the detector are represented in Fig. A.2 (a)-(h), i.e., PEE, CS, and PP with higher relative cross-sections. The corresponding response of gamma-ray interaction in the detector as a function of the energy has been plotted in the gamma-ray spectrum Fig. A.2(i), for a reference germanium detector with an energy resolution of the order of keV. In this figure, the cylinder represents active detector volume, while the shielding is represented by a blue envelope outside the detector. The gamma-ray spectrum is a fingerprint of a nucleus. It is unique for each nucleus depending upon the gamma-ray energy, and its intensity is a feature of its half-life. Fig. A.2(a), shows the PEE event from active detector volume, i.e., the incoming photon loses full energy from the bound electron in germanium leading to the production of a photoelectron. It leads to full energy photopeak event (Full gamma-ray energy is absorbed in the detector) as represented in Fig. A.2(i) as a Full-energy peak. In Fig. A.2(b), the incident photon loses energy in the shielding, and the characteristic X-ray is produced and interacts with the detector. It can be detected as a characteristic X-ray of the shielding material in the gamma-ray spectrum. Fig. A.2(c) represents the CS event, in which the scattered photon again gets detected in the detector leading to a Full-energy photopeak event. The CS events as represented in A.2(d)(scattered photon escapes)-(e)(incoming photon scatters from shielding) lead to secondary and primary photon continuum, respectively. Fig. A.2(f)-(h) denotes PP event. However, in (f), both outcoming photons are detected as Full-energy peaks, marked in Fig. A.2(i).

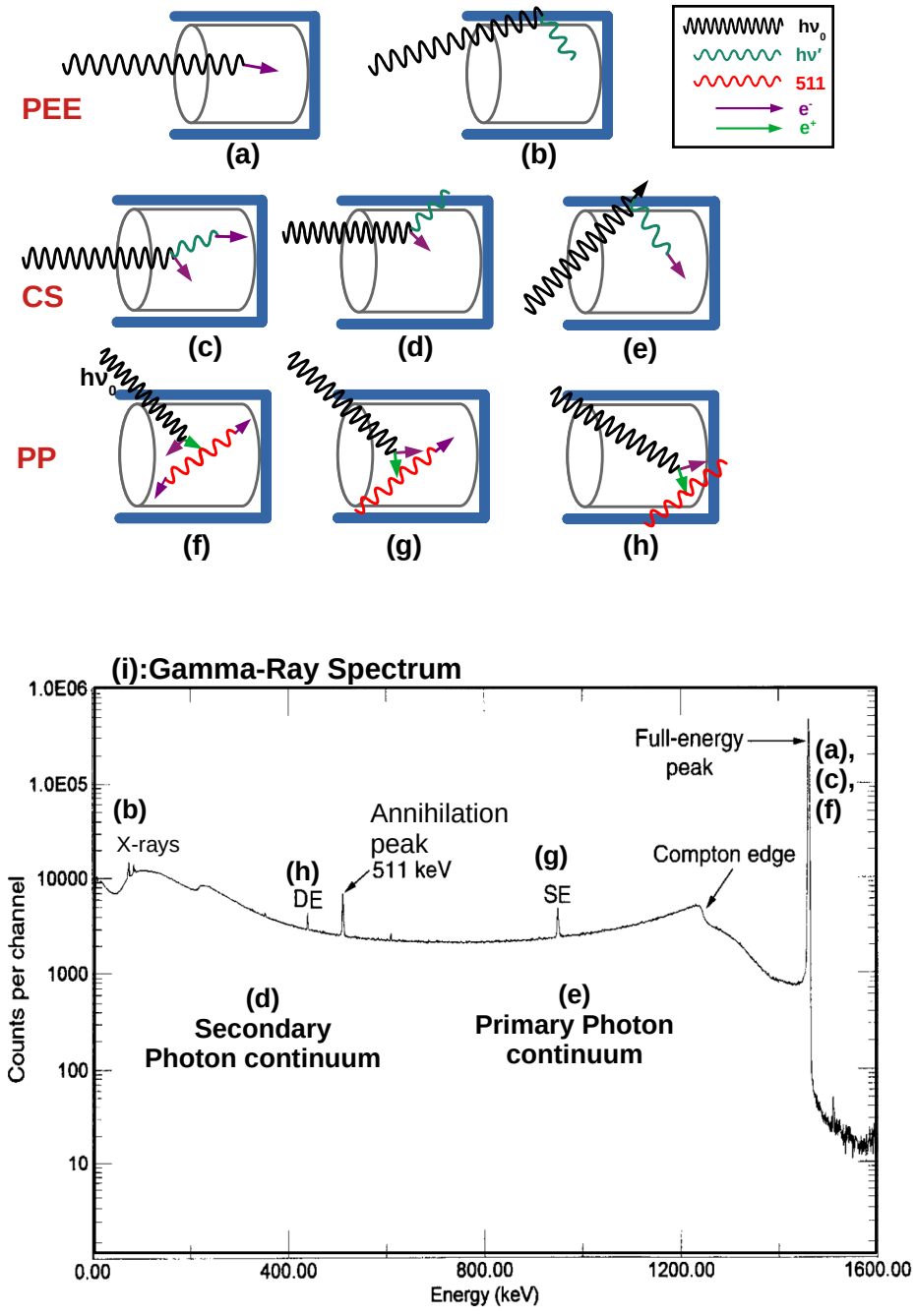

Fig. A.2. Effect of mono-energetic gamma-ray interaction on detector response for dominant interactions PEE, CS, and PP. The pictorial representation of different ways the gamma-ray may interact inside the detector is exhibited through (a)-(h). The detector is represented by a black cylinder, and the outside blue material represents detector shielding. The corresponding gamma-ray spectrum for each of the processes is denoted in (i) [18].

While in (g), one photon is detected, appearing as 511 annihilation peak, and the other escapes the detector leading to Single Escape (denoted as SE in Fig. A.2(i)) event, appearing at $h\nu_0$-511 keV. In (h), both photons escape the detector, leading to Double Escape (denoted as DE in Fig. A.2(i) at $h\nu_0$-1022 keV) event. The photon continuum may also be generated by 511 keV gamma-rays that may Compton scatter inside the detector and/or the outside shielding.

APPENDIX B

SIS digitizer parameter settings

Below are the settings of the SIS digitizer for coincidence setup between PSPGe and PSD for all the segments.

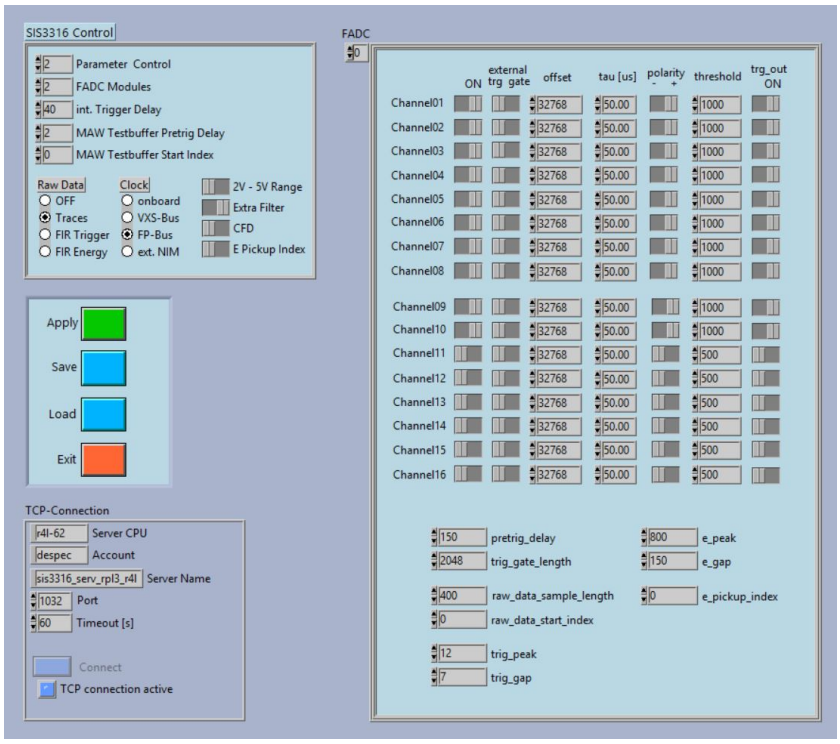

(a)

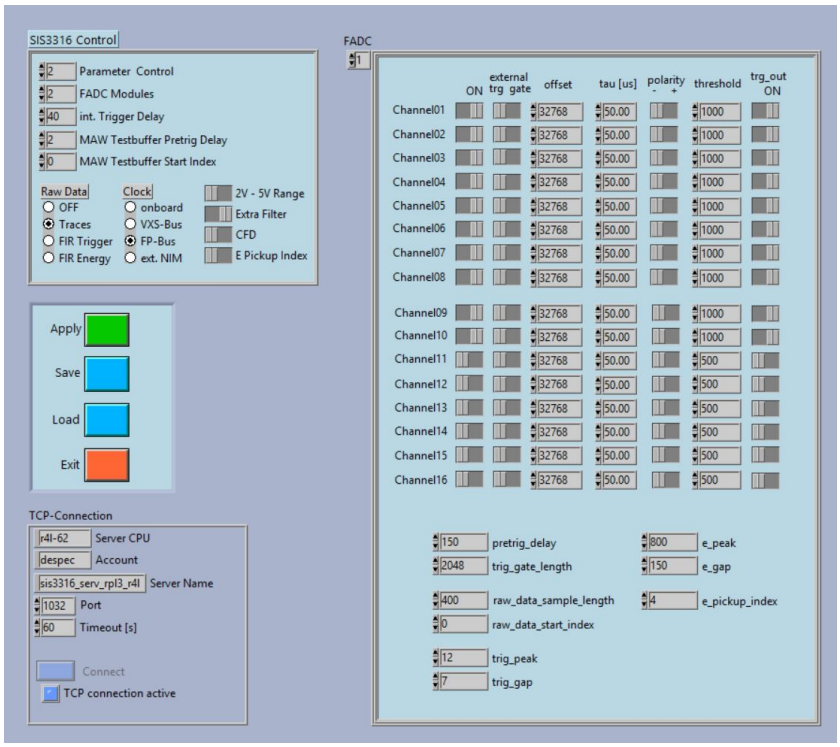

(b)

Fig. B.1. Signal handling and processing in SIS digitizer. The two images denote the SIS settings for (a) DC (b) AC electrodes.

APPENDIX C

Mean pulse using chi-square

The matrix of pulses is constructed for different cuts along the 0°scan (Set-A/side scan) and one cut along the 90°(Set-B front scan), represented in Fig. C.1. The pulses obtained for one of the cuts along the Set-A and Set-B scans is shown in Fig. C.2(a) and C.2(b), respectively.

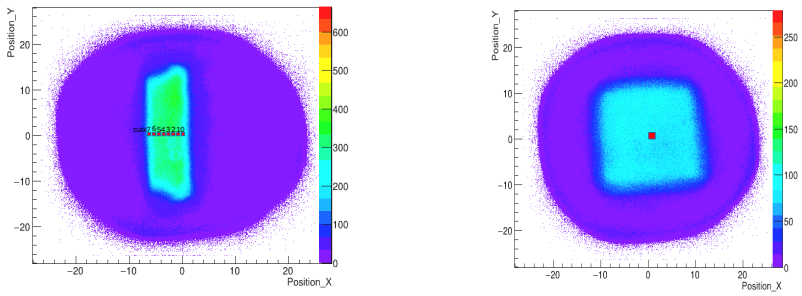

Fig. C.1. Representation of different cuts along the Set-A and one central cut along the Set-B measurement.

The χ^2 values obtained for the comparison of the pulses for the two sets in Fig. C.2 is shown in Fig. C.3. The very high values, i.e., χ^2>15x10^6 correspond to the baseline pulse in Fig. C.2(a) compared to all the pulses with the pulses in Fig. C.2(b). These pulses can directly be rejected by selecting a lower threshold. Further, the inset in Fig. C.3 represents zoomed spectrum. Later, different χ^2 thresholds are selected to calculate an average pulse. As a reference, Fig. C.4 represents pulse along the front and side scans for different thresholds. For χ^2 threshold 0<χ^2<1000 (Fig. C.4(a)), the average pulse along the two scans match. While for higher threshold selection, the pulses do not match, represented by Fig. C.4(b).

Therefore, for the calculation of the mean pulse along the two scans, the

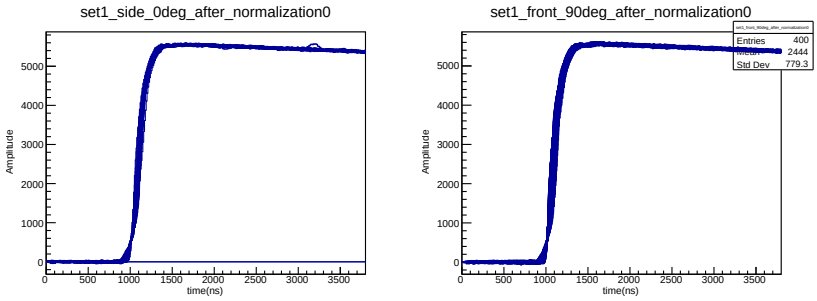

Fig. C.2. Normalized side and front pulses obtained for one of the cuts in the 2D plot in Fig. C.1(a) Set-A (sideview) pulses and (b) Set-B (frontview) pulses.

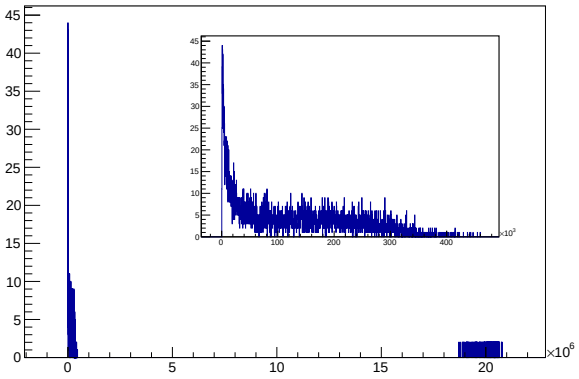

Fig. C.3. Plot of χ^2 obtained by comparing front and side pulses, shown in Fig. C.2. Few events with very large χ^2 are from the comparison of one baseline pulse in sideview being compared to all pulses in frontview. The inset image represents the zoomed χ^2 plot, i.e., values less than 0.5x10^6.

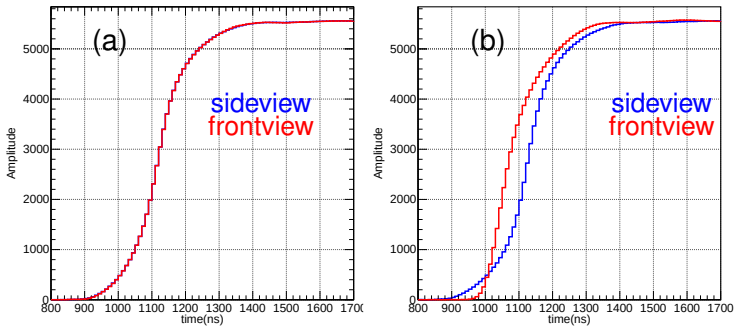

Fig. C.4. Average/mean front (red colored) and side (blue colored) pulse obtained by using different χ^2 cuts in plot C.3, i.e., (a) $0<\chi^2<1000$, (b) $260000<\chi^2<320000$.

threshold value of $\chi^2<1000$ has been selected.

APPENDIX D

Equations for position resolution calculation

The slope of the linear fit has been employed to obtain position difference (dX or dY) for pairs of all points and the corresponding uncertainty has been calculated through error propagation. The weighted mean of all points has been calculated using the errors of the data points. The linear fit using equation (D.1) provides slope m, say for n data points. The equation (D.3) is used to calculate dx ($x_{i+1} - x_i$) for each (x_i,y_i) i running from 1 to n. Therefore, n-1 data points are obtained for dx calculation. The error in X_i and X_{i+1} is calculated using equations (D.6) and (D.7), respectively. The error for each dx is also calculated using error propagation in equation (D.9). The weighted mean is calculated using n-1 values of dx_i using equation (D.10).

$$f(x) = m * x + c \tag{D.1}$$

$$m = \frac{y_{i+1} - y_i}{x_{i+1} - x_i} \tag{D.2}$$

$$x_{i+1} - x_i = \frac{y_{i+1} - y_i}{m} \tag{D.3}$$

$$dx_i = \frac{y_{i+1}}{m} - \frac{y_i}{m} \tag{D.4}$$

$$dx_i = X_{i+1} - X_i \tag{D.5}$$

$$\delta X_i = X_i \sqrt{[(\frac{\delta y_i}{y_i})^2 + (\frac{\delta m}{m})^2]} \tag{D.6}$$

$$\delta X_{i+1} = X_{i+1} \sqrt{[(\frac{\delta y_{i+1}}{y_{i+1}})^2 + (\frac{\delta m}{m})^2]} \tag{D.7}$$

$$\delta(dx_i) = \sqrt{\delta X_{i+1}{}^2 + \delta X_i{}^2} \tag{D.8}$$

$$\delta(dx_i) = \sqrt{[X_{i+1}{}^2\{(\frac{\delta y_{i+1}}{y_{i+1}})^2 + (\frac{\delta m}{m})^2\}] + [X_i{}^2\{(\frac{\delta y_i}{y_i})^2 + (\frac{\delta m}{m})^2\}]} \tag{D.9}$$

$$\bar{x} = \frac{\sum_{i=1}^{n-1} w_i dx_i}{\sum_{i=1}^{n-1} w_i} \tag{D.10}$$

$$w_i = \frac{1}{\delta(dx_i)^2} \tag{D.11}$$

The error is calculated using

$$\delta(\bar{x}) = \frac{1}{\sqrt{\sum_{i=1}^{n-1} w_i}} \tag{D.12}$$

The position resolution is given as $\bar{x} \pm \delta(\bar{x})$

APPENDIX E

Gain matching : slow TOT

The calibrated slow TOT spectrum is shown in Fig. E.1.

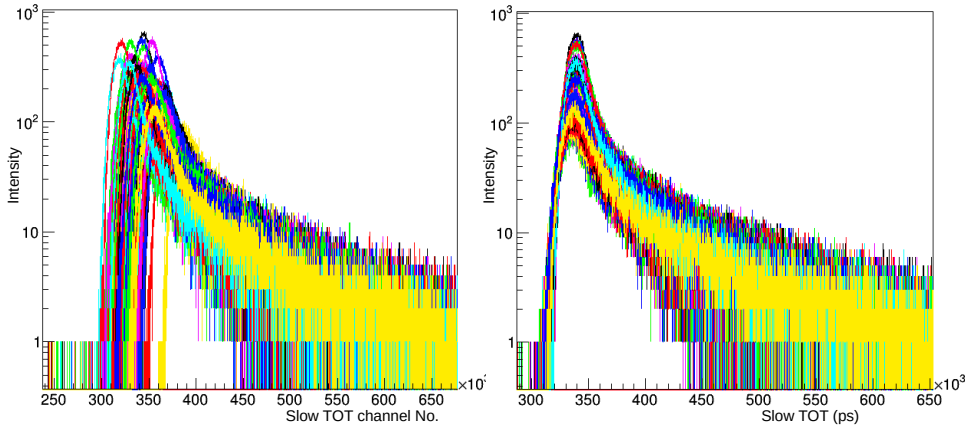

Fig. E.1. TAMEX Slow TOT channels (a) before and (b) after the gain matching procedure.

APPENDIX F

2D image Projection

The projection of the 2D images, obtained from PSD for (a) Set-A (Fig. 3.6(a)) and, (b) Set-B (Fig. 3.6(b)) measurements using centroid method for coincidence setup, are shown in Fig. F.1. The X and Y projection of Fig. 3.6(a) are shown in Fig. F.1(a)-(b), respectively, which represents the depth of the PSPGe detector. Fig. F.1(c)-(d) denotes the projections along X and Y of Fig. 3.6(b), respectively, representing the lateral view of the PSPGe detector.

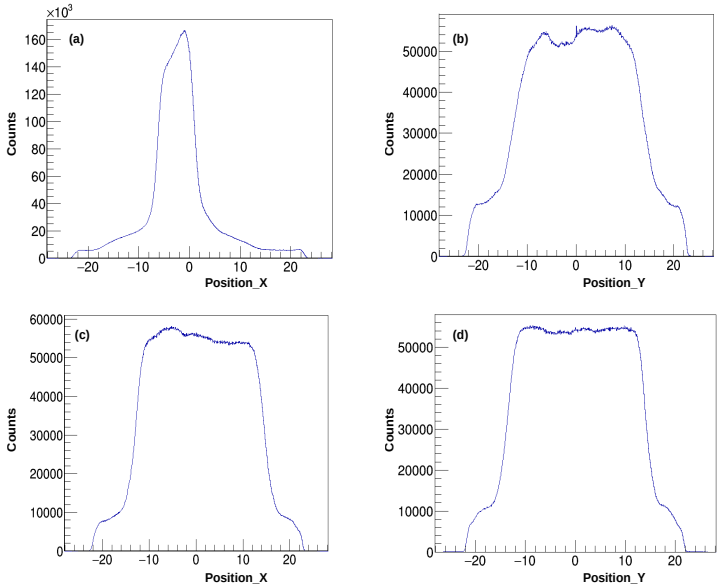

Fig. F.1. The projection of 2D image for both sets of scans shown in Fig. 3.6 are plotted. (a) Projection X of Fig. 3.6(a), (b) Projection Y of Fig. 3.6(a), Projection X of Fig. 3.6(b), Projection Y of Fig. 3.6(b).

Bibliography

[1] https://physics.nist.gov/PhysRefData/XrayMassCoef/ElemTab/z32.html, 2023.

[2] D. Dannheim, T. Frisson, and S. Kulis. Lab experiment: Characterization of silicon photomultipliers. http://cern-danube-school.uns.ac.rs/assets/labs/Lab%207_SIPM.pd, November 2013.

[3] László Varga. Characterization and optimization of silicon photomultipliers and small size scintillator tiles for future calorimeter applications. https://tuprints.ulb.tu-darmstadt.de/2624/, 2017.

[4] https://www.onsemi.com/pub/Collateral/AND9782-D.PDF, 2023.

[5] https://www.agata.org/, 2023.

[6] D Weisshaar, D Bazin, PC Bender, CM Campbell, F Recchia, V Bader, T Baugher, J Belarge, MP Carpenter, HL Crawford, et al. The performance of the γ-ray tracking array gretina for γ-ray spectroscopy with fast beams of rare isotopes. *Nuclear Instruments and Methods in Physics Research Section A: Accelerators, Spectrometers, Detectors and Associated Equipment*, 847:187–198, 2017.

[7] https://www.yumpu.com/en/document/read/22597498/b-birkenbach-hk-542-characterisation-of-agata-detectors/5, 2023.

[8] Karl Herholz, Helge Schopphoff, Mathias Schmidt, Rüdiger Mielke, Wolfgang Eschner, Klemens Scheidhauer, Harald Schicha, Wolf-Dieter Heiss, and Klaus Ebmeier. Direct comparison of spatially normalized pet and spect scans in alzheimer's disease. *Journal of Nuclear Medicine*, 43(1): 21–26, 2002.

[9] https://www.nndc.bnl.gov/ensdf/, 2023.

[10] https://www.luxiumsolutions.com/radiation-detection-scintillators/crystal-scintillators/lyso-scintillation-crystals, 2023.

[11] Matthew R. Dimmock, Andrew J. Boston, John R. Cresswell, Ian Lazarus, Patrice Medina, Paul Nolan, Camille Parisel, Cayetano Santos, John Simpson, and Carl Unsworth. Validation of pulse shape simulations for an agata prototype detector. *IEEE Transactions on Nuclear Science*, 56 (4):2415–2425, 2009.

[12] B. De Canditiis and G. Duchêne. Simulations using the pulse shape comparison scanning technique on an agata segmented hpge gamma-ray detector. *The European Physical Journal A*, 56(10):1–13, 2020.

[13] Namita Goel. Spatial characterisation of a 36-fold segmented agata detector via a novel scanning system. `https://tuprints.ulb.tu-darmstadt.de/2624/`, 2011.

[14] A Hernandez-Prieto, B Quintana, S Martìn, and C Domingo-Pardo. Study of accuracy in the position determination with salsa, a γ-scanning system for the characterization of segmented hpge detectors. *Nuclear Instruments and Methods in Physics Research Section A: Accelerators, Spectrometers, Detectors and Associated Equipment*, 823:98–106, 2016.

[15] `https://www.struck.de/sis3316-2014-03-20.pdf`, 2023.

[16] Arzoo Sharma, R Palit, J Gerl, M Górska, H Schaffner, T Habermann, S Saha, Biswajit Das, P Dey, R Donthi, BS Naidu, S Mandal, and Pushpendra P Singh. Scanning of a double-sided germanium strip detector. In *7th Int. Conf. on Advancements in Nuclear Instrumentation Measurement Methods and their Applications*. Eur. Phys. J. Web of Conferences, 2021.

[17] `https://quickfield.com/free_soft.htm`, 2023.

[18] Glenn F Knoll. *Radiation detection and measurement*. John Wiley & Sons, 2010.

[19] Hany Kasban, MAM El-Bendary, and DH Salama. A comparative study of medical imaging techniques. *International Journal of Information Science and Intelligent System*, 4(2):37–58, 2015.

[20] Jaehong Key and James F Leary. Nanoparticles for multimodal in vivo imaging in nanomedicine. *International journal of nanomedicine*, 9:711, 2014.

[21] Takayuki Yanagida. Inorganic scintillating materials and scintillation detectors. *Proceedings of the Japan Academy, Series B*, 94(2):75–97, 2018.

[22] `https://www.luxiumsolutions.com/files/1131/download`, 2023.

[23] `https://www.advatech-uk.co.uk/`, 2023.

[24] `https://www.first-sensor.com/cms/upload/appnotes/AN_SiPM_Introduction_E.pdf`, 2023.

[25] D. Renker. Geiger-mode avalanche photodiodes, history, properties and problems. *Nuclear Instruments and Methods in Physics Research Section A: Accelerators, Spectrometers, Detectors and Associated Equipment*, 567(1):48–56, 2006. ISSN 0168-9002. doi: https://doi.org/10.1016/j.nima.2006.05.060. URL `https://www.sciencedirect.com/science/article/pii/S0168900206008680`. Proceedings of the 4th International Conference on New Developments in Photodetection.

[26] K Vetter, A Kuhn, IY Lee, RM Clark, M Cromaz, MA Deleplanque, RM Diamond, P Fallon, GJ Lane, AO Macchiavelli, et al. Performance of the greta prototype detectors. *Nuclear Instruments and Methods in Physics Research Section A: Accelerators, Spectrometers, Detectors and Associated Equipment*, 452(1-2):105–114, 2000.

[27] SERKAN Akkoyun, Alejandro Algora, B Alikhani, F Ameil, G De Angelis, L Arnold, A Astier, Ayse Ataç, Y Aubert, C Aufranc, et al. Agata—advanced gamma tracking array. *Nuclear Instruments and Methods in Physics Research Section A: Accelerators, Spectrometers, Detectors and Associated Equipment*, 668:26–58, 2012.

[28] Dino Bazzacco. The advanced gamma ray tracking array agata. *Nuclear Physics A*, 746:248–254, 2004.

[29] Zhong He. Review of the shockley–ramo theorem and its application in semiconductor gamma-ray detectors. *Nuclear Instruments and Methods in Physics Research Section A: Accelerators, Spectrometers, Detectors and Associated Equipment*, 463(1-2):250–267, 2001.

[30] L Lewandowski, P Reiter, B Birkenbach, B Bruyneel, E Clement, J Eberth, H Hess, C Michelagnoli, H Li, RM Perez-Vidal, et al. Pulse-shape analysis and position resolution in highly segmented hpge agata detectors. *The European Physical Journal A*, 55(5):1–13, 2019.

[31] M. Nespolo. *Pulse Shape Analysis with Germanium Detectors: From MARS to AGATA*. Università degli Studi di Padova, 2004. URL `https://books.google.se/books?id=UbVwwAEACAAJ`.

[32] FCL Crespi, F Camera, O Wieland, G Benzoni, S Brambilla, B Million, and D Montanari. A pulse shape analysis algorithm for hpge detectors. *Nuclear Instruments and Methods in Physics Research Section A: Accelerators, Spectrometers, Detectors and Associated Equipment*, 570(3): 459–466, 2007.

[33] A. Olariu, P. Desesquelles, Ch. Diarra, P. Medina, C. Parisel, and C.S.Obot.A. Collaboration. Pulse shape analysis for the location of the γ-interactions in agata. *IEEE Transactions on Nuclear Science*, 53(3): 1028–1031, 2006. doi: 10.1109/TNS.2006.875130.

[34] S.N. Liddick, I.G. Darby, and R.K. Grzywacz. Algorithms for pulse shape analysis using silicon detectors. *Nuclear Instruments and Methods in Physics Research Section A: Accelerators, Spectrometers, Detectors and Associated Equipment*, 669:70–78, 2012. ISSN 0168-9002. doi: https://doi.org/10.1016/j.nima.2011.12.034. URL `https://www.sciencedirect.com/science/article/pii/S016890021102225X`.

[35] O Wieland, F Camera, B Million, A Bracco, and J van der Marel. Pulse distributions and tracking in segmented detectors. *Nuclear Instruments and Methods in Physics Research Section A: Accelerators, Spectrometers, Detectors and Associated Equipment*, 487(3):441–449, 2002.

[36] Jonathan P Wright, LJ Harkness-Brennan, AJ Boston, DS Judson, M Labiche, PJ Nolan, RD Page, F Pearce, David C Radford, J Simpson, et al. Position resolution simulations for the inverted-coaxial germanium detector, sigma. *Nuclear Instruments and Methods in Physics Research Section A: Accelerators, Spectrometers, Detectors and Associated Equipment*, 892:84–92, 2018.

[37] Anton Khaplanov, Bo Cederwall, and Stanislav Tashenov. Position sensitivity of segmented planar hpge detectors for the despec project at fair. *Nuclear Instruments and Methods in Physics Research Section A: Accelerators, Spectrometers, Detectors and Associated Equipment*, 592(3): 325–333, 2008.

[38] N Larson, SN Liddick, M Bennett, A Bowe, A Chemey, C Prokop, A Simon, A Spyrou, S Suchyta, SJ Quinn, et al. High efficiency beta-decay spectroscopy using a planar germanium double-sided strip detector. *Nuclear Instruments and Methods in Physics Research Section A: Accelerators, Spectrometers, Detectors and Associated Equipment*, 727:59–64, 2013.

[39] E Rintoul, AJ Boston, HC Boston, A Caffrey, JR Cresswell, LJ Harkness-Brennan, DS Judson, PJ Nolan, J Platt, C Unsworth, et al. Characterisation of the charge collection properties in a segmented planar hpge detector. *Nuclear Instruments and Methods in Physics Research Section A: Accelerators, Spectrometers, Detectors and Associated Equipment*, 987: 164804, 2021.

[40] S Shimoura. Position sensitivity of ge detectors and its applications to in-beam nuclear spectroscopy. *Nuclear Instruments and Methods in Physics Research Section A: Accelerators, Spectrometers, Detectors and Associated Equipment*, 525(1):188–192, 2004. ISSN 0168-9002. doi: https://doi.org/10.1016/j.nima.2004.03.044. URL `https://www.sciencedirect.com/science/article/pii/S0168900204003870`. Proceedings of the International Conference on Imaging Techniques in Subatomic Physics, Astrophysics, Medicine, Biology and Industry.

[41] C.S. Lee, J.H. Lee, J.Y. Moon, Y.K. Kwon, and Y. Gono. Characteristics of a planar-type segmented germanium detector on gamma-ray detection, linear polarization and position information. *Nuclear Physics A*, 718:550–552, 2003. ISSN 0375-9474. doi: https://doi.org/10.1016/S0375-9474(03)00840-6. URL `https://www.sciencedirect.com/science/article/pii/S0375947403008406`.

[42] `https://www.dicardiology.com/article/spect-scanner-vs-pet-which-best`, 2023.

[43] C. Messa, D. Perani, G. Lucignani, G.A. Zenorini, F. Zito, G. Rizzo, F. Grassi, A. Del Sole, M. Franceschi, M.C. Gilardi, and F. Fazio. High-resolution technetium-99m-hmpao spect in patients with probable alzheimer's disease: comparison with fluorine-18-fdg pet. *Journal of Nuclear Medicine*, 35(2):210–216, 1994.

[44] Konstantinos Spartiotis, Anssi Leppänen, Tuomas Pantsar, Jouni Pyyhtiä, Pasi Laukka, Kari Muukkonen, Olli Männistö, Jussi Kinnari, and Tom Schulman. A photon counting cdte gamma- and x-ray camera. *Nuclear Instruments and Methods in Physics Research Section A: Accelerators, Spectrometers, Detectors and Associated Equipment*, 550(1):267–277, 2005. ISSN 0168-9002.

[45] Chengcheng Zhu, Henrik Haraldsson, Bing Tian, Karl Meisel, Nerissa Ko, Michael Lawton, John Grinstead, Sinyeob Ahn, Gerhard Laub, Christopher Hess, et al. High resolution imaging of the intracranial vessel wall at 3 and 7 t using 3d fast spin echo mri. *Magnetic Resonance Materials in Physics, Biology and Medicine*, 29(3):559–570, 2016.

[46] B Ward, AC Baker, and VF Humphrey. Nonlinear propagation applied to the improvement of resolution in diagnostic medical ultrasound. *The Journal of the Acoustical Society of America*, 101(1):143–154, 1997.

[47] JKA Alderson and EFJ Ring. 'sprite'high resolution thermal imaging system. *Thermol*, 1:110–114, 1995.

[48] John A Kennedy, Ora Israel, and Alex Frenkel. 3d iteratively reconstructed spatial resolution map and sensitivity characterization of a dedicated cardiac spect camera. *Journal of Nuclear Cardiology*, 21(3):443–452, 2014.

[49] Stephen E Derenzo, TF Budinger, RH Huesman, and JL Cahoon. Dynamic positron emission tomography in man using small bismuth germanate crystals. Technical report, Lawrence Berkeley Lab., 1982.

[50] W.W. Moses. Fundamental limits of spatial resolution in pet. *Nuclear Instruments and Methods in Physics Research Section A: Accelerators, Spectrometers, Detectors and Associated Equipment*, 648:S236–S240, 2011. ISSN 0168-9002.

[51] M.E. Phelps. Positron emission tomography provides molecular imaging of biological processes. *Proceedings of the National Academy of Sciences USA*, 97(16):9226–9233, 2000.

[52] Eiji Sakai. Recent measurements on scintillator-photodetector systems. *IEEE Transactions on Nuclear Science*, 34(1):418–422, 1987.

[53] Ina Holl, Eckart Lorenz, and Gikas Mageras. A measurement of the light yield of common inorganic scintillators. *IEEE Transactions on Nuclear Science*, 35(1):105–109, 1988.

[54] Marvin J Weber and Roch R Monchamp. Luminescence of bi4 ge3 o12: Spectral and decay properties. *Journal of Applied Physics*, 44(12):5495–5499, 1973.

[55] Mikhail S Alekhin, Sandra Weber, Karl W Krämer, and Pieter Dorenbos. Optical properties and defect structure of sr2+ co-doped labr3: 5% ce scintillation crystals. *Journal of luminescence*, 145:518–524, 2014.

[56] Weiping Gong, Yue Wu, Rui Zhang, and Marcelle Gaune-Escard. Phase equilibrium in lanthanide halide systems: assessment of cebr3 and mbr–cebr3 systems (m= li, na, k, rb, cs). *Calphad*, 36:44–51, 2012.

[57] DF Anderson. Properties of the high-density scintillator cerium fluoride. *IEEE Transactions on Nuclear Science*, 36(1):137–140, 1989.

[58] Yuki Shimizu, Makoto Minowa, Wataru Suganuma, and Yoshizumi Inoue. Dark matter search experiment with caf2 (eu) scintillator at kamioka observatory. *Physics Letters B*, 633(2-3):195–200, 2006.

[59] Moszyński Laval, M Moszyński, R Allemand, E Cormoreche, P Guinet, R Odru, and J Vacher. Barium fluoride—inorganic scintillator for subnanosecond timing. *Nuclear Instruments and Methods in Physics Research*, 206(1-2):169–176, 1983.

[60] EVD Van Loef, LP Dorenbos, CWE Van Eijk, K Kramer, and HU Gudel. Scintillation properties of lacl/textsubscript 3: Ce/textsuperscript 3+/crystals: fast, efficient, and high-energy resolution scintillators. *IEEE transactions on nuclear science*, 48(3):341–345, 2001.

[61] Takayuki Yanagida, Masanori Koshimizu, Go Okada, Takahiro Kojima, Junya Osada, and Noriaki Kawaguchi. Comparative study of nondoped and eu-doped sri2 scintillator. *Optical Materials*, 61:119–124, 2016.

[62] Seiichi Yamamoto and Hideki Tomita. Comparison of light outputs, decay times, and imaging performance of a zns (ag) scintillator for alpha particles, beta particles, and gamma photons. *Applied Radiation and Isotopes*, 168:109527, 2021.

[63] BC Grabmaier. Crystal scintillators. *IEEE Transactions on Nuclear Science*, 31(1):372–376, 1984.

[64] AA Annenkov, MV Korzhik, and P Lecoq. Lead tungstate scintillation material. *Nuclear Instruments and Methods in Physics Research Section A: Accelerators, Spectrometers, Detectors and Associated Equipment*, 490 (1-2):30–50, 2002.

[65] Kazumasa Takagi and Tokuumi Fukazawa. Cerium-activated gd2sio5 single crystal scintillator. *Applied Physics Letters*, 42(1):43–45, 1983.

[66] CL Melcher and JS Schweitzer. Cerium-doped lutetium oxyorthosilicate: a fast, efficient new scintillator. *IEEE Transactions on Nuclear Science*, 39(4):502–505, 1992.

[67] Ludivine Pidol, Andrée Kahn-Harari, Bruno Viana, Eric Virey, Bernard Ferrand, Pieter Dorenbos, Johan TM de Haas, and Carel WE van Eijk. High efficiency of lutetium silicate scintillators, ce-doped lps, and lyso crystals. *IEEE Transactions on Nuclear Science*, 51(3):1084–1087, 2004.

[68] Weerapong Chewpraditkul, Chalerm Wanarak, Tomasz Szczesniak, Marek Moszynski, Vitezslav Jary, Alena Beitlerova, and Martin Nikl. Comparison of absorption, luminescence and scintillation characteristics in lu1. 95y0. 05sio5: Ce, ca and y2sio5: Ce scintillators. *Optical Materials*, 35 (9):1679–1684, 2013.

[69] Jarek Glodo, William M Higgins, Edgar VD van Loef, and Kanai S Shah. Scintillation properties of 1 inch cs_2liycl_6:ce crystals. *IEEE Transactions on Nuclear Science*, 55(3):1206–1209, 2008.

[70] A Lempicki, MH Randles, D Wisniewski, M Balcerzyk, C Brecher, and AJ Wojtowicz. Lualo/sub 3: Ce and other aluminate scintillators. *IEEE Transactions on Nuclear Science*, 42(4):280–284, 1995.

[71] H Ogino, A Yoshikawa, M Nikl, K Kamada, and T Fukuda. Scintillation characteristics of pr-doped lu3al5o12 single crystals. *Journal of crystal growth*, 292(2):239–242, 2006.

[72] VG Baryshevsky, MV Korzhik, VI Moroz, VB Pavlenko, AA Fyodorov, SA Smirnova, OA Egorycheva, and VA Kachanov. Yalo 3: Ce-fast-acting scintillators for detection of ionizing radiation. *Nuclear Instruments and Methods in Physics Research, Section B*, 58(2):291–293, 1991.

[73] Takayuki Yanagida, Hiromitsu Takahashi, Takeshi Ito, Daisuke Kasama, Teruaki Enoto, Mitsuhiro Sato, Shinya Hirakuri, Motohide Kokubun, Kazuo Makishima, Takagimi Yanagitani, et al. Evaluation of properties of yag (ce) ceramic scintillators. *IEEE transactions on nuclear science*, 52 (5):1836–1841, 2005.

[74] Kei Kamada, Takanori Endo, Kousuke Tsutumi, Takayuki Yanagida, Yutaka Fujimoto, Akihiro Fukabori, Akira Yoshikawa, Jan Pejchal, and Martin Nikl. Composition engineering in cerium-doped (lu, gd) 3 (ga, al) 5o12 single-crystal scintillators. *Crystal Growth & Design*, 11(10):4484–4490, 2011.

[75] Jianming Chen, Rihua Mao, Liyuan Zhang, and Ren-Yuan Zhu. Large size lso and lyso crystals for future high energy physics experiments. *IEEE Transactions on Nuclear Science*, 54(3):718–724, 2007.

[76] Federica Villa, Danilo Bronzi, Michele Vergani, Yu Zou, Alessandro Ruggeri, Franco Zappa, and Alberto Dalla Mora. Analog sipm in planar cmos technology. In *2014 44th European Solid State Device Research Conference (ESSDERC)*, pages 294–297. IEEE, 2014.

[77] CM Pepin, C St-Pierre, J-C Forgues, Y Kurata, N Shimura, T Usui, T Takeyama, H Ishibashi, and R Lecomte. Physical characterization of the labpet™ lgso and lyso scintillators. In *2007 IEEE Nuclear Science Symposium Conference Record*, volume 3, pages 2292–2295. IEEE, 2007.

[78] Mikiko Ito, Jin Pyo Lee, and Jae Sung Lee. Timing performance study of new fast pmts with lyso for time-of-flight pet. *IEEE Transactions on Nuclear Science*, 60(1):30–37, 2012.

[79] A Bornheim, MH Hassanshahi, M Griffioen, J Mao, A Mangu, C Peña, M Spiropulu, S Xie, and Z Zhang. Lyso-based precision timing detectors with sipm readout. *Nuclear Instruments and Methods in Physics Research Section A: Accelerators, Spectrometers, Detectors and Associated Equipment*, 896:75–81, 2018.

[80] Alessandro Ferri, Alberto Gola, Nicola Serra, Alessandro Tarolli, Nicola Zorzi, and Claudio Piemonte. Performance of fbk high-density sipm technology coupled to ce: Lyso and ce: Gagg for tof-pet. *Physics in Medicine & Biology*, 59(4):869, 2014.

[81] M. Ginsz. Characterization of high-purity, multi-segmented germanium detectors. `http://www.theses.fr/2015STRAE047`, 2015.

[82] AJ Bird, Z He, and D Ramsden. Multi-channel readout of crossed-wire anode photomultipliers. *Nuclear Instruments and Methods in Physics Research Section A: Accelerators, Spectrometers, Detectors and Associated Equipment*, 348(2-3):668–672, 1994.

[83] A Banerjee, S Mandal, Pratap Roy, S Mukhopadhyay, G Mukherjee, M Kumar, A Jhingan, and R Palit. A compact scintillator based position sensitive detector system for gamma ray tracking applications. *Nuclear Instruments and Methods in Physics Research Section A: Accelerators, Spectrometers, Detectors and Associated Equipment*, 930:100–104, 2019.

[84] Biswajit Das, A Kundu, R Palit, V Malik, P Dey, D Negi, SK Jadhav, AT Vazhappilly, and BS Naidu. Development of a gagg (ce)-based compact 3d scanning setup for assessment of active volume in γ-ray detectors. *Nuclear Instruments and Methods in Physics Research Section A: Accelerators, Spectrometers, Detectors and Associated Equipment*, 1048:167928, 2023.

[85] C Domingo-Pardo, N Goel, T Engert, J Gerl, I Kojouharov, H Schaffner, F Didierjean, G Duchêne, and MH Sigward. A novel γ-ray imaging method for the pulse-shape characterization of position sensitive semiconductor radiation detectors. *Nuclear Instruments and Methods in Physics Research Section A: Accelerators, Spectrometers, Detectors and Associated Equipment*, 643(1):79–88, 2011.

[86] C.M. Lederer, J.M. Jaklevic, and J.M. Hollander. In-beam gamma-ray spectroscopy of even mo and ru isotopes. *Nuclear Physics A*, 169(3):449–488, 1971. ISSN 0375-9474. doi: https://doi.org/10.1016/0375-9474(71)90697-X. URL `https://www.sciencedirect.com/science/article/pii/037594747190697X`.

[87] AK Mistry, HM Albers, T Arıcı, A Banerjee, G Benzoni, B Cederwall, J Gerl, M Górska, O Hall, N Hubbard, et al. The despec setup for gsi and fair. *Nuclear Instruments and Methods in Physics Research Section A: Accelerators, Spectrometers, Detectors and Associated Equipment*, 1033: 166662, 2022.

[88] J Sethi, R Palit, S Saha, and BS Naidu. Performance of a segmented planar ge detector and its coupling with the clover hpge detector. In *Proc. AIP Conf. Recent Trends in Nucl. Phys*, volume 1524, pages 287–291. American Institute of Physics, 2013.

[89] `https://www.gsi.de/en/work/research/experiment_electronics/data_processing/data_analysis/the_go4_home_page.htm`, 2023.

[90] `https://root.cern.ch/root/htmldoc/guides/users-guide/ROOTUsersGuideA4.pdf`, 2023.

[91] Michael Momayezi, William K Warburton, and Richard A Kroeger. Position resolution in a ge-strip detector. In *Hard X-Ray, Gamma-Ray, and Neutron Detector Physics*, volume 3768, pages 530–537. International Society for Optics and Photonics, 1999.

[92] PN Luke. Unipolar charge sensing with coplanar electrodes-application to semiconductor detectors. *IEEE Transactions on Nuclear Science*, 42(4): 207–213, 1995.

[93] N Goel, C Domingo-Pardo, T Habermann, F Ameil, T Engert, J Gerl, I Kojouharov, J Maruhn, N Pietralla, and H Schaffner. Characterisation of a symmetric agata detector using the γ-ray imaging scanning technique.

Nuclear Instruments and Methods in Physics Research Section A: Accelerators, Spectrometers, Detectors and Associated Equipment, 700:10–21, 2013.

[94] N Goel, C Domingo-Pardo, T Engert, J Gerl, I Kojouharov, and H Schaffner. Spatial calibration via imaging techniques of a novel scanning system for the pulse shape characterisation of position sensitive hpge detectors. *Nuclear Instruments and Methods in Physics Research Section A: Accelerators, Spectrometers, Detectors and Associated Equipment*, 652 (1):591–594, 2011.

[95] RA Kroeger, WN Johnson, JD Kurfess, BF Phlips, PN Luke, M Momayezi, and WK Warburton. Position sensitive germanium detectors for the advanced compton telescope. In *AIP Conference Proceedings*, volume 510, pages 794–798. American Institute of Physics, 2000.

[96] I Kojouharov, J Kojouharova, and J Gerl. Enclosure effects on the internal field distribution in hpge planar detectors. In *2006 IEEE Nuclear Science Symposium Conference Record*, volume 3, pages 1485–1488. IEEE, 2006.

[97] H Utsunomiya, H Akimune, K Osaka, T Kaihori, K Furutaka, and H Harada. Surface channel effect on γ-ray response functions of coaxial germanium detectors. *Nuclear Instruments and Methods in Physics Research Section A: Accelerators, Spectrometers, Detectors and Associated Equipment*, 548(3):455–463, 2005.

[98] `https://www.momentive.com/en-us/products/tds/rtv615?productId=64616a84-08ff-4372-a2a2-a58eb45be627`, 2023.

[99] `https://www.onsemi.com/download/data-sheet/pdf/microc-series-d.pdf`, 2023.

[100] `https://www.allaboutcircuits.com/electronic-components/datasheet/CLP-125-02-L-D--Samtec/`, 2023.

[101] Akashrup Banerjee, Michael Wiebusch, Marta Polettini, Andrew Mistry, Henning Heggen, Henning Schaffner, Helena M Albers, Nikolaus Kurz, Magda Górska, and Jürgen Gerl. Analog front-end for fpga-based readout electronics for scintillation detectors. *Nuclear Instruments and Methods in Physics Research Section A: Accelerators, Spectrometers, Detectors and Associated Equipment*, 1028:166357, 2022.

[102] Akashrup Banerjee, Marta Polettini, Henning Heggen, Henning Schaffner, Michael Wiebusch, Michael Traxler, Nikolaus Kurz, and Jürgen Gerl. Ultra short nuclear lifetimes measured with fast detectors and faster electronics. In *Hard X-Ray, Gamma-Ray, and Neutron Detector Physics XXII*, volume 11494, page 1149405. SPIE, 2020.

[103] `https://www.gsi.de/fileadmin/EE/EmbeddedSoftware/Manual_1._Exploder_and_Trigger_Module.pdf`, 2023.

[104] Veljko Radeka. Low-noise techniques in detectors. *Annual Review of Nuclear and Particle Science*, 38(1):217–277, 1988.

[105] L Mihailescu, W Gast, R.M Lieder, H Brands, and H Jäger. The influence of anisotropic electron drift velocity on the signal shapes of closed-end hpge detectors. *Nuclear Instruments and Methods in Physics Research Section A: Accelerators, Spectrometers, Detectors and Associated Equipment*, 447(3):350–360, 2000. ISSN 0168-9002. doi: https://doi.org/10.1016/S0168-9002(99)01286-3. URL `https://www.sciencedirect.com/science/article/pii/S0168900299012863`.

Nuclear Inst. and Methods in Physics Research, A 1051 (2023) 168233

Contents lists available at ScienceDirect

Nuclear Inst. and Methods in Physics Research, A

journal homepage: www.elsevier.com/locate/nima

Full Length Article

Performance test of a position sensitive planar germanium detector for phase-III DESPEC experiments

Arzoo Sharma [a,*], R. Palit [b,*], T. Habermann [c], J. Gerl [c], I. Kojouharov [c], H. Schaffner [c], P. Herrmann [c], H.J. Wollersheim [c], S. Saha [d], Biswajit Das [b], P. Dey [b], R. Donthi [b], B.S. Naidu [b], S. Mandal [e], Pushpendra P. Singh [a]

[a] Department of Physics, Indian Institute of Technology Ropar, Rupnagar 140 001, Punjab, India
[b] Department of Nuclear and Atomic Physics, Tata Institute of Fundamental Research, Mumbai 400 005, India
[c] GSI Helmholtzzentrum für Schwerionenforschung, Planckstrasse 1, 64291 Darmstadt, Germany
[d] School of Advance Sciences, VIT University, Vellore 632 014, India
[e] Department of Physics, North Campus, University of Delhi, Delhi 110 007, India

ARTICLE INFO

Keywords:
Double-sided strip detector
Position sensitive detector
Pulse shape analysis
Positron Annihilation Correlation
Coincidence method
Rise-time calculation

ABSTRACT

The position sensitivity of a planar segmented double-sided germanium strip detector, with 10 × 10 electrical segmentation in orthogonal directions, has been studied using the coincidence method. The coincidences were set up between an imaging scanner and the PSPGe (Position Sensitive Planar Germanium) detector using a positron source, ^{22}Na, and analyzed by employing the Positron Annihilation Correlation principle. A collimated ^{241}Am source scan was also performed to find position resolution along X and Y axes using low energy gamma-ray source. The primary objective of this work is to study the charge carrier transportation for gamma-ray interactions inside the PSPGe detector. In order to select the electrodes of interest and to obtain the pulse shapes for each event, two-dimensional images have been processed. The net charge induced on the surface of the electrode, calculated using the pulse shape analysis procedure, has been used to profile the position resolution and gamma interaction depth. The present study is an input for the deployment of PSPGe detector in the future decay spectroscopy experiments to be performed at the Facility for Antiproton and Ion Research (FAIR) in Germany. This work investigates the gamma interaction depth by calculating the rise-time of traces stored for each gamma interaction inside the detector volume, providing ≈1 mm resolution along the depth. The position resolution of the detector in lateral directions, determined using the amplitude difference of the transient charges, has also been found to be ≈1 mm.

1. Introduction

In recent years, enormous efforts have been devoted towards developing sophisticated solid-state Germanium detectors for gamma-spectroscopy experiments [1,2]. A crucial outbreak in the domain of gamma-spectroscopy has been achieved after the development of highly segmented Germanium detectors. The detector segmentation is an essential feature to determine interaction location using Pulse Shape Analysis (PSA) as it is sensitive to position.

The spatial characterization of such detectors is necessary to record the signals corresponding to each gamma interaction point inside the detector volume and to find its position [3,4]. The PSA method, based on the charge collection properties of the electrodes, has been used to achieve gamma interaction point and position resolution [5–7]. The charge carriers produced due to gamma interaction move under the influence of bias voltage applied to the electrodes, which induces a net charge on the electrode and an image/mirror charge on the adjacent electrode. W. Shockley and S. Ramo have discussed the method to evaluate these charges and induced current in Ref. [8,9]. It has been found that the spatial sensitivity of segmented detectors depends upon the effective charge collection at the two electrodes.

Recently, extensive efforts have been made to study the performance of a 25-fold segmented HPGe detector [10]. In addition to the PSA performance test, the efficiency and the peak-to-total ratio of the segmented HPGe detector have been also studied. AGATA (Advanced GAmma Tracking Array) [11], and GRETA (Gamma-Ray Energy Tracking Array) [12] are the 4π arrays of tapered hexagonal 36-fold segmented High Purity Germanium (HPGe) detectors arranged in a coaxial geometry. Both the arrays provide the possibility of gamma-ray tracking and Doppler shift correction due to the multi-fold segmentation of the encapsulated germanium crystal. A Segmented Inverted

* Corresponding authors.
E-mail addresses: 2017phz0005@iitrpr.ac.in (A. Sharma), palit@tifr.res.in (R. Palit).

https://doi.org/10.1016/j.nima.2023.168233
Received 25 December 2022; Received in revised form 13 March 2023; Accepted 21 March 2023
Available online 23 March 2023

coaxial GerMAnium (SIGMA) detector has been developed with better energy and position resolution [13]. SIGMA is an electrically segmented HPGe detector with point contact and electrode segmentation technology. For this detector, the grid search algorithm has been employed to find position resolution by considering a simulated pulse for a single interaction point with a random noise added to the pulse. The SIGMA detector has achieved a position resolution of 0.41 mm for 150 keV gamma energy. The position response of a 24-fold segmented coaxial germanium detector has been studied in Ref. [14]. They have reported position resolution of 3–7 mm, using the rise-time difference (for radial interaction study) and image charge magnitude difference at neighboring electrodes (for azimuthal location). In addition to the availability of highly segmented HPGe detectors, the domain of gamma [15] and beta [16] spectroscopy has marked a significant advancement with the R&D of planar segmented HPGe detectors. Such a planar detector has been proposed as an implant detector for performing the decay spectroscopy studies [17].

Following the developments, Khaplanov et al. [15] studied the effect of granularity on the position resolution of a planar HPGe detector. In this study, two different detector geometries, i.e., (a) pixelated detector with 16 pixels on one side, and (b) double-sided strip detector with eight strips in the orthogonal directions at opposite faces, have been used to determine the gamma interaction point. The PSA analysis has shown the benefit of using an orthogonal double-sided strip detector over the pixelated detector. It has been reported in Ref. [15] that the higher granularity of the detector is an asset to achieve better position resolution. Further, in a beta-decay spectroscopy experiment [16], a performance test of a planar orthogonal double-sided strip HPGe detector has been carried out, in which a 16-fold electrically segmented detector has been used as an implantation detector for radioactive isotopes. In Ref. [18], C.S. Lee et al. have studied the reconstruction of pulse shapes of planar p-type detector using Green's function based on induced charge effect. E. Ideguchi et al. have studied the response of 25-fold segmented planar germanium detector along the depth using Compton scattering coincidence method [19]. They have obtained ≈2 mm along the depth. Further, S. Shimoura has studied the position sensitivity of the segmented planar germanium detector, used in an array for the in-beam gamma-spectroscopy experiment, employing PSA technique [20]. E. Rintoul et al. [21] studied the charge collection property of planar double-sided strip detector through the collimated ^{241}Am source surface scan and ^{137}Cs source side scan, and obtained good energy and position resolution using the PSA technique.

In the present work, the position resolution and depth of gamma-ray interaction have been studied for one of the planar segmented HPGe detectors, which shall be employed in the future DESPEC experiments at the Facility for Antiproton and Ion Research (FAIR) in Germany. This article is organized as follows. In Section 2, the experimental setup and methodology, including detector design and scanning setup, are discussed. In order to find the position resolution of the PSPGe detector, two sets of measurements have been performed using the coincidence technique and independent collimated source scan. The analysis procedure adopted to determine the depth of gamma interaction and calculate the position resolution along the lateral faces of the detector is discussed in Section 3. The results obtained from the present analysis and their interpretations are discussed in Section 4, followed by a summary.

2. Experimental setup and methodology

The characterization of a Position-Sensitive Planar Germanium (PSPGe) detector has been carried out at GSI Germany using a scanning setup developed to characterize highly segmented germanium detectors. The GSI scanning system [22,23], which consists of a Position Sensitive Detector (PSD), was deployed in coincidence with the PSPGe detector using a positron source. This technique is helpful to select the pulses corresponding to the correlated gamma interaction event in both the detectors within a time window. A detailed description of the PSPGe detector and the experimental setup is given in the following section.

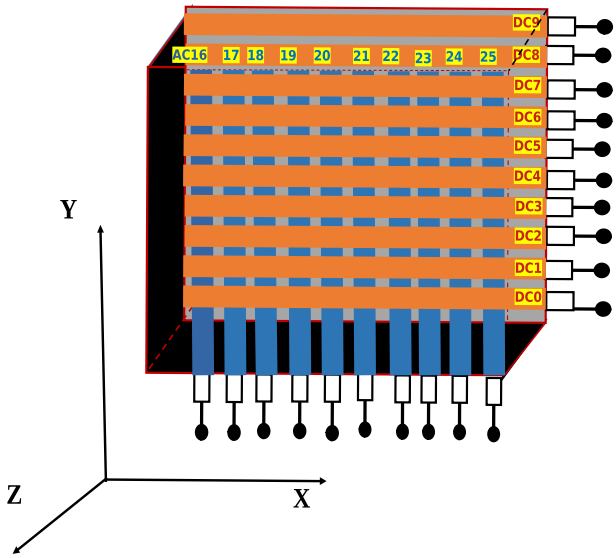

Fig. 1. Layout of planar orthogonal double-sided strip detector. The horizontal and vertical strips are indicated by orange and blue rectangles, respectively.

2.1. Detector description

The p-type Planar Position Sensitive HPGe detector, produced by Mirion Technologies (former CANBERRA EURISYS), is a double-sided orthogonal strip detector that comprises 10 strips per each side in horizontal and vertical directions. One of the contacts is produced by boron implantation and is DC connected to the preamplifiers and the other contact is a proprietary Mirion technology and has AC connection to the preamplifiers. The segmentation is only electrical one and is done by etching a certain pattern, thus producing the strips. According the information of the producer, two guard rings, surrounding the strips at every side, are employed. It is important to mention that the guard rings have a planar structure — practically 2D instead a simple grove. The primary goal of them is to reduce the leakage current though the strips which improves the energy resolution. The segmentation of the detector is an essential feature to find the location of gamma interaction by storing pulse shapes for each segment on an event-by-event basis. The physical dimensions of the detector are 6 cm × 6 cm × 2 cm with a thin Aluminium window of thickness 0.5 mm. The layout of the detector segmentation is shown in Fig. 1, displaying ten segmentations along the horizontal X (DC connected) and vertical Y-axis (AC connected). The segmentation makes the detector position-sensitive for the interaction of incoming photons in a voxel of dimensions 6 mm × 6 mm × 2 cm. The operating bias voltage of the detector at full depletion is −1900 V. The complete detector description is given in the Ref. [24].

2.2. Collimated source scanning

A ^{241}Am source scanning was performed at steps of 1 mm using lead collimator with hole of diameter 1 mm. It is a low energy source with 59.5 keV gamma-line, used to determine surface effects in the crystal. The half-value thickness of 59.5 keV in germanium crystal is 0.6 mm calculated using NIST - XCOM database [25]. Hence, the scan was performed on both the sides, i.e., one side with AC strips and other with DC strips. The detector to source distance was kept at 2 mm. The two scans were performed for one of the middle strip and a side strip. The vertical strips (AC21 and AC16) and the horizontal strips (DC4 and DC8), were scanned at the center along their width. The activity of ^{241}Am source was approximately 44 kBq. The electronics readout was created using OR of all the channels of PSPGe using the SIS3316 digitizer [26]. The SIS3316 digitizer had 32 readouts, out of which 20

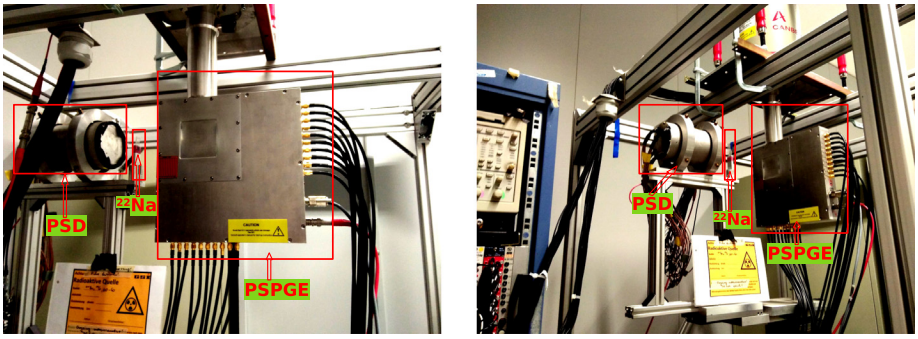

(a) (b)

Fig. 2. Coincidence setup for PSD and PSPGe at an angle (a) 0° for Set-A, and (b) 90° for Set-B measurements. The detector system and the source are marked inside the rectangular regions for clarity.

channels were used for the PSPGe detector readout. PSPGe data were recorded whenever at least one segment had a signal above the trigger threshold. The typical trigger rate was 300 Hz. In the first step, the center of the strip (to be scanned) was located by moving the source to get the maximum counts in the photopeak and later, it was moved to either direction covering three positions in the left and three in the right at steps of 1 mm (covering the approximate size of the strip).

2.3. Scanning setup

The scanning setup consists of a PSD comprising of Cerium doped Lutetium Yttrium OrthoSilicate (LYSO) scintillation crystal coupled to a Position-Sensitive Photo-Multiplier Tube (PSPMT). The PSPMT has a mesh of 16 X and 16 Y anodes. In the scanning setup, the detector and positron source ^{22}Na are mounted on an aluminum frame at an optimized distance of 5 cm [27]. The scanner has a spatial resolution of the order of 1 mm. In the present work, the PSPGe detector was set up in coincidence with a properly characterized PSD using the ^{22}Na source of approximate activity 169 kBq. The experiment was performed for PSD at an angle 0°, as shown in Fig. 2(a) (Set-A), and rotating PSD at an angle 90°, shown in Fig. 2(b) (Set-B). The positron source emits two 511 keV gamma-rays in opposite directions after the process of pair annihilation. This figure shows that both gamma-rays are collected in the two opposite-facing detectors. The charge collected in PSD is used to obtain 2-Dimensional (2-D) image from the coincidence data.

The PSPGe was irradiated with 511 keV gamma-rays obtained from the standard source, selected via its coincidence with the PSD. The half-value thickness of 511 keV in germanium crystal is approximately 1.5 cm calculated using NIST - XCOM database [25]. The source to PSPGe detector distance was 8.6 cm for Set-A and 14.4 cm for Set-B measurements. It may be noted that the source-detector distances were optimized for covering a whole solid angle around the PSPGe detector. The optimization was made by looking at the ONLINE 2-D images obtained from the PSD using GSI Object Oriented On-line Off-line (GO4) data collection package [28]. The PSD and PSPGe were setup in coincidence using the timing information from PSD and OR output of all the channels in PSPGe, obtained from the SIS3316 digitizer. The coincidence output was then used as a readout trigger for QDC (PSD) and SIS3316 digitizer (PSPGe) with a trigger rate of 250 Hz. The QDC had 32 channel readout for all 16X + 16Y anodes from PSD. The data was collected using the Multi Branching System data acquisition (MBS - DAQ) and GO4 for online monitoring. The detailed electronics setup has been discussed elsewhere [29].

3. Data collection and analysis

The data was collected for approximately two days for Set-A and Set-B positions (≈2 TB of data), and half an hour for each scanned position in ^{241}Am source scan (≈1.5 TB of data) using MBS. The offline data analysis was performed using GO4 and C++ based ROOT platform [30]. The position resolution of the PSPGe detector has been determined by analyzing pulse shapes at various gamma interaction points inside the detector. As shown in Fig. 1, the detector is segmented along the horizontal and vertical directions, but not along the depth. Despite this, the position resolution measurements for three coordinates can be extracted independently. In order to find the depth of gamma-ray interaction, a method of small pixel effect has been employed [31]. The depth has been estimated using the rise-time difference between the two opposite surfaces of the double-sided strip detector. For finding position resolution along the lateral faces, (X and Y-axis) the amplitude ratio of the image charge carriers in the neighboring segments is calculated as given in Refs. [32,33].

Table 1
Full Width at Half Maxima (FWHM) obtained for one near edge and one middle strip along AC as well as DC sides.

Source	E (keV)	FWHM DC4 (keV)	FWHM DC8 (keV)	FWHM AC17 (keV)	FWHM AC21 (keV)
^{241}Am	26.3	0.91	0.89	1.28	1.40
^{241}Am	59.5	0.98	0.96	1.29	1.59
^{60}Co	1332.5	2.68	2.54	2.29	2.36

3.1. Key procedures

- The energy resolution of the detector has been studied using ^{241}Am and ^{60}Co. For typical energy resolution of the strips, see Table 1.
- Further, the analysis has been performed to reconstruct the 2-D image from the PSD using the centroid fitting approach. It has been attained through charge collected at X and Y anodes in PSD using QDC. The 2-D images obtained from this analysis are given in Fig. 3(a) (for Set-A) and 3(b) (for Set-B) representing the depth and the lateral view of the detector, respectively.
- The energy spectrum derived from the SIS3316 digitizer has been used to select the electrode of interest for further analysis through gating on the Photopeak after calibration.
- For Set-A measurements, the 2-D image is projected onto the *X*-axis for dividing the axis, as the PSPGe detector is not segmented in depth.
- For Set-B, the strip is further divided using the 2-D image to get better position resolution than the segmentation itself. In addition, ^{241}Am collimated source scan data has been analyzed to find the position resolution using 59.5 kev gamma-ray photopeak. The two source measurements (^{22}Na and ^{241}Am) are independent.
- The 2-D image is projected onto the respective axis to obtain the calibration. The calibration of the projected image is performed

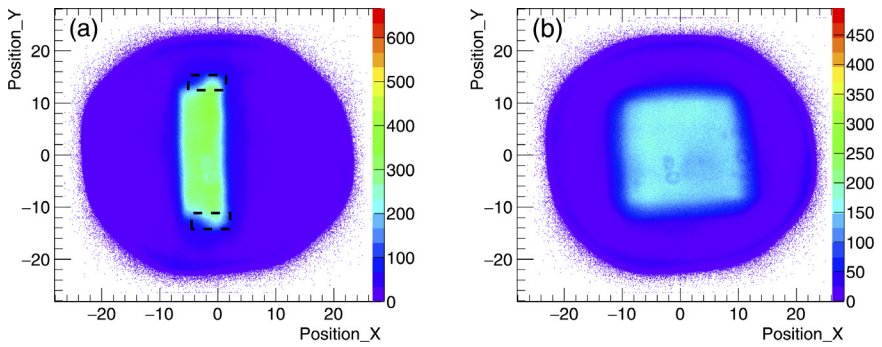

Fig. 3. 2-D images obtained from PSD for (a) Set-A and, (b) Set-B measurements using centroid method for coincidence setup. The black dotted rectangular regions at the top and bottom of the image in (a) represent the guard ring on AC side (discussed in Section 4).

following the known dimensions of the PSPGe detector. In Set-A, Position_X in PSD image (Fig. 3(a)) represents the depth of the PSPGe detector (shown by Z-axis in Fig. 1).[1] In Set-B, Position_X represents the X-axis of the PSPGe detector. The Position_Y indicates the Y-axis in both sets of measurements.

- The traces obtained from the digitizer SIS3316 are further processed as quantified in the literature [34], i.e., performing baseline subtraction, normalization, and finally, the time aligning of the traces.
- Traces have been time-aligned at 10% of the final amplitude.

3.2. Depth of gamma interaction

The Set-A measurements, performed with PSD at 0°, have been used to calculate gamma interaction depth. It implies that the PSD has been facing the crystal depth as displayed in Fig. 2(a). It may be pointed out that the position sensitivity and fast imaging capabilities of PSD help to accomplish the experimental goals solely through one measurement [35]. The 2-D image from PSD is projected on to X-axis and is sub-divided into fifteen regions for calibration since there is no segmentation along the detector's depth. The DC and AC strips have been numbered from 0 to 9 and 16 to 25, respectively, as represented in Fig. 1. In this work, the analysis has been performed for one middle DC–AC strip and one side DC–AC strip pairs, referred to as DC4 - AC20, and DC0 - AC16 respectively.

The gate on energy helps to understand the response of the detector for the gamma-ray of interest. The energy information obtained from the SIS3316 digitizer has been used to make an energy cut on the 511 keV photopeak to select DC4 and AC20, DC0 and AC16 electrodes. Single interactions in one AC/DC strip combination has been required to avoid ambiguities from multiple interaction points in the detector. Further, the traces obtained from the energy cut have been studied for each of the fifteen cuts on the 2-D image. The acquired trace information has been used to find the rise-time for AC and DC electrodes after processing digitizer pulses for each interaction event in these cuts. The rise-time difference of pulses has been calculated between the front and the back faces to get the depth of the gamma interaction point, which is useful due to the difference in mobility of electrons and holes, implying separate charge collection of the two charge carriers at the respective electrodes. Therefore, the difference in mobility leads to different rise-time values [31,36]. The T50 rise-time has been calculated for the time-aligned traces in the present analysis. It is defined as the time required for the pulse to reach 50% of the maximum amplitude minus the time required to reach 10% of the maximum amplitude. The average rise-time has been calculated for each of the fifteen cuts and plotted as a function of the depth. The

[1] The depth represents Z-axis in the PSPGe detector. The 2-D image from set-A measurement (depth scan) has DC segments on the left side and AC segments on the right side of the central densely populated detector image.

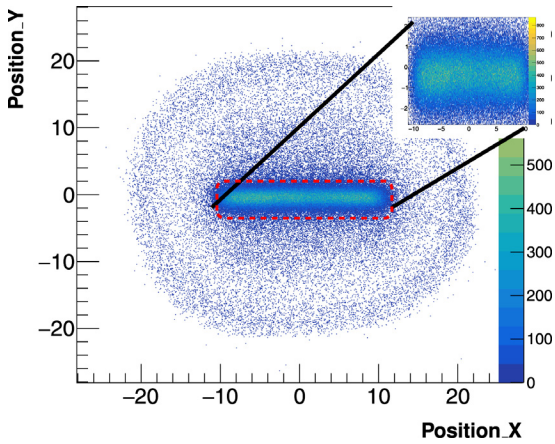

Fig. 4. 2-D Image obtained from PSD for Set-B gated on horizontal electrode, DC4. The image on the top of this image is the zoomed one on rectangular portion marked with red dashed lines in the center. It has been marked as one of the representative cases to show the boundaries of the electrode selected.

T50 rise-time difference has been calculated between AC20 and DC4, i.e., $T50_{AC20} - T50_{DC4}$, and between AC16 and DC0. i.e., $T50_{AC16} - T50_{DC0}$. T50 rise-time values were chosen for the analysis as it provided more sensitivity in depth as compared T30 (time required for the pulse to reach 30% of the maximum amplitude minus the time required to reach 10% of the maximum amplitude) and T90 (time required for the pulse to reach 90% of the maximum amplitude minus the time required to reach 10% of the maximum amplitude). The analysis of the results for AC and DC electrodes' behavior along the depth is discussed analytically in Section 4 using χ^2 comparison and rise-time difference.

3.3. Lateral position resolution

The measurements have been carried out to find the position resolution of the detector along the X and Y directions. Fig. 2(b) shows the set-B measurements, in which PSD is positioned at an angle of 90°. The analysis procedure remains the same for processing the trace of the selected strips in the data set. As a representative case, the 2-D image for the 511 keV photopeak on strip DC4 is given in Fig. 4.

The 2-D image for the selected strip (the red dashed rectangular region in the Fig. 4 is projected onto the Y-axis for DC4 (and for vertical strip, the selected 2-D image is projected on to the X-axis). This analysis has been performed for DC4 and AC21 segments. The selected segment is sub-divided into seven positions using the projections, where the position difference between each division is considered to be 1 mm, as the strip thickness is ≈6 mm. The transient charges in the adjacent segments have been analyzed for each position. The applied bias does not affect the induced charge on the electrode produced due to the

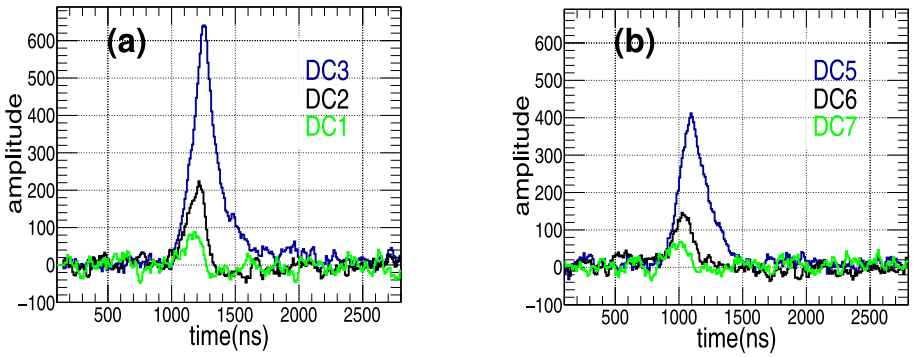

Fig. 5. Event in DC4, and the corresponding amplitudes of transient charges in the neighboring strips (a) below, and (b) above DC4.

moving charges as it depends on the instantaneous electric field at each point of its path [37]. For the strip semiconductor detector, the amplitude of the induced charge on an electrode would be lower if it is farther away as compared to the pitch of the electrode. The most pronounced weighting potential would be near the electrode surface. In the case of an orthogonal strip detector, the electrons and holes are collected at anode and cathode surfaces, respectively.

The image charges are shown in Fig. 5, where one of the fired DC segment is selected, DC4. The corresponding image charges in the neighboring segments are shown in Fig. 5(a)–(b). As indicated in the figure, the closest neighboring segments, DC3 and DC5 are represented in blue. The next neighbors, DC2 and DC6, are shown in black, followed by DC1 and DC7 segments in green color. Due to the maximum amplitude of the mirror charge in DC3, it may be inferred that the interaction occurred close to the lower edge of DC4. Moreover, it has been observed that corresponding to the moving charge created in DC4, the charge is induced on the far neighbors along with nearest adjacent segments. The amplitude of the induced charge depends on the electrode's hit location, along with the amount of energy deposited by the incoming gamma-ray. The analysis has been further progressed in two steps. First, the 2-D image was constructed for 511 keV photopeak on both DC4 and AC21 segments, i.e., by selecting the events in which both the strips fire together and eventually, obtaining a corresponding voxel (with dimension of ≈6 mm X 6 mm X 2 cm). As a next step, the projection of the 2-D image is further divided into seven regions. As an example for two middle strips, the image has been reproduced showing amplitude of image charges in the neighborhood strips, given in Fig. 6. In these figures, the central part represents interaction event with two middle strips (DC4 and AC20) firing at the same time, where DC4 is represented by red color and AC20 by black color. The corresponding image charges of the two strips are shown in blue color. The left and right image charges correspond to AC19 and AC21 electrodes. The top and bottom image charges represent the induced charge in DC5 and DC3, respectively. As shown in Fig. 6(a), AC20 has faster rise-time as compared to DC4. The T50 rise-time difference is found to be −40 ns. The 2-D image cut is −1.9 < Position_X < −1.5 and 0.5 < Position_Y < 1 (corresponds to upper left part of voxel). For this specific location, it has been found that the polarity of image charges in the neighborhood of AC20 is negative, while the DC4 has positive image charges. The amplitude of image charges in the AC19 and DC5 segments are high, indicating interaction occurred in the vicinity of these segments. Further, for an event shown in Fig. 6(b), DC4 has shorter rise-time than AC20 segment. A T50 rise-time difference of 140 ns has been obtained. The 2-D image cut is −0.5 < Position_X < 0 and 0.5 < Position_Y < 1, i.e., the upper right voxel. As indicated in the figure, the polarity of image charges in the neighborhood of DC4 is negative, and the polarity of image charges in AC19 and AC21 segments is positive. The amplitude of the image charges in DC5 and AC21 is more pronounced than in the DC3 and AC19 segments.

This implies that the time difference between the two segments for the defined interaction locations in Fig. 6(a)–(b) affects the polarity of the image charges. Hence, the interaction location affects the amplitude of the image charges. Therefore, it may be concluded from Figs. 5 and 6 that the ratio of the amplitudes in the adjacent of the hit segment can be employed to find the position resolution. It is further pointed out that for all interaction voxels, the gamma-ray interaction depth may differ. Moreover, based upon different gamma interaction depths, the polarity of image charges will differ.[2]

Additionally, for independent ^{241}Am collimated source scan, the image charges amplitude study has been performed by gating on the 59.5 keV photopeak. Because of the lower penetration depth of 59.5 keV gamma-rays in germanium, the image charges have been obtained with negative polarity. It indicates the specific rise time difference between the horizontal and vertical strips. For the AC segment scan, centroid of the T50 rise-time difference distribution plot for each measurement position between DC5 and AC21 obtained is ≈5 (± 0.5) ns. For the DC scan, the T50 rise-time difference between DC4 and AC21, it is ≈140 (± 1.5) ns. The amplitudes of the image charges in the neighborhood of the scanned segment have been analyzed and are discussed in Section 4.

4. Results and discussion

The segmentation of the PSPGe detector along the X and Y-axis makes it position-sensitive for the gamma-ray hit. The higher degree of segmentation helps to record each event in a different segment. The coincidence technique has been employed to characterize the PSPGe detector. In Fig. 3(a), the guard ring is observed, represented by black dotted rectangular region, which accounts for the homogeneous charge collection at the electrodes. The presence of only one guard ring despite the information of the producer for two guard rings may be attributed to the electric field distribution build on 2D structures. It may be noted that the presence of the guard ring does not prevent the trapping of the charge carriers at the open surface of the detector. Then, the surface charge there creates a "field defect" [38,39] – an area with a specific fringe field which diverts the charge carriers towards the open surface of the detector thus eliminating them from the charge collection and pulse generation. The more counts in the central region in the 2-D reconstructed images describe the active volume of the detector crystal. The calibration is performed through the known dimensions of PSPGe.

The pulse shape comparison scan has been performed for pulses along the 0°and 90°scans using χ^2 minimization to understand the depth of gamma-ray interaction. The χ^2 has been performed between a strip along the 0°(set-A) scan and the same strip along the 90°(set-B)

[2] Further to note, the 2-D set-B measurement was performed for both orthogonal sides, i.e. one side with vertical strips (AC segments) and the other side with horizontal strips (DC segments). For vertical strip scan, AC21 segment has been analyzed for position resolution measurement. For horizontal strip scan, DC4 segment has been analyzed for position resolution measurement.

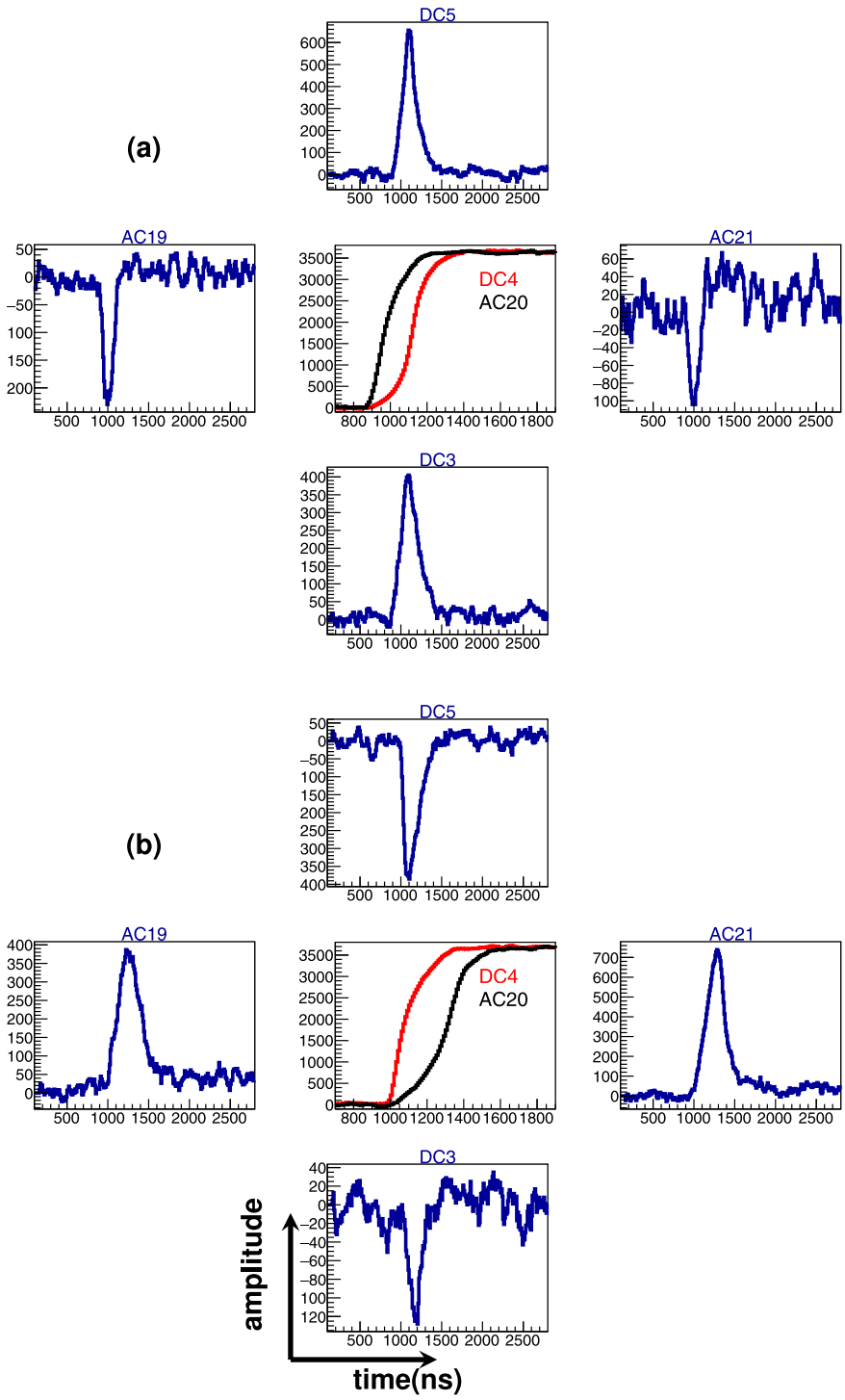

Fig. 6. Image Charges obtained by gating on 2-D PSD spectrum (for set-B measurement) in the voxel with 2-D cut given by (a) −1.9 < Position_X < −1.5 and 0.5 < Position_Y < 1 (b) −0.5 < Position_X < 0 and 0.5 < Position_Y < 1.

scan. The pulses at different positions were selected along the depth (using 2-D image from the PSD) and were compared to pulses in a single cut in the 90°(representing front side of detector) scan [27]. The formula used for χ^2 calculation for matrix with i pulses in one scan and j pulses in the other scan is given as following:

$$\chi^2_{i,j} = \frac{\sum_{k=k_0}^{k_{max}} (Pulse_0[i,k] - Pulse_{90}[j,k])^2}{k_{max} - k_0} \quad (1)$$

where k represents sample number of the pulse which corresponds to time (with a sampling time of 10 ns). k_0 represents initial sample number where the pulses have been time aligned. k_{max} denotes the sample number with maximum pulse amplitude. $k_{max} - k_0$ corresponds to the slope of the pulse, i.e., when charge carriers are moving between the opposite electrodes. $Pulse_0$ and $Pulse_{90}$ represents pulse in the 0°and 90°scans, respectively. After comparison or χ^2 calculation, the mean of the pulses was taken for specific χ^2 range or minimum value of χ^2.

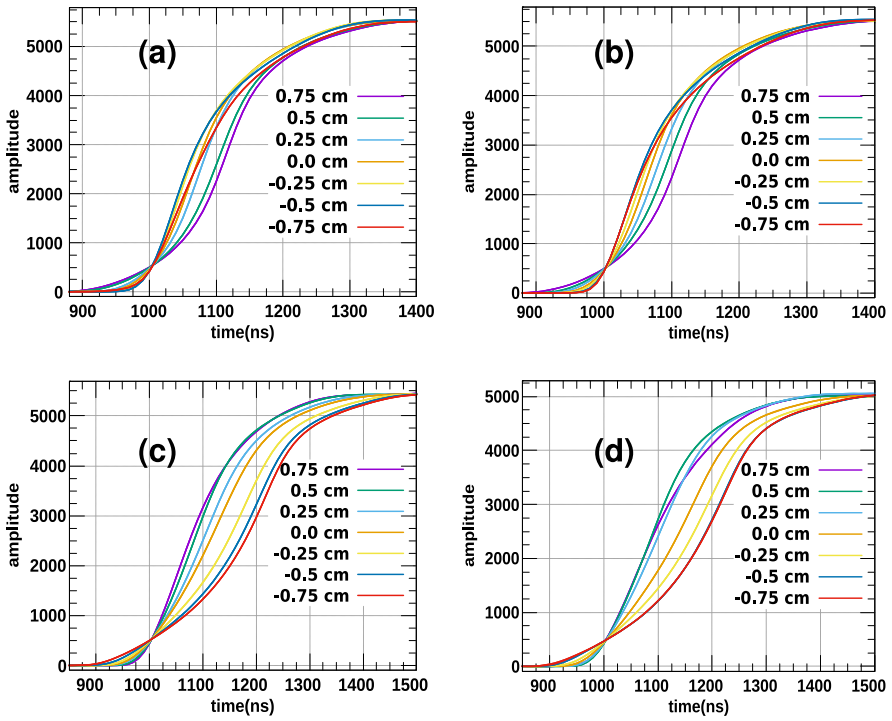

Fig. 7. (a) Mean pulse obtained after pulse shape comparison using χ^2 minimization for strip (a) DC0 (b) DC4 (c) AC16 (d) AC20. The legend represents different depth cuts in the 0°scan/set-A 2D image (depth dimension is 2 cm).

The mean pulse was then plotted for different depth cuts. The analysis has been shown for DC0, DC4, AC16, and AC20 strips, compared along the two sets of scans. The compared pulses consisted of a matrix of ≈30 000 pulses. The mean pulses plotted are in Fig. 7. The pulse shape comparison helps to understand the interaction location of gamma-ray inside the detector. The mean pulse calculated at various depths have different shapes. This behavior is attributed to the difference of the electrons and holes charge collection when moving towards the respective electrodes. From Fig. 7(a)–(b), it is concluded that for the DC segments, the rise-time of the pulse increases with increasing depth. While the rise-time decreases for AC segments with the increasing depth, shown in 7(c)–(d). The results are consistent for the middle and edge strips. This method helps to validate the sensitivity of scanning device to find the gamma-ray interaction depth in the PSPGe detector (for coincidence between scanner and PSPGe) using χ^2 minimization method for set of pulses in orthogonal scanned positions.

Further, in order to position resolution along the depth, the rise-time T50 has been calculated for traces obtained from the SIS3316 digitizer. The rise-time difference has been calculated between two middle strips (DC4 and AC20) and two edge strips (DC0 and AC16) by selected segment using 511 keV energy cut. The T50 rise-time difference has been calculated for both the strip pairs, for each of the fifteen cuts, in the 2-D image.

The T50 rise-time time difference between AC16 - DC0, and AC20 - DC4 is plotted as a function of the interaction depth in Fig. 8(a) and (b), respectively. The centroid of the difference in the rise-time distribution has been plotted as a function of hit location. A Gaussian fit has been performed for each set of T50 rise-time difference values distribution. The error in each data point represents the uncertainty in centroid after the fit. The rise-time difference between the two electrodes can help to identify the interaction location as the trace would be different for each interaction point for both types of electrode but within the position resolution of the detector, as indicated also from χ^2 analysis. The higher values of the time difference between the two electrodes describe that the interaction location is closer to the DC electrode or, vis-à-vis, far from the AC segment. The holes travel longer than the electrons to reach the AC electrode. This trend remains almost constant for the interaction depths at the boundaries of the detector. It becomes challenging to locate the exact point of gamma interaction in this depth region. However, in the middle/active region, the time difference shows a linearly decaying pattern. The decrease in time difference happens because of the relatively fast charge collection at the AC segment with an increase in depth. For AC20 - DC4, the T50 rise-time difference values vary from ≈130 to −40 ns at the extreme ends, and for AC16 - DC0, the range is 110 to −20 ns. Hence, the difference in T50 rise-time between the two orthogonal strips helps to estimate the interaction depth independent of X and Y coordinates. The linear fit has been performed for the values of depth ranging from −0.4 to 0.7 cm. The slope of the fit was further used to obtain position difference (dX or dY) for pairs of all points and the corresponding error was calculated through error propagation. It has been used to calculate weighted mean to find the position resolution.

The position resolution obtained from Fig. 8(a) and (b) is 1.2 ± 0.09 mm, and 1.2 ± 0.14 mm, respectively.

In order to determine the position resolution along the X and Y-axis, the Set-B coincidence setup has been utilized. As discussed in the analysis procedure for finding the lateral position resolution, the amplitude ratio is calculated for each induced charge in the neighboring segments. The amplitude ratio between the image charges estimates how close the two interactions could be resolved. The minimum resolving would correspond to the thickness of the segment itself, as there would always be a pulse generated corresponding to an event in a specific segment. The axis of the projected 2-D image is calibrated according to the dimensions of the strip, i.e., 6 mm. For each interaction location, the amplitudes of the induced charges in the neighboring segment have been studied. In the present work, the difference in amplitude ratios has been calculated by the asymmetry parameter a_amp which is defined as,

$$a\_amp = \frac{A1 - A3}{A1 + A3} \tag{2}$$

where A1 and A3 correspond to the amplitude of image charges in strip 1 and strip 3 for interaction in strip 2 and A3 < A1. In the present analysis, a_amp has been calculated for the interaction in DC4

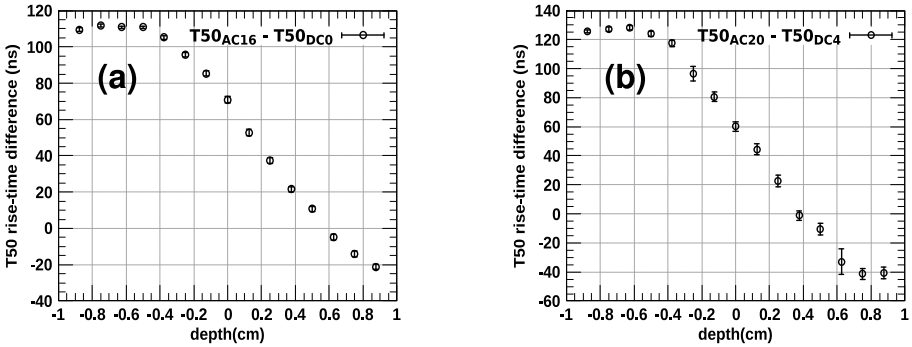

Fig. 8. (a) Plot of T50 rise-time difference between (a) AC16 - DC0 pair (at the detector edge) (b) AC20 - DC4 pair (middle strips) plotted as a function of depth.

and AC21 electrodes. For an event in the DC4 segment, the amplitude of image charges in the neighborhood of DC4 has been calculated. A3 and A5 represent the amplitudes of image charges in DC3 and DC5 segments, respectively. Similarly, A20 and A22 represent the amplitudes of images charges in AC20 and AC22 strips, respectively, for a gamma-ray interaction in the AC21 electrode. The special note is that the a_amp has been calculated for specific depth obtained by calculating rise-time difference between the segment and one of the orthogonal segment for both the data sets of scans (as mentioned in footnote[2]). For DC4 scan, rise-time difference is calculated between AC21 and DC4 ($T50_{AC21}$ - $T50_{DC4}$). For AC21 scan, rise-time difference is calculated between AC21 and DC5 ($T50_{AC21}$ - $T50_{DC5}$). The values of the obtained rise-time difference have been tabulated in Table 2 for both horizontal and vertical strip scanned data. For each of the seven cuts, a_amp is obtained using centroid from the Gaussian fit to the distribution plot and error is obtained from the error in the centroid value. The a_amp has been plotted as a function of respective axis Y (for DC4 hit segment) and X (for AC21 hit segment) as shown in Fig. 9(a) and (b), respectively. As we move along the axis, the amplitude of left neighborhood image charge decreases while the right image charge amplitude increases. Therefore, we obtain linear decay line with negative slope. The linear fit is performed to the data to obtain slope. The weighted mean is calculated to determine position resolution. The position resolution obtained has been tabulated in Table 2.

Additionally, the analysis has been performed for position resolution calculation for collimated ^{241}Am source scan. The resolution has been studied using 59.5 keV photopeak selection for the scanned electrodes DC4, DC8, AC17, AC21. The corresponding neighborhood image charges are stored for each hit electrode. The scan was performed for 7 data points starting from the middle of the electrode and moving collimated source in steps of 1 mm in each direction.[3] The similar analysis is performed to calculate the a_amp values from the distribution plot for each measurement position and then plotting a_amp as the function of respective axis, shown in Fig. 10. The linear fit is performed to obtain the slope and further calculating position resolution. The resolution measurements are tabulated in Table 2 for different measurements.

From the analysis, it is inferred that the resolution along the X and Y axes for both the ^{241}Am and ^{22}Na scans, is of the order of ≈1 mm. The error bars differ in the two cases because of precise collimation source measurement using ^{241}Am. It has low energy gamma-ray with low attenuation depth as compared to ^{22}Na, leading to more accuracy due to surface scanning. Using ^{241}Am independent source scan, it is also concluded that the resolution is consistent along the center and edge of the detector (from Table 2).

[3] The position axis in the ^{241}Am source scan shown in Fig. 10 is different from the axis in the coincidence setup set-B analysis shown in Fig. 9 as the later is calculated from the 2-D image projection while the former is from the real moving source positions.

Table 2
Lateral position resolution using two scan methods, i.e., coincidence scan using ^{22}Na source and ^{241}Am scan. For horizontal (DC) and vertical (AC) segment scans, the resolution has been calculated along Y and X-axis, respectively, mentioned in column 2. The neighboring or adjacent segment (to left and right of the scanned/hit segment) are given in column 4. Orthogonal strip w.r.t. which the rise-time difference (accounting for the depth of gamma-ray interaction) is provided in column 5 and the corresponding rise-time values in column 6. The resolution obtained is given in column 7.

Source scan	Scanned axis	Scanned strip No.	Neighboring strip No.	Orthogonal strip No.	T50 rise-time difference (ns)	Position resolution (mm)
^{241}Am	Y	DC4	DC3, DC5	AC21	140	1.0 ± 0.04
^{241}Am	Y	DC8	DC7, DC9	AC21	75	1.1 ± 0.05
^{241}Am	X	AC17	AC16, AC18	DC5	−20	1.2 ± 0.05
^{241}Am	X	AC21	AC20, AC22	DC5	5	1.1 ± 0.04
^{22}Na	Y	DC4	DC3, DC5	AC21	59.5	0.9 ± 0.25
^{22}Na	X	AC21	AC20, AC22	DC5	59.5	0.9 ± 0.27

Therefore, it is concluded that the a_amp and/or amplitude ratio between the image charges adjacent to the hit segment provides gamma-ray hit location along the X and Y-axis. The polarity of the image charges will depend upon the instantaneous electric field generated by the moving charge in the hit segment and the interaction depth.

Therefore, the present analysis shows an appreciable difference in amplitudes for an event near the edges of the strip. This analysis provides a confidence limit of position resolution to be approximately 1 mm for both the X and Y-axis. In this manner, the amplitude difference in the neighboring segments of the hit segment has been used to find the position resolution inside the detector along the X and Y-axis. Hence, with this good position resolution makes the detector suitable to be used for the upcoming DESPEC campaigns.

5. Summary

In summary, it is inferred based on the present performance test that the Position Sensitive Planar Germanium (PSPGe) detectors are potential candidates for future gamma spectroscopy experiments. In this work, the response of the PSPGe detector is studied using the coincidence technique, along with independent collimated source measurement. The analysis is performed to select electrode of interest (middle and edge) in horizontal and vertical directions using energy gate. For resolution along the Z-axis (depth of the PSPGe detector), the 2-D image obtained using the coincidence setup has been used to divide the axis in depth as it is not segmented. The χ^2 comparison has been performed between the 0°and 90°coincidence scan using scanning setup for different depths. The mean pulse obtained for different depths provide also information on the depth of interaction. More precisely this has been studied using the rise-time difference between the two opposite surfaces as a function of depth for middle and side strips. An appreciable rise-time difference has been obtained at various depth locations with position resolution of the order of ≈1.3 mm, consistent at the borders of the detector. In order to achieve position resolution

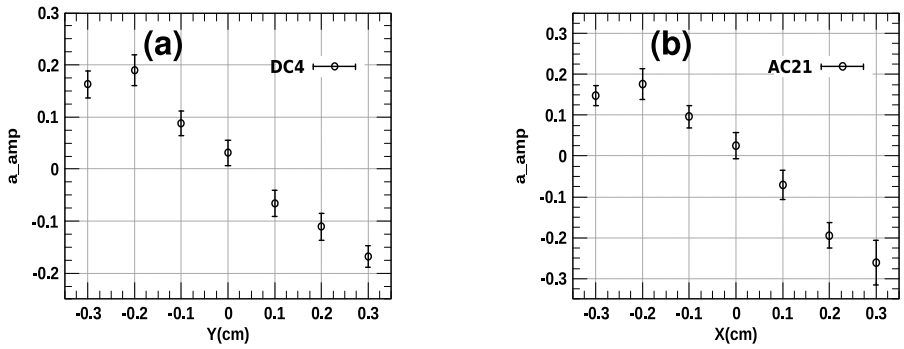

Fig. 9. a_amp parameter calculation for comparison of image charges in neighborhood of (a) DC4 and (b) AC21 for coincidence setup using ^{22}Na source.

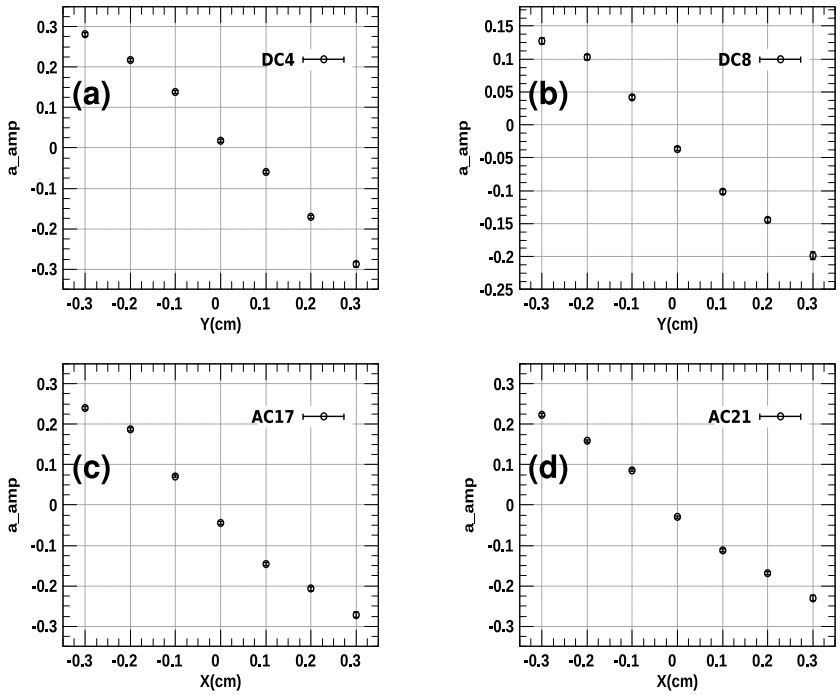

Fig. 10. a_amp parameter calculation for comparison of image charges in neighborhood of (a) DC4 and (b) DC8 (c) AC17 (d) AC21 using independent collimated ^{241}Am source scan.

better than 6 mm (the size of the segment itself), the strip has also been divided using the 2-D image projection cut along both X and Y directions from the coincidence ^{22}Na source scan data. The position resolution along the horizontal and vertical directions is measured using the difference in amplitudes of the image charges in the neighborhood of the selected hit segment. The measured amplitude difference is considered to account for the gamma hit location. The analysis for the front crystal scan (providing X and Y resolution) has also been performed using collimated ^{241}Am. The obtained position resolution along X and Y axes using both the scans is around 1.1 mm. The present investigation provides a valuable input towards designing of gamma-spectrometer for phase-III DESPEC experiments at FAIR.

Declaration of competing interest

The authors declare that they have no known competing financial interests or personal relationships that could have appeared to influence the work reported in this paper.

Data availability

Data will be made available on request.

Acknowledgments

This work is partially supported by the Department of Atomic Energy, Government of India, under project No. 12P-R&D-TFR-5.02-0400. The authors would like to acknowledge the Helmholtz International Center for FAIR/GET_IN-volved in Germany. The authors acknowledge Pascal Quirin, Michael Ginsz, and their complete team at MIRION Technologies for comprehensive discussion and cooperation. The authors acknowledge all the support and motivation by Prof. M. Górska. One of the authors, A. S. acknowledges A. Banerjee and T. Arici for their support and discussions during the experiments. A.S. especially acknowledges G. Aggez for her valuable feedback on experimental setup. Most importantly, A.S. acknowledges all the group members at GSI for quick help and suggestions.

References

[1] M. Górska, M. Lipoglavšek, H. Grawe, J. Nyberg, A. Ataç, A. Axelsson, R. Bark, J. Blomqvist, J. Cederkäll, B. Cederwall, G. de Angelis, C. Fahlander, A. Johnson, S. Leoni, A. Likar, M. Matiuzzi, S. Mitarai, L.-O. Norlin, M. Palacz, J. Persson, H.A. Roth, R. Schubart, D. Seweryniak, T. Shizuma, Ö. Skeppstedt, G. Sletten, W.B. Walters, M. Weiszflog, $^{98}_{48}Cd_{50}$: The two-proton-hole spectrum in $^{100}_{50}Sn_{50}$, Phys. Rev. Lett. 79 (1997) 2415–2418.

[2] C. Vaman, C. Andreoiu, D. Bazin, A. Becerril, B.A. Brown, C.M. Campbell, A. Chester, J.M. Cook, D.C. Dinca, A. Gade, D. Galaviz, T. Glasmacher, M. Hjorth-Jensen, M. Horoi, D. Miller, V. Moeller, W.F. Mueller, A. Schiller, K. Starosta, A. Stolz, J.R. Terry, A. Volya, V. Zelevinsky, H. Zwahlen, Z=50 shell gap near sn 100 from intermediate-energy Coulomb excitations in even-mass sn 106-112 isotopes, Phys. Rev. Lett. 99 (2007) 162501.

[3] L. Lewandowski, P. Reiter, B. Birkenbach, B. Bruyneel, E. Clement, J. Eberth, H. Hess, C. Michelagnoli, H. Li, R.M. Perez-Vidal, M. Zielinska, Pulse-shape analysis and position resolution in highly segmented HPGe AGATA detectors, Eur. Phys. J. A 55 (2019) 1–13.

[4] M. Nespolo, Pulse Shape Analysis with Germanium Detectors: From MARS To AGATA: Dottorato Di Ricerca in Fisica, Vol. 17, Università degli studi di Padova.: Dipartimento di fisica Galileo Galilei, Ciclo, Università degli Studi di Padova, 2004.

[5] F.C.L. Crespi, F. Camera, O. Wieland, G. Benzoni, S. Brambilla, B. Million, D. Montanari, A pulse shape analysis algorithm for HPGe detectors, Nucl. Instrum. Methods Phys. Res. A 570 (2007) 459–466.

[6] F.C.L. Crespi, F. Camera, B. Million, M. Sassi, O. Wieland, A. Bracco, A novel technique for the characterization of a HPGe detector response based on pulse shape comparison, Nucl. Instrum. Methods Phys. Res. A 593 (2008) 440–447.

[7] A. Olariu, Member, IEEE, P. Désesquelles, Ch. Diarra, P. Médina, C. Parisel, C. Santos, Pulse shape analysis for the location of the γ-interactions in AGATA, IEEE Trans. Nucl. Sci. 53 (2006) 1028–1031.

[8] W. Shockley, Currents to conductors induced by a moving point charge, J. Appl. Phys. 9 (1938) 635–636.

[9] S. Ramo, Currents induced by electron motion, Proc. IRE 27 (1939) 584–585.

[10] O. Wieland, F. Camera, B. Million, A. Bracco, J. van der Marel, Pulse distributions and tracking in segmented detectors, Nucl. Instrum. Methods Phys. Res. A 487 (2002) 441–449.

[11] S. Akkoyun, A. Algora, B. Alikhani, F. Ameil, G. de Angelis, L. Arnold, A. Astier, A. Ataç, Y. Aubert, C. Aufranc, et al., Agata—advanced gamma tracking array, Nucl. Instrum. Methods Phys. Res. A 668 (2012) 26–58.

[12] K. Vetter, A. Kuhn, I.Y. Lee, R.M. Clark, M. Cromaz, M.A. Deleplanque, R.M. Diamond, P. Fallon, G.J. Lane, A.O. Macchiavelli, et al., Performance of the GRETA prototype detectors, Nucl. Instrum. Methods Phys. Res. A 452 (2000) 105–114.

[13] J.P. Wright, L.J. Harkness-Brennan, A.J. Boston, D.S. Judson, M. Labiche, P.J. Nolan, R.D. Page, F. Pearce, D.C. Radford, J. Simpson, C. Unsworth, Position resolution simulations for the inverted-coaxial germanium detector, SIGMA, Nucl. Instrum. Methods Phys. Res. A 892 (2018) 84–92.

[14] M. Descovich, P.J. Nolan, A.J. Boston, J. Dobson, S. Gros, J.R. Cresswell, J. Simpson, I. Lazarus, P.H. Regan, J.J. Valiente-Dobon, P. Sellin, C.J. Pearson, The position response of a large-volume segmented germanium detector, Nucl. Instrum. Methods Phys. Res. A 553 (2005) 512–521.

[15] A. Khaplanov, B. Cederwall, S. Tashenov, Position sensitivity of segmented planar HPGe detectors for the DESPEC project at FAIR, Nucl. Instrum. Methods Phys. Res. A 592 (2008) 325–333.

[16] N. Larson, S.N. Liddick, M. Bennett, A. Bowe, A. Chemey, C. Prokop, A. Simon, A. Spyrou, S. Suchyta, S.J. Quinn, et al., High efficiency beta-decay spectroscopy using a planar germanium double-sided strip detector, Nucl. Instrum. Methods Phys. Res. A 727 (2013) 59–64.

[17] M. Doncel, B. Cederwall, A. Gadea, J. Gerl, I. Kojouharov, S. Martin, R. Palit, B. Quintana, Performance and imaging capabilities of the DEGAS high-resolution γ-ray detector array for the DESPEC experiment at FAIR, Nucl. Instrum. Methods Phys. Res. A 873 (2017) 36–38.

[18] C.S. Lee, J.H. Lee, J.Y. Moon, Y.K. Kwon, Y. Gono, Characteristics of a planar-type segmented germanium detector on gamma-ray detection, linear polarization and position information, Nuclear Phys. A 718 (2003) 550–552.

[19] E. Ideguchi, B. Cederwall, T. Bäck, L. Milechina, Y. Gono, Y.F. Yang, N. Aoi, T. Teranishi, D. Bucurescu, T. Kishida, Position sensitivity of a segmented planar Ge detector, Nucl. Instrum. Methods Phys. Res. A 496 (2003) 373–384.

[20] S. Shimoura, Position sensitivity of Ge detectors and its applications to in-beam nuclear spectroscopy, Nucl. Instrum. Methods Phys. Res. A 525 (2004) 188–192.

[21] E. Rintoul, A.J. Boston, H.C. Boston, A. Caffrey, J.R. Cresswell, L.J. Harkness-Brennan, D.S. Judson, P.J. Nolan, J. Platt, C. Unsworth, T.F. Woodroof, I.H. Lazarus, J. Simpson, J. Cocks, D. Walker, B. Pirard, P. Quirin, Characterisation of the charge collection properties in a segmented planar HPGe detector, Nucl. Instrum. Methods Phys. Res. A 987 (2021) 164804.

[22] C. Domingo-Pardo, N. Goel, T. Engert, J. Gerl, I. Kojouharov, H. Schaffner, F. Didierjean, G. Duchêne, M.H. Sigward, A novel γ-ray imaging method for the pulse-shape characterization of position sensitive semiconductor radiation detectors, Nucl. Instrum. Methods Phys. Res. A 643 (2011) 79–88.

[23] T. Habermann, F. Didierjean, G. Duchêne, M. Filliger, J. Gerl, I. Kojouharov, G. Li, N. Pietralla, H. Schaffner, M.H. Sigward, Application of gamma imaging techniques for the characterisation of position sensitive gamma detectors, Nucl. Instrum. Methods Phys. Res. A 873 (2017) 24–26.

[24] J. Sethi, R. Palit, S. Saha, B.S. Naidu, Performance of a segmented planar Ge detector and its coupling with the clover HPGe detector, in: Proc. AIP Conf. Recent Trends in Nucl. Phys., Vol. 1524, American Institute of Physics, 2013, pp. 287–291.

[25] NIST website, 2022, https://physics.nist.gov/PhysRefData/Xcom/html/xcom1.html.

[26] SIS digitizers, 2022, https://www.struck.de/sis3316-2014-03-20.pdf.

[27] N. Goel, Spatial Characterisation of a 36-Fold Segmented AGATA Detector Via a Novel Scanning System (Ph.D. Thesis), 2011.

[28] GSI GO4 software, 2022, https://www.gsi.de/en/work/research/experiment_electronics/data_processing/data_analysis/the_go4_home_page.htm.

[29] Arzoo Sharma, R. Palit, I. Kojouharov, J. Gerl, M. Gorska-Ott, H. Schaffner, T. Habermann, S. Saha, Biswajit Das, P. Dey, R. Donthi, B.S. Naidu, S. Mandal, Pushpendra P. Singh, Scanning of a double-sided germanium strip detector, EPJ Web Conf. 253 (2021) 11009.

[30] Root, 2022, https://root.cern.ch/root/htmldoc/guides/users-guide/ROOTUsersGuideA4.pdf.

[31] M. Momayezi, W.K. Warburton, William R.A. Kroeger, Position resolution in a Ge-strip detector, in: Hard X-Ray, Gamma-Ray, and Neutron Detector Physics, Vol. 3768, International Society for Optics and Photonics, 1999, pp. 530–537.

[32] P.N. Luke, Unipolar charge sensing with coplanar electrodes-application to semiconductor detectors, IEEE Trans. Nucl. Sci. 42 (1995) 207–213.

[33] Z. he, Potential distribution within semiconductor detectors using coplanar electrodes, Nucl. Instrum. Methods Phys. Res. A 365 (1995) 572–575.

[34] N. Goel, C. Domingo-Pardo, T. Habermann, F. Ameil, T. Engert, J. Gerl, I. Kojouharov, J. Maruhn, N. Pietralla, H. Schaffner, Characterisation of a symmetric AGATA detector using the γ-ray imaging scanning technique, Nucl. Instrum. Methods Phys. Res. A 700 (2013) 10–21.

[35] N. Goel, C. Domingo-Pardo, T. Engert, J. Gerl, I. Kojouharov, H. Schaffner, Spatial calibration via imaging techniques of a novel scanning system for the pulse shape characterisation of position sensitive HPGe detectors, Nucl. Instrum. Methods Phys. Res. A 652 (2011) 591–594.

[36] R.A. Kroeger, W.N. Johnson, J.D. Kurfess, B.F. Phlips, P.N. Luke, M. Momayezi, W.K. Warburton, Position sensitive germanium detectors for the Advanced Compton Telescope, in: AIP Conference Proc., Vol. 510, American Institute of Physics, 2000, pp. 794–798.

[37] Z. He, Review of the Shockley-Ramo theorem and its application in semiconductor gamma-ray detectors, Nucl. Instrum. Methods Phys. Res. A 463 (2001) 250–267.

[38] I. Kojouharov, J. Kojouharova, J. Gerl, Enclosure effects on the internal field distribution in hpge planar detectors, in: IEEE Nuclear Science Symposium Conference Record, Vol. 3, 2006, pp. 1485–1488.

[39] H. Utsunomiya, H. Akimune, K. Osaka, T. Kaihori, K. Furutaka, H. Harada, Surface channel effect on γ-ray response functions of coaxial germanium detectors, Nucl. Instrum. Methods Phys. Res. A 548 (2005) 455–463.

Scanning of a Double-Sided Germanium Strip Detector

Arzoo Sharma[1,3], R. Palit[2], I. Kojouharov[3], J. Gerl[3], M. Gorska-Ott[3], H. Schaffner[3], T. Habermann[3], S. Saha[4], Biswajit Das[2], P. Dey[2], R. Donthi[2], B.S. Naidu[2], S. Mandal[5], Pushpendra P. Singh[1]

[1]Department of Physics, Indian Institute of Technology Ropar, Rupnagar – 140 001, Punjab, India
[2]Department of Nuclear and Atomic Physics, Tata Institute of Fundamental Research, Homi Bhabha Road, Mumbai – 400 005, India
[3]GSI Helmholtzzentrum für Schwerionenforschung GmbH, Planckstrasse 1, 64291 Darmstadt, Germany
[4]University of Massachusetts Lowell, Lowell, Massachusetts 01854, USA
[5]Department of Physics, North Campus, University of Delhi, Delhi – 110 007, India
palit@tifr.res.in, 2017phz0005@iitrpr.ac.in

***Abstract*— This work presents the results from the characterization of a Position-Sensitive Planar Germanium (PSPGe) detector. The PSPGe detector is a double-sided orthogonal strip detector consisting of 10x10 electrical segmentation along the horizontal and vertical directions. The characterization was performed using the coincidence setup between the PSPGe detector and the well-characterized scanning system employing the positron annihilation correlation principle. The scanning system consists of a Position Sensitive Detector (PSD) and ^{22}Na positron source. The main objective of this study is to deploy PSPGe detector for future decay experiments at the Facility for Antiproton and Ion Research (FAIR), Germany. The measurements have been performed to find the depth of gamma-ray interaction in the planar segmented detector. The 2-Dimensional image obtained from the PSD has been used to find the depth of gamma-ray interaction in the planar strip detector using pulse shape analysis. In addition, the sensitivity of PSPGe detector has been investigated by calculating the rise-time from pulse shapes for the front and back strips of the detector.**

Keywords **—Double-Sided Strip Detector; Positron Annihilation Correlation; Position Sensitive Detector; Pulse Shape Analysis.**

I. Introduction

While the nucleus of an atom is a complex object; it has been studied extensively with the aid of characteristic gamma-ray emitted from its decay using gamma spectroscopy tools. The understanding of the structure of nuclei has been obtained through the development of sophisticated solid-state detectors. An advent in this field has been through the development of highly segmented High Purity Germanium (HPGe) detectors like AGATA [1] and GRETA [2]. These detectors are employed to track the path of gamma-ray interaction inside the detector crystal using energy, time, and location information. They are coaxial 4π HPGe detector arrays based on the principle of Pulse Shape Analysis (PSA) [3]. The pulses are stored for each segmented crystal within the defined time window of supporting electronics. Various PSA algorithms have been employed to locate the interaction position that is based on the principle of the Shockley-Ramo theorem [4]. It states that the moving charge, produced by gamma-ray interaction, induces a charge on the electrode, which is detected by the charge-sensitive pre-amplifiers. The correct PSA algorithm helps to reconstruct the complete path of a photon interacting at various locations using the Compton scattering formula. If the algorithm is not reasonably constructed, it may lead to the complete loss of several interacting events. This may further provide wrong energy. Hence, the reasonable choice of PSA algorithm has to be made depending upon the detector geometry, electrode, and segmentation. Therefore, the complexity of signals in these segmented detectors requires complete characterization with known gamma-ray sources.

This manuscript has been put forth to characterize a Planar Position-Sensitive Germanium (PSPGe) detector along the depth. The detector depth is not segmented. Hence, the rise-time studies have been performed to find depth of gamma-ray interaction [5]. Further, the detector has been scanned using a scanning facility developed at GSI Helmholtz Centre for heavy-ion research, Germany [6, 7]. The main aim of performing these tests is to employ the detector as an implantation detector in the Decay SPECtroscopy (DESPEC) experiments in the framework of Facility for Antiproton and Ion Research (FAIR) at GSI [8]. This article is organized as follows. Section II describes the detailed experimental setup. In section III, the analysis procedure is discussed. The Results and conclusions are presented in sections IV and V.

II. Experimental details

The PSPGe detector is a p-type electrically segmented detector. It consists of 10 segmentation along both horizontal as well as vertical directions. The horizontal strips are DC coupled, and the vertical strips are AC coupled. The detector has dimensions of 6 x 6 x 2 cm^3. The energy resolution and efficiency details of the detector are described in the reference [9]. The DC electrodes are etched on the front side of the detector, while AC strips are at the backside. In the present work, DC and AC electrodes are referred to as DC0 to DC9,

and AC16 to AC25, respectively, as indicated in figure 1.

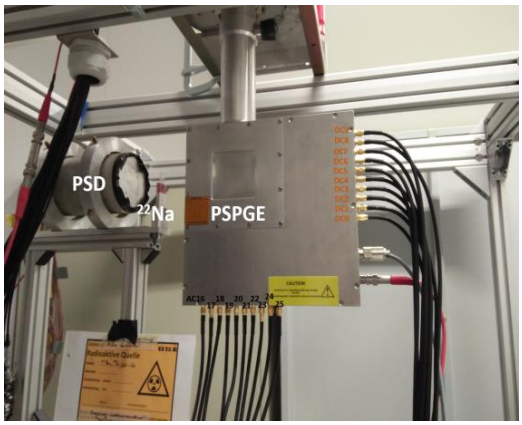

Fig. 1: Typical coincidence setup between PSD (left) and PSPGe detector (right) (DC and AC strips are marked in orange and blue color, respectively).

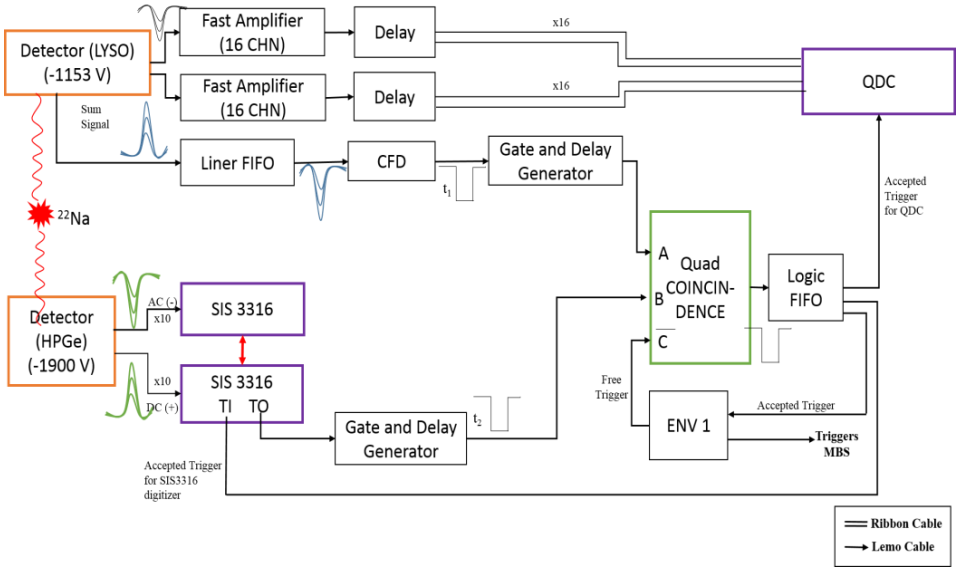

Fig. 2: Typical block diagram of electronics arrangement used for setting up the coincidence between PSD and PSPGe detectors.

The experimental setup is shown in Fig. 1. The PSPGe detector has been set up in coincidence with the PSD using ^{22}Na source. The PSD consists of a LYSO scintillator coupled to Position-Sensitive Photo Multiplier Tube (PSPMT) [10]. After pair annihilation, the two gamma-rays are detected in PSPGe and PSD. The distance between ^{22}Na source and PSPGe detector was kept 8.6 cm. The distance was optimized to get a complete image by looking at the online 2-Dimensional (2-D) image using GSI Object Oriented On-line Off-line (GO4) software. The 2-D image is extracted from PSD, consisting of PSPMT with 16-X and 16-Y anodes mesh. The complete electronics block diagram is shown in Fig. 2. The 32 anode output signals from the PSD were amplified using Fast Amplifier (N979). Afterward, the output was fed to Versa Module Eurocard (VME) based multi-event Charge to Digital Convertor (QDC V792) unit with 12-bit resolution. The cathode output from the PSD was used to generate timing gate, t_1 (depicted in Fig. 2), via Constant Fraction Discriminator (CFD - CF4000). The 10 DC and 10 AC outputs of the PSPGe detector were fed to 100 MHz digitizers from Struck Innovative Systeme (SIS3316) modules. It provides information on pulse shape and energy for each interacting gamma-ray on an event-by-event basis. The digitizer's Trigger-Out (TO) output was a logic pulse that contained information of the OR (OR of the time) of all channels, indicated as time t_2 in Fig. 2. Afterward, t_1 and t_2 were set up in coincidence using the Quad Coincidence unit (CO4001). The data from QDC and SIS3316 was read out using the Multi-Branching Data Acquisition System (MBS). The ENV1 module contains the dead time of the MBS readout, which is put in anti-coincidence with t_1 and t_2 using CO4001. The output was used as an accepted trigger for the QDC and SIS3316 digitizer. The settings of the digitizer were made using desktop Graphical User Interface (GUI). The monitored data rate was ~250 Hz.

III. Data Analysis Procedure

The data analysis has been performed using GO4, C++, and ROOT. The critical points of the analysis procedure are listed here. First, the 2-D image is reconstructed from the charge collected at X and Y anodes in PSD for the coincidence events. The reconstruction has been obtained by the centroid fitting method, as displayed in Fig. 3.

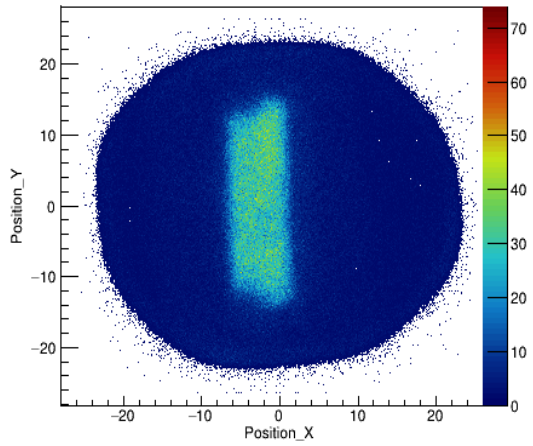

Fig. 3: The 2-D image obtained from PSD.

The middle region with maximum counts represents the active region of detector volume. 2-D image is projected onto X-axis, and it represents the depth of PSPGe. It is used for dividing the depth into segments because of no segmentation along the depth. First, the obtained energy spectra from the digitizer are calibrated. Then, it is used to select an electrode of interest by gating on the Compton edge. The pulse shape and/or trace obtained from the digitizer provides information on the gamma-interaction event for the selected electrode. The analysis has been performed for the obtained traces as described in reference [11], i.e., the baseline subtraction is performed, followed by normalization. Afterward, traces are time-aligned at 10% of the final amplitude.

The work has been presented to understand the analysis for finding the depth of gamma-ray interaction using the setup shown in Fig. 1. The Compton edge of 511 keV photopeak is used to select two middle strips DC4 and AC20. The pulse shape is analyzed for different points along the depth. The rise time is measured for selected traces at a specific depth location. The average of multiple traces is considered to find the rise-time. The sensitivity of the PSPGe detector towards depth would depend on how precisely charge collection could be measured for two charge carriers (electrons and holes) at the two opposite-facing electrodes. It would then lead to different rise-time values at different depth locations. In the scope of the present analysis, T30 rise-times have been calculated for DC4 and AC20 strips. It is defined as the time required to reach 30% of the maximum amplitude minus the time required to reach 10% of the maximum amplitude. The analysis results, for the behavior of both DC and AC strips, have been discussed in detail in the upcoming section.

IV. Results and Discussion

The coincidence technique using the principle of positron annihilation has been used to characterize the electrically segmented PSPGe detector. The increased segmentation is beneficial to track each Compton scattered event in a different segment. The centroid fitting method has been used to reconstruct the image from PSD.

To understand the charge induced by the incoming gamma-rays, the rise-time has been calculated for the pulse shapes obtained from SIS3316 digitizer. The analysis has been performed using energy cut at Compton edge for two middle strips, DC4 and AC20. As a representative case, the behavior of DC4 and AC20 strips is shown in Fig. 4, for one of the middle cuts. In the figure, the amplitude of the trace is plotted as a function of time. The obtained T30 rise-time values for DC4 and AC20 strips are 30 ns and 80 ns, respectively. This shows the appreciable time difference between the two traces. This feature can be further used to find the rise-time as a function of depth.

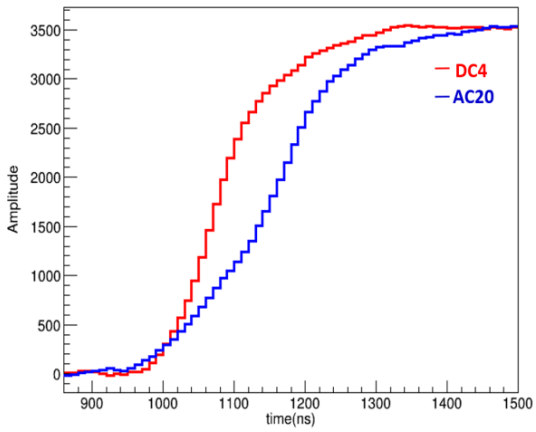

Fig. 4: T10 aligned traces for a middle cut selection (-2.1<Position_X<-1.9) on active region in 2-D image obtained from PSD. Traces of DC4 and AC20 are represented by red and blue color, respectively.

The difference in rise-times of the two strips may be attributed to the movement of charge carriers towards the respective electrodes. The front face of the detector consists of DC segments, and the AC segments are etched on the backside of the detector. The electrons would travel towards the DC electrode while holes would be collected at the AC electrode. The rise-time distribution is plotted for one of the depths in Fig. 5. In this plot, T30 rise-time counts are represented by a black histogram. The red curve is the Gaussian fit to find the centroid of the distribution. Hence, the centroid can be used to find the rise-time at a specific depth. In addition, the spread in the distribution may be used to infer the error in the obtained rise-time values [12].

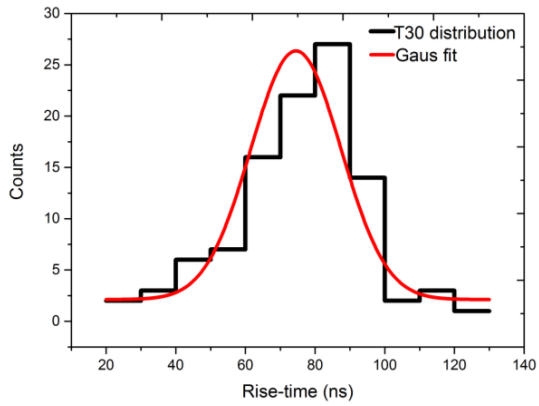

Fig. 5: Plot of counts vs rise-time (T30) at a specific depth. The red curve is the Gaussian fit (used to find centroid of the distribution).

The analysis has been extended to find the rise-time as a function of depth for both the DC4 and AC20 electrodes. It is shown in Fig. 6(a)-(b).

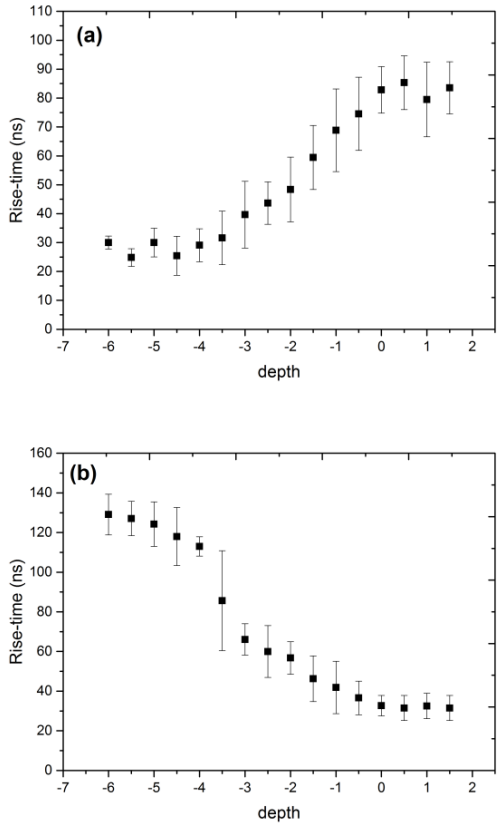

Fig. 6: T30 rise-time values as a function of depth for (a) DC4 and (b) AC20 segments, respectively.

In this figure, X-axis represents depth, i.e., going from the front to the backside of the detector. The values plotted are the centroids of the rise-time distribution obtained for each depth. The error has been calculated for each data point from the rise-time distribution spread, as indicated in Fig. 5. For DC4 (Fig. 6(a)), with an increase in depth, rise-time increases. Fig. 6(b) shows that the rise-time of AC20 decreases with an increase in depth. The rise-time of the DC4 segment starts to increase while traversing from the left to right side, i.e., from DC towards the AC electrodes. It occurs because of the slow collection of electrons at the front surface with an increase in depth.

In comparison, the holes are collected faster, therefore, the faster rise-time response at the AC electrode. This implies that the difference in collection times of the two charge carriers, between the front and backside of the detector, can successfully be applied to find the depth of the gamma-ray interaction. From the above analysis, it may be deduced that the position response of the detector is sensitive towards charge collection at the respective electrodes.

V. Summary and Conclusions

In summary, a PSPGe detector has been characterized using a time-efficient scanning facility at GSI Germany. The response of the detector has been studied for gamma-ray interaction along the depth using rise-time values obtained from the pulse shape analysis. The behavior of induced charge along the detector surface has been obtained and analyzed using rise-time calculation as a function of depth. The T30 rise-time distribution has been used to find the position sensitivity of the detector towards a gamma-ray hit. The results obtained in this work have been promising for finding the position sensitivity of the detector as the subsequent analysis steps.

Acknowledgment

This work is partially supported by the Department of Atomic Energy, Government of India, under project No. 12P-R&D-TFR-5.02-0400. The authors would like to acknowledge the Helmholtz International Center for FAIR in Germany and Prof. H. J. Wollersheim for constant support for carrying out this work.

References

[1] S. Akkoyun, A. Algora, B. Alikhani, F. Ameil, G. De Angelis, L. Arnold, A. Astier, A. Ataç, Y. Aubert, and C. Aufranc, "*Agata—advanced gamma tracking array*". Nuclear Instruments Methods in Physics Research Section A: Accelerators, Spectrometers, Detectors Associated Equipment 2012. **668**: p. 26-58.

[2] K. Vetter, A. Kuhn, I. Lee, R. Clark, M. Cromaz, M. Deleplanque, R. Diamond, P. Fallon, G. Lane, and A. Macchiavelli, "*Performance of the GRETA prototype detectors*". Nuclear Instruments Methods in Physics Research Section A: Accelerators, Spectrometers, Detectors Associated Equipment 2000. **452**(1-2): p. 105-114.

[3] F. Crespi, F. Camera, B. Million, M. Sassi, O. Wieland, and A. Bracco, "*A novel technique for the characterization of a HPGe detector response based on pulse shape comparison*". Nuclear Instruments Methods in Physics Research Section A: Accelerators, Spectrometers, Detectors Associated Equipment, 2008. **593**(3): p. 440-447.

[4] Z. He, "*Review of the Shockley–Ramo theorem and its application in semiconductor gamma-ray detectors*".

Nuclear Instruments Methods in Physics Research Section A: Accelerators, Spectrometers, Detectors Associated Equipment 2001. **463**(1-2): p. 250-267.

[5] M. Momayezi, W. K. Warburton, and R. A. Kroeger. "*Position resolution in a Ge-strip detector*". in *Hard X-Ray, Gamma-Ray, and Neutron Detector Physics*. 1999. International Society for Optics and Photonics.

[6] T. Habermann, F. Didierjean, G. Duchêne, M. Filliger, J. Gerl, I. Kojouharov, G. Li, N. Pietralla, H. Schaffner, and M.-H. Sigward, "*Application of gamma imaging techniques for the characterisation of position sensitive gamma detectors*". Nuclear Instruments Methods in Physics Research Section A: Accelerators, Spectrometers, Detectors Associated Equipment, 2017. **873**: p. 24-26.

[7] C. Domingo-Pardo, N. Goel, T. Engert, J. Gerl, I. Kojouharov, H. Schaffner, F. Didierjean, G. Duchêne, and M. Sigward, "*A novel γ-ray imaging method for the pulse-shape characterization of position sensitive semiconductor radiation detectors*". Nuclear Instruments Methods in Physics Research Section A: Accelerators, Spectrometers, Detectors Associated Equipment, 2011. **643**(1): p. 79-88.

[8] A. Khaplanov, B. Cederwall, and S. Tashenov, "*Position sensitivity of segmented planar HPGe detectors for the DESPEC project at FAIR*". Nuclear Instruments Methods in Physics Research Section A: Accelerators, Spectrometers, Detectors Associated Equipment, 2008. **592**(3): p. 325-333.

[9] J. Sethi, R. Palit, B. Naidu, S. Saha, T. Trivedi, R. Donthi, and S. Jadhav. "*Characterization of a Planar Ge Strip Detector and its Coupling with a Segmented HPGe Clover Detector*". in *Proceedings of the DAE Symp. on Nucl. Phys*. 2011.

[10] N. Goel, C. Domingo-Pardo, T. Engert, J. Gerl, I. Kojouharov, and H. Schaffner, "*Spatial calibration via imaging techniques of a novel scanning system for the pulse shape characterisation of position sensitive HPGe detectors*". Nuclear Instruments Methods in Physics Research Section A: Accelerators, Spectrometers, Detectors Associated Equipment, 2011. **652**(1): p. 591-594.

[11] N. Goel, C. Domingo-Pardo, T. Habermann, F. Ameil, T. Engert, J. Gerl, I. Kojouharov, J. Maruhn, N. Pietralla, and H. Schaffner, "*Characterisation of a symmetric AGATA detector using the γ-ray imaging scanning technique*". Nuclear Instruments Methods in Physics Research Section A: Accelerators, Spectrometers, Detectors Associated Equipment, 2013. **700**: p. 10-21.

[12] M. Descovich, P. Nolan, A. Boston, J. Dobson, S. Gros, J. Cresswell, J. Simpson, I. Lazarus, P. Regan, and J. Valiente-Dobon, "*The position response of a large-volume segmented germanium detector*". Nuclear Instruments Methods in Physics Research Section A: Accelerators, Spectrometers, Detectors Associated Equipment, 2005. **553**(3): p. 512-521.

Position Sensitivity Study of Double Sided Germanium Strip detector Using Coincidence Method

Arzoo Sharma[1],* R. Palit[2],† T. Habermann[3], J. Gerl[3], I. Kojhourav[3], H. Schaffner[3], M. Górska[3], S. Saha[4], Biswajit Das[2], P. Dey[2], R. Donthi[2], B.S. Naidu[2], S. Mandal[5], and Pushpendra P. Singh[1]

[1]*Department of Physics, Indian Institute of Technology Ropar, Rupnagar – 140001, INDIA*
[2]*Department of Nuclear and Atomic Physics, Tata Institute of Fundamental Research, Mumbai - 400005, INDIA*
[3]*GSI Helmholtzzentrum für Schwerionenforschung GmbH, Planckstrasse 1, Darmstadt - 64291, GERMANY*
[4]*School of Advance Sciences, VIT University, Vellore - 632014, INDIA and*
[5]*Department of Physics, North Campus, University of Delhi, Delhi – 110007, INDIA*

Introduction

The development of highly segmented position sensitive germanium detectors have marked the advancement in the field of gamma spectroscopy experiments. The highly segmented detector arrays have striking features like gamma-ray tracking and Pulse Shape Analysis (PSA), which provides precise information of the gamma interaction location inside the detector from the comparison of pulses obtained for two orthogonal data sets [1]. For the characterization of such segmented detectors, it is necessary to record pulse shapes for each gamma interaction point inside the detector because of the complexity of pulses at various locations. The data set of stored pulses is compared with the pulse shapes obtained through experimental measurements performed for an unknown source. In the present work, the scanning facility at GSI has been used to characterize the Position Sensitive Planar Germanium (PSPGe) detector.

Experiment and Analysis

The scanner consists of a Position Sensitive Detector (PSD) which is made of Lutetium Yttrium Orthosilicate (LYSO) scintillator crystal coupled with the 16 X and 16 Y anodes mesh Photomultiplier tube [2]. The PSD has been well characterized, and the position resolution is of the order of ≈ 1-2 mm. The PSPGe is a position sensitive double sided orthogonal strip detector. It consists of 10 horizontal (DC coupled) and 10 vertical (AC coupled) strips at the two opposite faces [3]. The size of the detector is 6 x 6 x 2 cm^3. In the present analysis, the horizontal strips are numbered from DC0 to DC9, and vertical strips are numbered from AC16 to AC25.

The coincidences have been demanded between PSD and PSPGe detectors using positron annihilation employing a ^{22}Na source. After the process of pair annihilation, two 511 keV gamma-rays are emitted in opposite directions from each other. The charge collected in PSD is used to obtain 2-D image from the coincidence data. It has been achieved by using QDC to acquire the information of charge collected at X and Y anodes in PSD. The centroid fitting method has been used to find the centroid channel of charge collected at anode for the coincidence events. The 2-D image obtained from coincidence is shown in Fig. 1(a). The analysis has been performed to look for the position sensitive strips by gating on 511 keV photopeak energy. After demanding the coincidence events for every time any of the two horizontal (DC3 or DC8) or two vertical strips (AC19 or AC24) fires, the image obtained has been shown in Fig. 1(b).

*Electronic address: 2017phz0005@iitrpr.ac.in
†Electronic address: palit@tifr.res.in

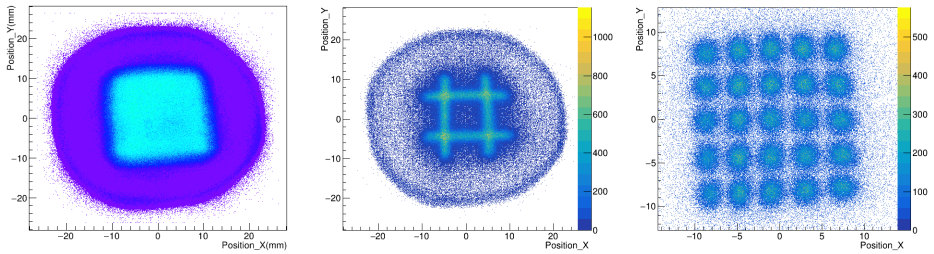

FIG. 1: (a) 2-D image obtained from PSD for coincidence setup showing (a) complete image (b) two selected strips in horizontal and vertical directions (c) voxel arrangement.

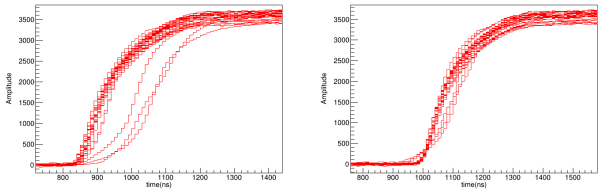

FIG. 2: Traces (a) before and (b) after time alignment.

The size of each strip is 6 mm. The above stated analysis has been further extended to look for voxels in the 2-D image. For this, the analysis gate was constructed for strips with a condition that a horizontal strip fires in coincidence with a vertical strip. The selected horizontal strips are DC0, DC2, DC4, DC6, and DC8. The vertical strips are AC16, AC18, AC20, AC22, and AC24.

The 2-D image has been used to study the charge collection properties of PSPGe detector. This has been performed by analysing the pulse shapes and energy obtained from SIS3316 digitizer for each strip in PSPGe detector. The pulses/traces collected are refined by performing baseline subtraction. Thereafter, the traces are normalized w.r.t. the maximum amplitude of pulse shape, and they are time aligned at 10% of the maximum amplitude. The traces before and after normalization have been represented in Fig. 2 (a) and (b), respectively.

From the above analysis, it may be stated that the PSPGe detectoris sensitive towards gamma-ray interaction. This can be studied by gating on a strip and further finding the time response using the rise-time information obtained from trace generated by the incoming gamma-ray event inside the detector. The future analysis to calculate position resolution of the PSPGe detector is in progress.

Acknowledgment

This work is partially supported by the Department of Atomic Energy, Government of India, under project No. 12P-R&D-TFR-5.02-0400. The authors would like to acknowledge the Helmholtz International Center for FAIR in Germany.

References

[1] F.C.L. Crespi et al., *Nucl. Instr. Meth. A*, vol. 593, no. 3, pp. 440–447, 2008.

[2] C. Domingo-Pardo et al., *Nucl. Instr. Meth. A*, vol.643, no. 1, pp. 79–88, 2011.

[3] J. Sethi et al., *in Proc. AIP Conf. ICRTNP-2012*, vol. 1524, 2013, pp. 287–291.